Cold Collisions in a Molecular Synchrotron

Aernout P. P. van der Poel

VRIJE UNIVERSITEIT

Cold Collisions in a Molecular Synchrotron

ACADEMISCH PROEFSCHRIFT

ter verkrijging van de graad Doctor aan
de Vrije Universiteit Amsterdam,
op gezag van de rector magnificus
prof.dr. V. Subramaniam,
in het openbaar te verdedigen
ten overstaan van de promotiecommissie
van de Faculteit der Bètawetenschappen
op dinsdag 13 maart 2018 om 15.45 uur
in de aula van de universiteit,
De Boelelaan 1105

door

Aernout Pieter Paul van der Poel

geboren te Eelde

promotor:	prof.dr. W.M.G. Ubachs
copromotor:	dr. H.L. Bethlem

This thesis was approved by the members of the reviewing committee:

prof. dr. H.G. Raven	(Vrije Universiteit Amsterdam)
dr. D. Carty	(Durham University)
prof. dr. S. Hoekstra	(Rijksuniversiteit Groningen, Nikhef)
prof. dr. G.J.M. Meijer	(Fritz-Haber-Institut der Max-Planck-Gesellschaft, Radboud Universiteit)
prof. dr. D.H. Parker	(Radboud Universiteit)

The work described in this thesis was carried out at the Institute for Lasers, Life and Biophotonics of the Vrije Universiteit Amsterdam and was supported by the Netherlands Organization for Scientific Research (NWO) via a VIDI grant, by the European Research Council (ERC) via a Starting grant, and by FOM Project 'Broken Mirrors and Drifting Constants'.

ISBN: 978-94-028-0948-0
Printed by: Ipskamp Printing

Contents

Chapter 1

Introduction, summary, and outlook

To study collisions between molecules is to ask one of the most fundamental questions in chemistry: "What happens when molecules meet?" More specifically, in this thesis, I will try to answer the question: "What happens when two slow molecules meet?" Studying collisions in the cold regime of 10–100 K is important for understanding the chemistry in interstellar gas clouds. By measuring collision cross sections in the laboratory, rate constants can be calculated for the bulk processes that occur in these clouds, allowing a better understanding of e.g. the abundance of molecules in the universe, or the quantum state population distribution of these molecules. Furthermore, cold collisions are interesting as—in contrast to collisions at room temperature—the wave properties of molecules are very important.

The study of cold collisions is a subfield of the field of atomic and molecular physics, which concerns itself with the study of atoms and molecules, the building blocks of all 'stuff' that surrounds us. As described by quantum mechanics, these particles can only exist in specific states: Just like a guitar string can only support standing waves at frequencies of which half the wavelength fits exactly an integer number of times on the length of the string, in the same way do electrons fit only in discrete wave functions around a nucleus, do bonds between atoms vibrate only in discrete levels of excitation, and do molecules only rotate with discrete amounts of angular momentum.

Electronic transitions typically have energies of tens of thousands Kelvins, meaning that the atoms and molecules around us, at a comfortable room temperature of 293.15 K (20°C), will all be in their electronic ground state. The energies of these electronic transitions correspond roughly to the energy of photons in the visible or UV parts of the spectrum. Vibrational excitations are much lower in energy and have typical level energies of hundreds of Kelvins, meaning that depending on the species, some of the molecules around us can

be vibrationally excited. These energies typically correspond to the energy of photons in the infrared. Finally, rotational excitations are even lower in energy. They have energies on the order of a Kelvin, which corresponds to microwave radiation. Thus the molecules around us are rotating like crazy. The reason the corresponding photon energies are mentioned, is because an important technique to measure these transitions is spectroscopy: Illuminate a particle with EM-radiation, while scanning the frequency of the radiation. If the frequency is just right, i.e. resonant with a frequency of an excited state, a photon of the light can be absorbed by the particle as it makes a transition to the excited state. In this way, the energy levels of atoms and molecules can be measured.

The energies of these levels are determined by the structure of the atom or molecule: What are the masses of its constituents? Where are they located with respect to each other? What is the strength of the interaction between them? Or even more fundamentally: Which interactions exist between its constituents in the first place? These are the questions we aim to answer by studying the energy levels of atoms or molecules.

1.1 Introduction to collisions

Returning to the subject of collisions (for textbooks on this topic, see for instance Refs. [1, 2]), there are three kinds: In reactive collisions, the chemical composition of the collision partners changes. Molecules break apart and/or new molecules are formed. In inelastic collisions the chemical species remain intact, but some of the collision energy is converted to internal energy in one (or more) of the collision partners: it is (de)excited to a higher (or lower) rotational, vibrational, and/or electronic level. The last type of collision is the elastic collision. The collision partners do not undergo any internal change in elastic collisions, only their momentum is changed. These different paths a collision can take, i.e. specific reactions, inelastic collisions to specific quantum states, or elastic collisions, are called collision channels.

The rates at which these collisions occur are described by the collision cross section. This quantity has units of square meters, and can intuitively be described as the area within which the particles must meet in order for them to collide. For hard sphere collisions for example, think of marbles, the cross section is simply the area of the circle whose radius is the sum of the radii of the marbles. Different collision channels have their own collision cross sections. The sum of the cross sections of all channels is called the total cross section. The differential cross section describes how the cross section depends on the scattering angle θ (depicted in Figure 1.1). It can be integrated over all scattering angles to retrieve the integral cross section.

Somewhat surprisingly, collision cross sections for collisions (both integral and differential) depend on the collision energy. In the example of marbles for example, as mentioned above, there is no reason why the cross section would

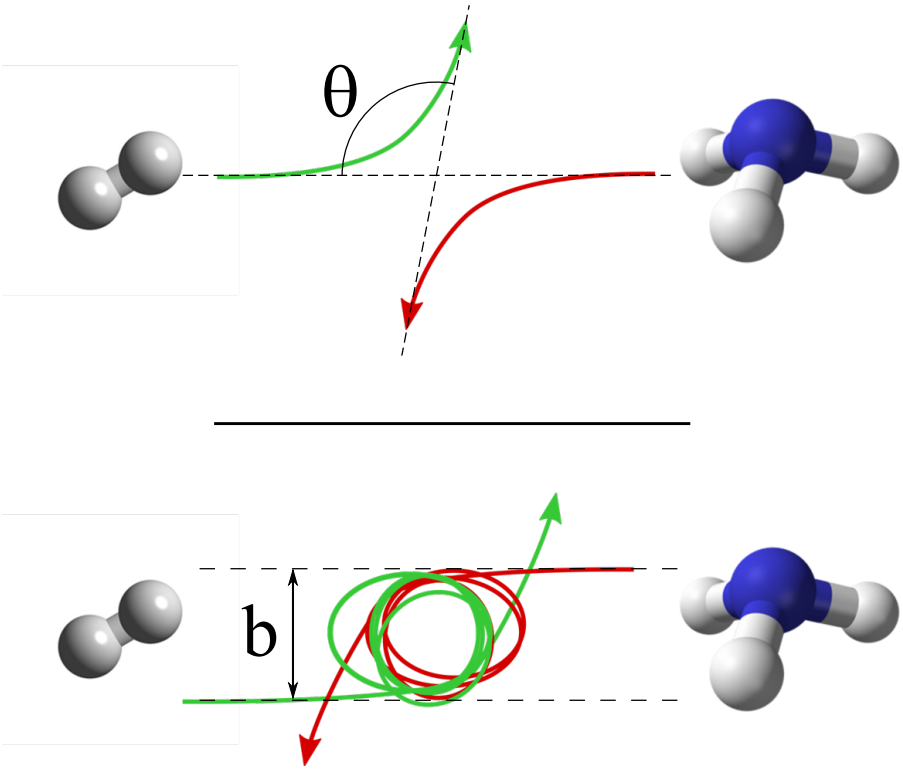

Figure 1.1 – Two (semi-classical) examples of a collision between a hydrogen molecule and an ammonia molecule. The top panel shows an elastic collision with scattering angle θ. The bottom panel shows an elastic collision that leads to an orbiting resonance. In this example the molecules do not approach each other head-on, but rather with some non-zero impact parameter b.

depend on the collision energy. After all, the size of the marbles does not change with their velocity. Atoms and molecules are, however, not marbles; for one, they possess a long range attractive Van der Waals potential next to the short range repulsive core, but more importantly, they are governed by the rules of quantum physics. Thus, they are waves as much as they are particles.

A trivial example of energy dependence of the collision cross section for non-elastic collisions, is that any collision that increases the internal energy of the collision partners, i.e. any endothermic reactive or inelastic collision, is simply not possible when the collision energy is insufficient.

More subtle are collisions for which the collision energy is sufficient to reach the final state, but an energy barrier in-between the initial and final states prevents the system to make it to the other side in a classical way. This barrier can be the result of the interaction between the particles, or it can be the centrifugal energy barrier that is a result of the angular momentum the

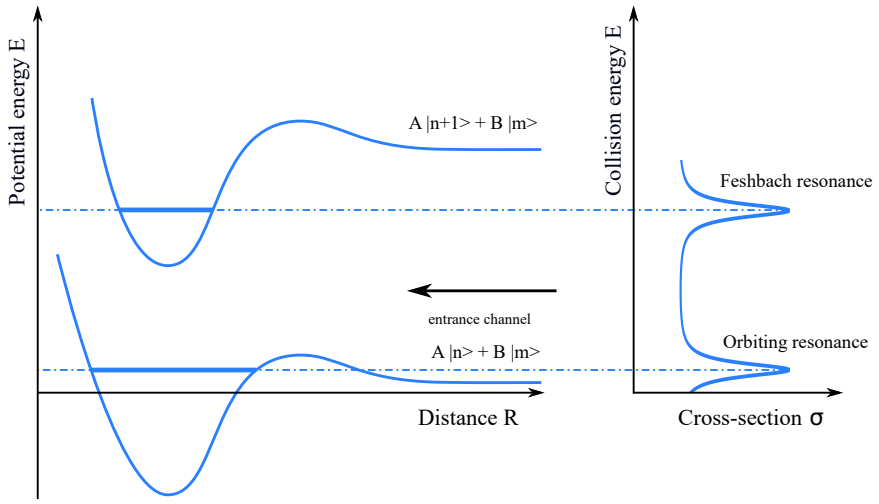

Figure 1.2 – Schematic representation of how bound states in the interaction potential bring about Feshbach and orbiting resonances. The graph on the left shows the interaction energy of two particles, A and B, as a function of the distance between them. The figure on the right shows the cross section as a function of the collision energy. An orbiting resonance is caused by a semi-bound state in the potential energy surface the particles occupy before the collision, i.e. A in quantum state $|n\rangle$, B in quantum state $|m\rangle$. A Feshbach resonance is caused by a semi-bound state in a higher lying potential energy surface, in which one of the particles occupies a higher lying quantum state, for example A in quantum state $|n+1\rangle$. Note that, while occupying this semi-bound state in the higher lying potential, the particles do not have enough energy to part ways until particle A returns to its starting state $|n\rangle$. Based on Fig. 4 of Ref. [3].

system has when the particles approach each other at some collision parameter b rather than head-on (see Figure 1.1). Quantum mechanically speaking the system is able to tunnel through this barrier, be it at a low rate. Interestingly, when there is a bound state behind the energy barrier, the energy of which is equal to the collision energy, the probability to tunnel through the energy barrier and occupy this bound state behind it (read: the collision partners stick together) is dramatically enhanced, and so is the collision cross section, as shown in Figure 1.2. These so-called orbiting resonances are clear and striking signatures of quantum mechanics at work. The energies at which these resonances occur, i.e. the energies that correspond to the discrete ways in which the collision partners can stick together, gives clear and direct insight in the potential energy surface that describes the interaction between them. Measuring well-resolved collisional resonances is a Holy Grail of contemporary physical chemistry.

For atoms, some of these resonances have been observed at thermal temperatures (see below). For collisions with molecules however, the resonances can

only be seen at much lower collision energies. Compared to atoms, molecules have much more internal structure in the form of vibrational and rotational energy levels, so that much more quantum waves are involved in the collisions. Since collision resonances are, by definition, caused by only one of these waves, the resonances are averaged out by all the other waves involved. To make sure only a few partial waves contribute, the collision energy needs to be reduced so that there is not enough energy for these higher lying vibrational and rotational states to play a role. As mentioned above, rotational energies are typically several Kelvin, giving an idea for the energy range required to measure these resonances in collisions with molecules.

The fact that the cross sections depend on the collision energy is not a bad thing. On the contrary, it allows us to learn about these atoms and molecules by measuring this energy dependence, providing us with a whole field of interesting physics to explore.

1.2 Cold and controlled molecules

In order to obtain molecules with a small velocity spread, we need to lower their temperature. Several techniques exists to do this, as for example described in Ref. [4].

The most employed method to cool down molecules, typically to around 1 K, is to make a molecular beam from a supersonic expansion [5, 6]. Such a beam is created by releasing a pulse of gas from a high-pressure volume (typically 1–4 bar), through a nozzle, into a vacuum. As the gas expands into the vacuum, the internal energy of the gas is converted into forward kinetic energy by means of collisions. This expansion is faster than the speed at which shock waves (i.e. sound) travel through the expanding gas, hence the expansion is *supersonic*. This has the important effect that a disturbance in the back of the gas pulse is unable to disrupt the expansion in the front. Few centimeters behind the valve, the gas has cooled and expanded so far that collisions no longer take place. From this point onwards the molecular beam is 'frozen'; the molecules continue their journey without interacting with their neighbours and can be studied without interference. During the expansion, the molecules are also vibrationally and rotationally cooled. The result is a gas pulse with a low translational ($\leqslant 1$ K), vibrational (about 50 K) and rotational temperature (about 5 K), but with a forward velocity of typically several hundreds of meter per second. Typical velocity spreads are tens of meters per seconds.

The velocity of a supersonic beam depends on the mass of the species used: the heavier the particles are, the lower their velocity will be. If a few percent of a molecule of interest is seeded into a heavy buffer gas such as xenon, collision between the faster molecules and slower buffer gas atoms will slow down and reduce the temperature of the molecules even further. Even lower temperatures and speeds can be achieved by cooling down the valve that releases molecular packets.

To further slow and manipulate the molecules, some sort of handle on them is necessary. Fortunately, many molecules have an electric dipole moment: While the net charge of the molecule is neutral, one side of the molecules has a bit excess positive charge while the other side is more negatively charged. The potential energy of an electric dipole in an electric field is linear in both the size of the electric dipole and the strength of the electric field. Depending on the orientation of the dipole with respect to the electric field, the molecule is either attracted to areas with low electric field (so-called low field seekers) or attracted to higher electric fields (high field seekers).

In Figure 1.3, the resulting Stark shifts of the sublevels of the $J = 1$ rovibrational ground state in ND_3 are shown as example. This state is split into a symmetric and antisymmetric state by the umbrella motion of the ammonia molecule, with an inversion splitting of $0.79\,\mathrm{cm}^{-1}$ [7]. The rotation of the ammonia molecule is further described by quantum number M, the projection of J on the direction of the electric field, and K, the projection of J on the three-fold rotational symmetry axis of the molecule. Their product, MK, is indicated for the states in Figure 1.3. States for which $MK = 0$ are insensitive to the electric field. States for which $MK = \pm 1$ are sensitive to electric field and thus are Stark shifted by the field. The Stark shift is seen to grow quadratically for small electric fields. In this regime, the electric field orients the molecule, such that its effective dipole moment increases together with the field strength. When the molecule is completely oriented and has reached its maximum effective electric dipole moment, the Stark shift becomes linear with the electric field strength. This Stark shift allows the use of gradients in electric fields to manipulate the ammonia molecule. Note however that the force exerted on a dipole is typically ten orders of magnitude smaller than the forces that are used to manipulate charged particles (ions), and that only molecules in certain rotational states can be manipulated.

The dipole moment of molecules allows several additional techniques to be applied [9–11]. A hexapole, for example, can be used to focus the molecules in a molecular beam that occupy a specific low-field-seeking state, while molecules in other quantum states are defocused. This leads to a higher beam density and increased beam quantum state purity. Another technique uses electric fields to decelerate the beam using Stark deceleration. For a spectroscopic experiment, a slower beam means an increased interaction time and thus more precise measurements. More extremely, molecules can be decelerated all the way to stand-still and subsequently be trapped or tossed up in a fountain geometry [12]. Another path is to use the decelerator to create very cold beams of molecules with *well-controlled* velocities, rather than velocities as low as possible. Such beams are very useful in collision experiments, where the decelerator is used to tune the energy of collisions with these state-selected molecules.

And thus, we have finally arrived at the fascinating research field that is the focus of this thesis: the field of collisions with cold and controlled atoms and molecules [13–18]. The remainder of this introduction will be as follows. First,

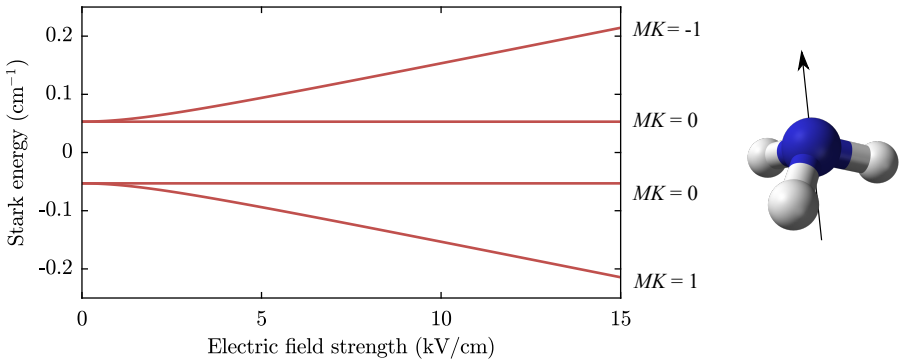

Figure 1.3 – Left: Stark shifts of the sublevels of the $J = 1$ ro-vibrational ground state of ND_3 as a function of electric field strength [8]. Right: schematic representation of an ammonia molecule including its three-fold rotational symmetry axis.

a selection of collision experiments will be showcased. This will demonstrate how the molecular beam techniques described above can be applied to study different kinds of collisions, at different degrees of 'cold'. Next, I will present a short history on the development of the molecular synchrotron, to provide an understanding of the road that has led to the experiments presented in this thesis. These experiments will then be summarized, through the same goggles as the other showcases, to show how this work fits into the bigger picture. Finally, the general conclusions of this work will be presented, as well as an outlook for future endeavors.

1.3 Discussion of selected scattering experiments

The development of cold, supersonic atomic or molecular beams, including several options to control them, also made possible a wide array of collision experiments. Most are based on crossed molecular beam experiments. The energies of experiments below are given in the unit of wavenumber (cm^{-1}); $1\,cm^{-1}$ corresponds to an energy of 1.4 K, or 0.12 meV, or 2.9×10^{-3} kcal/mol, or 2.0×10^{-23} J. For comparison, the energy involved in clapping your hands together corresponds roughly to an energy of 4 J, or $2 \times 10^{23}\,cm^{-1}$. (Your hands are a hundred times slower than the particles in these experiments, typically, but also a factor of 10^{26} heavier.)

1.3.1 High energy collision studies

The first indications of orbital resonances were found by Schutte *et al.* in 1972 [19]. In their experiment, a beam of hydrogen atoms was collided with a beam of mercury atoms, under an angle of 71°. The resulting relative velocity was

scanned between 1,000–4,000 m/s using a velocity selector. On top of so-called glory oscillations, a deviation was measured around 1,500 m/s relative velocity, that turned out, after comparing the experimental results with theory, to be due to orbital resonances.

Toennies *et al.*, in 1979, published results from scattering experiments of hydrogen atoms and hydrogen molecules with rare gas atoms neon, argon, krypton, and xenon under an angle of 46° [3]. Several clear, resolved orbiting resonances in elastic collisions were measured in a range of relative velocities from 300–1,000 m/s. Also in this experiment, the velocity of the hydrogen beams was controlled with a velocity selector.

1.3.2 Towards ultralow temperature in collision experiments

More than 40 years later, Chefdeville *et al.* used two cryogenically cooled Even-Lavie valves at low crossing angle to reach low collision energies. In one experiment, they collided a beam of hydrogen molecules with a beam of 1% carbon monoxide seeded in helium [20]. The beam speeds, both around 940 m/s, differed by only 7 m/s. In combination with crossing angles down to 12.5°, collision energies below 3.85 cm^{-1} were achieved, which is the energy difference between the CO $j = 0$ and $j = 1$ states. By detecting the carbon monoxide molecules in the $j = 1$ state, they were able to measure the relative, integral cross sections for inelastic CO + H_2 collisions, and in doing so detected three collision resonances.

In another experiment, Chefdeville *et al.* collided a beam of hydrogen molecules with a beam of 0.3% oxygen molecules seeded in helium [21]. Collision energies down to 3.95 cm^{-1} were achieved, which is the energy difference between the O_2 $N = 1, j = 0$ and $N = 1, j = 1$ states. By detecting oxygen molecules in the $N = 1, j = 1$ state, they were able to measure the relative, integral cross sections for inelastic O_2 ($N = 1, j = 0$) + H_2 (both para and normal) collisions, again measuring multiple resonances.

Taking this idea further, scattering experiments have been carried out with merged beams, i.e., with a crossing angle of 0°. Using a bent magnetic guide, beams of metastable helium atoms can be merged with a free expansion of any other gas. In the group of Narevicius, multiple experiments have been performed with these metastable helium beams colliding with beams of argon atoms, beams of H_2, HD, or D_2 molecules, or beams of para-H_2 molecules ($j = 0$). Both beams originating from temperature-controlled Even-Lavie valves. In these experiments, by matching the velocities of the beams, collision energies from up to roughly 210 cm^{-1} down to 0.007 cm^{-1} were achieved. The experiments studied Penning ionizing collisions by detecting the resulting ions [22–25].

Jankunas *et al.* performed merged beam experiments with two bent guides. One beamline comprised a temperature-controlled Even-Lavie valve in combination with a bent magnetic guide to create cold, state-selected beams of metastable neon or helium atoms. A second beamline, originating from a

solenoid valve (General Valve Series 9), consisting of NH_3, ND_3, CH_3F, or CHF_3 molecules, either neat or seeded in noble gases, is sent through a bent electric guide, such that the two beams overlap and have an average scattering angle of 0°. Jankunas *et al.* studied Penning ionizing collisions between these metastable noble gases and these symmetric top molecules, with collision energies in the range of 0.02–161 cm^{-1}, by detecting the resulting ions [26–31].

Another example of merged beam experiments studied collisions between H_2^+ and H_2 molecules [32]. The basis for the experiment are two beams of neutral hydrogen molecules, under a small angle, released by temperature-controlled home-built pulsed valves. Hydrogen molecules in one of the beams are prepared in a highly ($n > 20$) excited Rydberg state. The resulting molecule has a very large electric dipole moment and can thus easily be manipulated by electric fields. The beam was deflected by an on-chip surface-electrode Rydberg-Stark deflector in order to merge the two beams. Since the Rydberg electron is in a high orbit, it is not involved in the collision, but instead shields the collision volume from stray electric fields. The resulting $H_2^+ + H_2 \rightarrow H_3^+ + H$ reaction is measured by detecting the resulting H_3^+ ions. Integral collision cross sections were measured in the energy range of 3.5–42 cm^{-1}.

The last method that will be discussed here is CRESU (Cinétique de Réaction en Ecoulement Supersonique Uniforme, or Reaction Kinetics in Uniform Supersonic Flow in English), which in some sense can also be regarded as a merged beam experiment. In this method, a uniform buffer gas flow is created using a Laval nozzle. Unlike the supersonic beams in the experiments described above, sufficient collisions occur in the flow to keep the gas in thermal equilibrium throughout the expansion, thus the gas will have a well-defined temperature. The temperature in the flow is determined by the shape of the nozzle and the choice of buffer gas [33]. Typically, one of the collision partners is mixed in the buffer gas, while the other is produced by laser excitation or dissociation from a precursor also mixed in the buffer gas. Then, from the time evolution of various state populations, rate constants can be determined for the various collision channels. Initially used to study reactions with ions [34], Sims *et al.* employed it to study collisions of CN radicals with O_2 molecules and NH_3 molecules at temperatures between 9 and 205 cm^{-1} [35]. According to Sims *et al.*, the main limitations of the method are that (1) the interaction time is limited because of the high typical beam velocities, meaning that only reactions with high rate constants can be studied, (2) the collision energy is limited by condensation in the beam due to the high typical densities, and (3) a new nozzle has to be constructed for different flow conditions. Recently rotational energy transfer was studied for CO + Ar collisions between 30 and 293 K (21-204 cm^{-1}) [36]. As can be seen, this technique allows a wide range of collision energies to be studied at conditions very similar to those in interstellar gas clouds.

1.3.3 Controlled collisions with a Stark decelerator

By slowing seeded molecular beams with a Stark decelerator, cold packets of molecules with controlled velocities ranging from tens to hundreds of meters per second can be produced. These packets are ideal for collision studies: The narrow energy distribution of the packet is important for attaining a good energy resolution, while the ability to tune the velocity allows one to vary the collision energy over a wide range. Furthermore, the high state purity makes it possible to measure the collision products virtually background-free. In an early experiment, Gilijamse *et al.* measured state-to-state inelastic cross sections between Stark decelerated packets of hydroxyl radicals (OH) and packets of xenon atoms from a cooled pulsed valve under a 90 degree angle in an energy range of 50–400 cm^{-1} [37]. The first bi-molecular collisions were measured by Kirste *et al.*, using a Stark decelerated beam of hydroxyl radicals, and a hexapole-focused beam of nitric oxide molecules (seeded in xenon) [38]. State-to-state inelastic cross sections were measured in the energy range of 70–300 cm^{-1}.

The addition of velocity map imaging [39, 40] to the experiments allows not only the integral, but also the differential cross section, i.e., the cross section as a function of scattering angle, to be measured. Von Zastrow measured collisions of Stark-decelerated nitric oxide molecules at a fixed velocity with several nobles gas atoms in free expansions, at collision energies of 630 cm^{-1} for helium, 485 cm^{-1} for neon, and 450 cm^{-1} for argon [41]. With a carefully chosen detection scheme, very sharp images of the differential cross section were produced, showing diffraction oscillations for the state-to-state inelastic collisions. Vogels *et al.* studied collisions of Stark decelerated nitric oxide molecules with beams of helium atoms from a cooled Even-Lavie valve, at a scattering angle of 45° [42]. They measured the differential cross section for state-to-state inelastic collisions at several collision energies between 13 and 45 cm^{-1}, a range in which collision resonances are predicted by theory. The effect of these resonances were clearly visible in the differential cross sections. Recently, Onvlee *et al.* studied collisions with a Stark-decelerated beam of nitric oxide molecules at a fixed velocity colliding with beams of rare-gas atoms at 180°, and imaged Fraunhofer scattering [43].

1.3.4 Sensitive collision measurements using trapped particles

Great sensitivity can be achieved by studying collisions between molecules in a beam and particles in a trap. In contrast to crossed molecular beam experiment, collision signal can be accumulated over a long time.

This was first demonstrated by Willitsch *et al.*, who collided Ca^+ ions in a Coulomb crystal in a Paul trap with a beam of CH_3F molecules to measure $Ca^+ + CH_3F \rightarrow CaF^+ + CH_3$ reactions [44, 45]. The CH_3F is produced from a thermal effusive beam followed by a quadrupole guide for velocity selection

of CH_3F molecules. Very low velocities were selected, corresponding to kinetic energies of only 2–3.7 K. While the density of such a beam is very low (between 10^5–10^6 molecules per cm^3), this was compensated by the fact that the Ca^+ ions were trapped for up to two hours and that individual reactions could be detected by counting the number of Ca^+ ions in the trap. Chang *et al.* used a similar technique to study reactions of Ca^+ ions with two conformers of 3-aminophenol [46]. The 3-aminopherol molecules were seeded in neon for a slower supersonic beam. The beam was then deflected using electric fields. Since the two conformers have different electric dipole moments, this allowed selecting which conformer collided with the Ca^+ ions. Conformer specific reaction rates were measured.

Another example is an experiment performed by Sawyer *et al.* [47] in which hydroxyl radicals, seeded in krypton, Stark decelerated to standstill and trapped in a magnetic trap for up to 170 ms, were collided with beams of ND_3 molecules, velocity selected with a curved hexapole guide, from a cryogenic helium buffer gas source. They measured, at a collision energy of about $3\,cm^{-1}$, the trap-loss cross section with and without external electric field. With electric field, the cross section for trap-loss collisions between these dipolar molecules was found to increase.

Likewise, Strebel *et al.* [48] studied collisions of lithium atoms with rare gas atoms and SF_6 molecules, in an energy range of 2–200 K. A cloud of lithium atoms was trapped in a magnetic-optical trap at a temperature of ~ 1 mK. Beams of rare gas atoms and SF_6 molecules were released from a fast rotating nozzle. Since the nozzle has a well-controlled velocity in the laboratory frame, in the direction opposite to the molecular beam direction, the resulting beams reached velocities as low as 50 m/s (up to 750 m/s). They measured both integral and differential elastic collision cross sections by measuring trap loss and differential scattering signals. The quantum wave nature of the collisions was revealed by the measured rainbow features and orbiting resonances.

1.4 Development of the molecular synchrotron

This thesis described collision experiments that have been performed with a molecular synchrotron. In order to provide context and a better understanding of its essential features, this section describes the development of the molecular synchrotron.

The basic idea for the first storage ring for polar molecules was simple enough: If a hexapole can transversely focus a beam of polar molecules, it should in principle be possible to build a storage ring by taking a single long hexapole, and bend it into a circle [52]. And this is exactly what Crompvoets *et al.*, working at (the former) FOM Institute Rijnhuizen in Nieuwegein, demonstrated experimentally [49, 53]. Figure 1.4 shows a sketch of the 125 mm radius ring. This storage ring was able to store a packet of ND_3 molecules, prepared by an injection beamline consisting of a Stark decelerator and several focusing

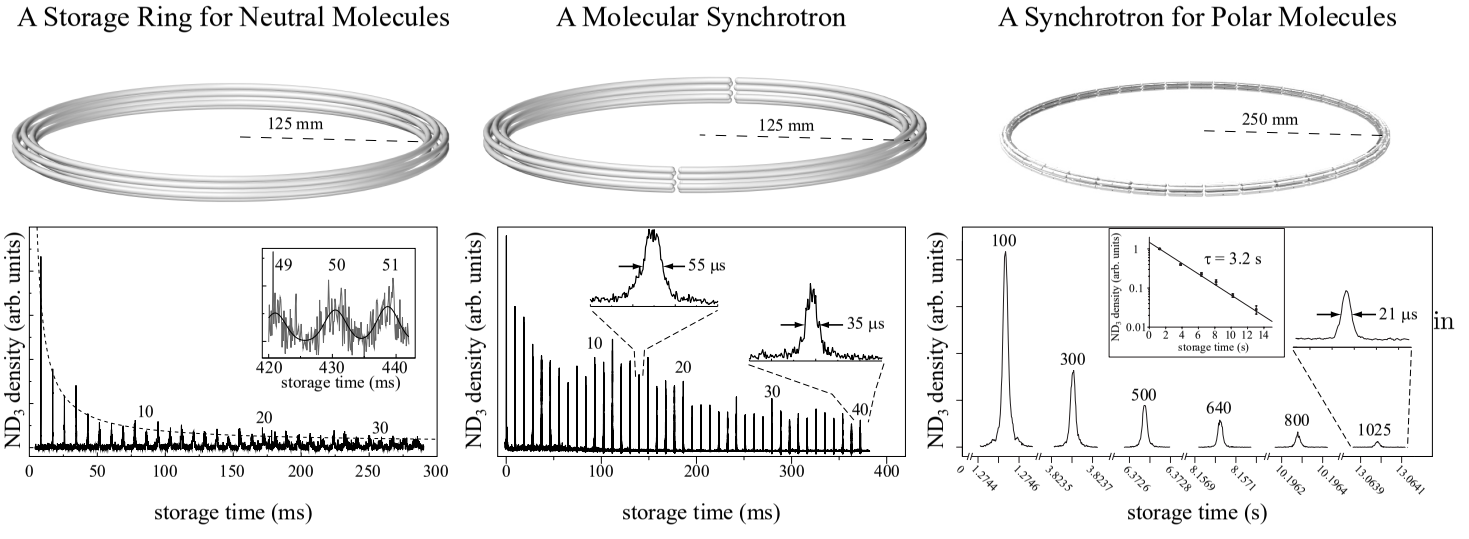

Figure 1.4 – Overview of three generations of storage rings. For each generation, the figures shows the title of the thesis in which the rings are demonstrated, a render of the ring, and a time-of-flight measurement of the revolving packets of ND_3 molecules after a variable number of round-trip. Figure is adapted from [49–51].

elements, for about 50 round-trips. Since the ring was cylindrically symmetric, no forces could be applied to the trapped molecules in the longitudinal direction. The packet would thus disperse over time, until the packet of molecules would fill the ring homogeneously. A time-of-flight measurement is shown in Figure 1.4. Note that the width of the packet, after being stored for 430 ms, is several milliseconds.

In order to be able to keep the molecules in a tight packet, the design for the second generation storage ring consisted of two hexapole half-circles, separated by a 2 mm gap. By switching the voltages on the two halves appropriately as the molecules pass through the gaps from one half to the other, a longitudinal bunching force was applied to the molecules. And indeed, Heiner *et al.*, working at the Fritz-Haber-Institut der Max-Planck-Gesellschaft in Berlin, demonstrated experimentally that the stored packet of ND_3 molecules could be kept together for more than 100 round-trips, establishing the first synchrotron for polar molecules [50, 54, 55]. A rendering of the ring is shown in Figure 1.4, together with time-of-flight measurements performed on the trapped molecules. Note that in this case, the width of the packet, after being stored for almost 400 ms, is only 35 μs. As a second benefit, the fact that the two halves could be switched individually means that it was possible to inject a second packet of ammonia without losing the packet that was already stored.

Finally, Zieger *et al.* demonstrated the third generation ring [51, 56, 57], which was constructed and demonstrated at the FHI in Berlin and took the idea of partitioning the ring even further: This ring consists of 40 straight hexapole elements arranged in a circle with a radius of 250 mm (see Figure 1.4), and brings another set of important improvements. The factor that limits the velocity at which molecules can be trapped, are the voltages necessary to confine the molecules on a circular orbit: voltages of already ± 5 kV were applied to the second generation storage ring in order to store ND_3 molecules with velocities of 90 m/s on an orbit with a radius of 125 mm. The larger radius of this third generation ring thus allows it to store molecules with higher velocities, of up to 140 m/s, without having to increase the voltages even further. This shows again how weak the interaction of these electric dipoles with the electric field really is.

The fact that the new ring consisted of 40 segments (that can be switched individually) brings about a number of additional advantages. Bunching the molecules up to 40 times per round-trip instead of 2 times results in stronger longitudinal confinement forces. Zieger *et al.* implemented a novel bunching scheme. While resulting in weaker bunching forces, this scheme avoids molecules crossing regions with zero fields, in which molecules are able to make a transition to a different rotational sublevel without a Stark shift, thus being lost from the trap. Furthermore, the higher degree of symmetry of the ring increased the transverse phase-space acceptance, which describes upper limits on the molecules' trappable deviations in position and velocity. Finally, a 40 segment ring can, in principle, store up to 19 packets of ammonia molecules simultaneously. (Due to incoupling considerations, the minimum distance

between two adjacent packets is 2 hexapole elements so that no more than 20 packets can be stored simultaneously. Furthermore, two additional hexapole elements have to be temporarily turned off in order to let a packet of molecules enter the ring. Any packet that would be present in these hexapoles would be lost. Hence, the maximum number of packets that can simultaneously stored is 19.)

The first attempt to observe collisions was carried out using this third generation storage ring (second generation synchrotron) [51]. After demonstrating the storing capabilities of this new synchrotron, it was upgraded with a second injection beamline that injected packets of molecules flying in the opposite direction. This allowed it to store up to 13 packets of molecules traveling in each direction, so 26 in total, limited by the wiring of the injection hexapoles that are turned off in order to allow the molecules to enter the ring. The idea here is that every packet of molecules will, during each round-trip, encounter all packets revolving in the opposite direction twice. Storing the molecules for hundreds of round-trips thus would lead to a very high sensitivity for detecting collisions between the ammonia molecules. Unfortunately, the densities of the stored ammonia packets proved to be too low to result in detectable amounts of collisions, even after so many encounters.

Shortly after these measurements, the synchrotron was moved to the Vrije Universiteit Amsterdam, as did I, and a new project to study collisions using a molecular synchrotron started.

1.5 Summary and outlook

This work draws inspiration from experiments with merged beams that allow low energy collisions to be studied and experiments with trapped particles that result in high sensitivities. Cold, velocity controlled packets of ND_3 are created by combining a seeded supersonic expansion of 5% ND_3 in xenon (350 m/s) with hexapoles for transverse focusing, a Stark decelerator for deceleration (to 100–140 m/s), and a buncher for longitudinal focusing of ammonia molecules in the low-field seeking sublevel of the $J = 1$, $K = 1$ ro-vibrational ground state. The synchrotron itself consists of 40 hexapole elements that continuously focus (i.e. trap) the molecules in the transverse direction, while appropriate switching of the high-voltages applied to the hexapoles contain the molecules in the longitudinal direction (like in the buncher).

We apply the synchrotron to the study of collisions by adding to it an additional beamline with collision partners. These collision partners will not have an electric dipole moment, and thus will not be influenced by the fields that confine the ammonia molecules. Rather, they fly straight through, crossing the trajectory of the trapped ammonia molecules at the so-called collision zone.

The central idea of this thesis, then, is that aligning the supersonic beams with collision partners in a tangential and co-propagating fashion, similar to the merged beam experiments, should allow measurement of the relative, total,

integrated, collision cross sections for ND_3 + Ar collisions at low collision energies, its sensitivity strongly enhanced by storing the ammonia packets for many round-trips.

Chapters 2 and 3 describe the experiments on which this thesis is based, and their results. Both chapters describe the same experiments, and in fact some of the figures are identical, but their focus is different. While Chapter 2 explains the general principles of the experiment, its focus is on the result: a proof of principle in the form of a measurement of the relative, total, integrated cross sections for ND_3 + Ar collisions in the energy range of 40–140 cm^{-1}. These results are compared with theoretical calculations by Loreau *et al.* [58].

Obtaining these experimental results, however, required extensive calibration of our setup. Furthermore, trajectory simulations of the ammonia molecules played a crucial role in the interpretation of the measurements. These more technical aspects are covered in detail in Chapter 3.

Together, Chapters 2 and 3 give a complete picture of the experiment, and confirm that these ideas about measuring collisions in a synchrotron are correct and feasible to execute in the laboratory. By allowing the study of cold, and specifically elastic collisions, the method of studying collisions using a synchrotron complements the existing range of techniques to study cold collisions.

The setup is not without its limitations, however. So far, only ND_3 has been stored in the synchrotron, so that only collision studies with ND_3 (and specifically ND_3 molecules in the low-field seeking substate of the $J = 1, K = 1$ ro-vibrational ground state) can be performed. More important is that the collision studies are limited to collision energies too high to be able to see interesting structure such as resonances in the collision cross sections, due to the low velocity of the ammonia molecules in the ring (100–140 m/s) with respect to their collision partners (400–600 m/s).

There are several paths forward from here, two of which stay relatively close to home: A similar synchrotron could be built with a larger radius, so that faster ammonia molecules can be stored (ideally with a velocity on the order of 400 m/s). Alternatively, a cryogenic beam source could be used to create beams of around 100 m/s which can be made to collide with the stored ammonia packets.

A radically different approach would be to build a magnetic analog of the synchrotron used for the experiments in this work, capable of storing beams of hydrogen atoms at velocities up to 600 m/s. Not only does this mean that the atoms will be able to be injected into the synchrotron directly from a supersonic beam source, leading to much larger densities, but also that in a collision experiment much lower relative velocities and thus collision energies can be reached. This will allow for studying very cold collisions with the most common species found in space (atomic hydrogen). A possible design for a magnetic storage ring is discussed in Chapter 4 of this thesis.

CHAPTER 2

Cold collisions in a molecular synchrotron[1]

We study collisions between neutral, deuterated ammonia molecules (ND_3) stored in a 50 cm diameter synchrotron and argon atoms in co-propagating supersonic beams. The advantages of using a synchrotron in collision studies are twofold: (i) By storing ammonia molecules for many round-trips, the sensitivity to collisions is greatly enhanced; (ii) The collision partners move in the same direction as the stored molecules, resulting in low collision energies. We tune the collision energy in three different ways: by varying the velocity of the stored ammonia packets, by varying the temperature of the pulsed valve that releases the argon atoms, and by varying the timing between the supersonic argon beam and the stored ammonia packets. These give consistent results. We determine the relative, total, integrated cross section for $ND_3 + Ar$ collisions in the energy range of 40–140 cm^{-1}, with a resolution of 5–10 cm^{-1} and an uncertainty of 7–15%. Our measurements are in good agreement with theoretical scattering calculations.

[1]Based on Aernout P. P. van der Poel, Peter C. Zieger, Sebastiaan Y. T. van de Meerakker, Jérôme Loreau, Ad van der Avoird, Hendrick L. Bethlem, *Cold Collisions in a Molecular Synchrotron*, Physical Review Letters **120**, 033402 (2018).

2.1 Introduction

The crossed molecular beam technique, pioneered by Dudley R. Herschbach and Yuan T. Lee, has yielded a detailed understanding of how molecules interact and react [59, 60]. Until recently, these crossed molecular beam studies were limited by the velocities of the molecular beams to collision energies above a few $100\,\mathrm{cm}^{-1}$ ($1\,\mathrm{cm}^{-1} \simeq 1.4\,\mathrm{K}$). Over the past years, however, a number of ingenious methods [13–15] have been developed to study collisions in the cold regime. These advances are important for several reasons. Firstly, the temperatures of interstellar clouds are typically between 10–100 K; collision data of simple molecules at low temperatures is thus highly relevant for understanding the chemistry in these clouds [61]. Furthermore, quantum effects become important at low temperatures, where few partial waves contribute and the de Broglie wavelength associated with the relative velocity becomes comparable to or larger than the intermolecular distances. Of particular interest are resonances of the collision cross section as a function of collision energy [3, 62–64]. The position and shape of these resonances are very sensitive to the exact shape of the PES and thus serve as precise tests of our understanding of intermolecular forces.

The ability to control the velocity of molecules using time-varying electric fields has allowed studies of inelastic collisions of OH and NO molecules with rare gas atoms at low collision energies [37, 38, 42, 65]. Using cryogenically cooled beams under a small (and variable) crossing angle, inelastic collisions of O_2 and CO with H_2 and He at energies between 5 and 30 K have been studied [66].

Even lower temperatures can be obtained by using magnetic or electric guides to merge two molecular beams into a single beam. This technique has been used to study Penning ionization reactions of various atoms and molecules with metastable helium [22, 25, 28, 67] and collisions between ground state hydrogen molecules and hydrogen molecules in high Rydberg states [32].

In a different approach, trapped ions at millikelvin temperatures are monitored while slow, velocity selected, beams of molecules pass through the trap to study reactive ion-molecule collisions [45, 46]. The ions are stored for a long time and their number can be accurately determined, which allows the study of reactions with rates as small as one per minute. In a similar fashion, collisions of slow beams of ammonia with magnetically trapped OH molecules were observed [47], as were collisions of slow beams of rare gas atoms and SF_6 with lithium in a magneto-optical trap [48].

Here, we study collisions between neutral ammonia molecules stored in a synchrotron and beams of argon atoms. Using a synchrotron for collision studies offers two advantages: First, the collision partners move in the same direction as the stored molecules, resulting in a small relative velocity and thus a low collision energy. Second, the sensitivity to collisions is enhanced by storing the ammonia molecules for many round-trips. Our approach thus combines the low collision energies obtained in experiments that use merged

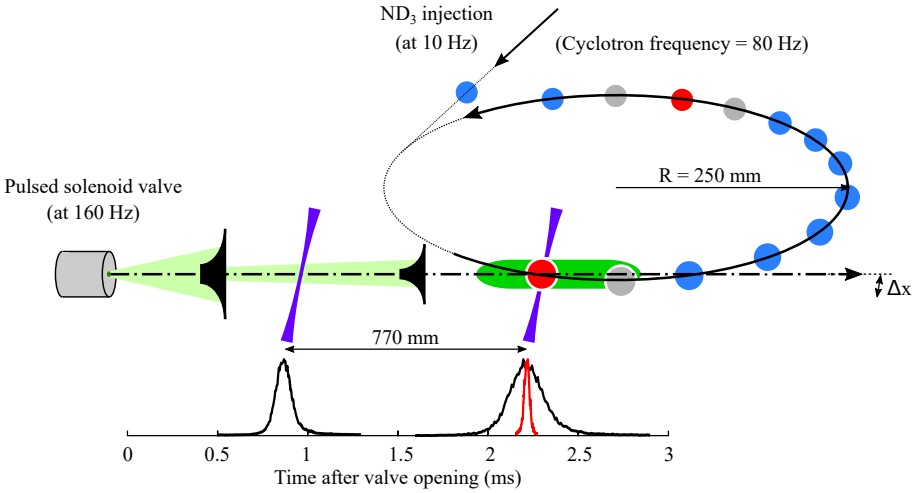

Figure 2.1 – Schematic view of the synchrotron and beamline. Supersonic beams from a cooled Even-Lavie valve intersect the synchrotron a quarter round-trip downstream from the injection point. The argon beam is displaced from the equilibrium orbit by a distance Δx. The packets of argon (shown in green) are timed such that the *probe* packets (shown in red) encounter an argon packet on every round-trip, while *reference* packets (shown in blue) provide a simultaneous measurement of background loss. Bottom: In order to determine the velocity distribution of the argon beams, the time-of-flight spectra are recorded (i) 770 mm before the synchrotron and (ii) inside the synchrotron (black curves). For reference the time-of-flight profile of a packet of ammonia after making 90 round-trips is also shown (red curve).

molecular beams [22, 25, 28, 67] with the high sensitivity of experiments that monitor trap loss [45–48].

2.2 Experimental setup

The synchrotron used in our experiment is shown schematically in Fig. 2.1. It consists of 40 electric hexapoles arranged in a circle with a diameter of 0.5 m, to which voltages of up to ±5 kV are applied. With these settings, we store packets of ND_3 molecules in the low-field seeking sublevel of the J=1, K=1 rovibrational ground state with velocities in the range of 100–150 m/s. At any time during the experiment, 14 packets of ammonia molecules are held by the synchrotron. Each packet of this train is stored for up to 1.2 s, while at a 10 Hz rate new packets are being injected in front of the train and packets at the back of the train are being detected (and hence ejected). More details on the synchrotron and injection beam line can be found in Zieger *et al.* [56, 57, 68].

The stored packets of ammonia molecules are made to collide with beams of argon atoms released by a pulsed Even-Lavie valve [69], which can be operated at temperatures between −150 and +30°C. The pulsed valve is operated at

160 Hz, 2 times the cyclotron frequency of the stored ammonia packets, such that every tenth ND_3 packet will encounter a fresh argon packet every round-trip. We will refer to these packets as *probe* packets. Packets that do not encounter the argon beam, referred to as *reference* packets, provide a simultaneous measurement of background loss. Collisions between stored ammonia molecules and argon atoms will (almost always) cause ammonia molecules to be lost from the trap as the longitudinal and transverse trap depths are much smaller than the collision energies. The argon beam is displaced from the equilibrium orbit of the stored ammonia molecules by about 1.6 mm such that it intersects the path of the ammonia molecules twice. This simplifies the analysis (*vide infra*).

As shown in Fig. 2.1, the relative intensities of the argon beams are monitored at two positions: 480 mm downstream from the valve and inside the detection zone of the synchrotron, 1250 mm downstream from the valve. The argon atoms are detected by 3+1 Resonance-Enhanced Multi-Photon Ionization (REMPI) *via* the $3s^2 3p^5(^2P_{1/2})4s$-state [70] using a pulsed UV laser running at 314 nm. The arrival time distributions measured at the two detection zones are used to derive the longitudinal velocity distributions. The black curves in Fig. 2.1 show typical time of flight profiles measured in both detection zones for an argon beam at a valve temperature of -150°C. For reference, the time-of-flight profile of a packet of ammonia after making 90 round-trips is also shown (red curve).

2.3 Results and discussion

Fig. 2.2 shows the number of ammonia molecules in the probe beam (red squares) and reference beam (blue squares) as a function of storage time. Note that the error bars reflecting the statistical spread of the ion signal are (in most cases) smaller than the symbols. In this particular experiment, hydrogen molecules are used as collision partner rather than argon atoms. The solid lines show the result of fits to the data using the expression $n = n_0\, e^{-k \cdot RT}$, with n the number of detected ions per shot, RT the number of round-trips the packets have made before being detected, and k the loss rate. For the reference packets we find a loss rate of $1.41 \pm 0.08\%$ per round-trip, corresponding to a lifetime of 1.0 s. For the probe packets, we find a loss rate of $2.67 \pm 0.11\%$ per round-trip, which implies that collisions with the supersonic beam induce an additional loss rate of $1.26 \pm 0.14\%$ per round-trip.

The orange data points in the lower panel of Fig. 2.2 show the loss rate due to collisions calculated from the number of ions detected in the probe and reference beams at specific round-trip numbers, using $k_{\mathrm{col}} = -\ln(n_{\mathrm{probe}}/n_{\mathrm{ref}})/RT$. The error bars reflect the statistical spread of the ion signal. The uncertainty of k_{col} decreases dramatically during the first round-trips and reaches an optimum after $\sim$70 round-trips, at which point only 14% of molecules in the probe beam remain. When the storage time is increased further, the uncertainty

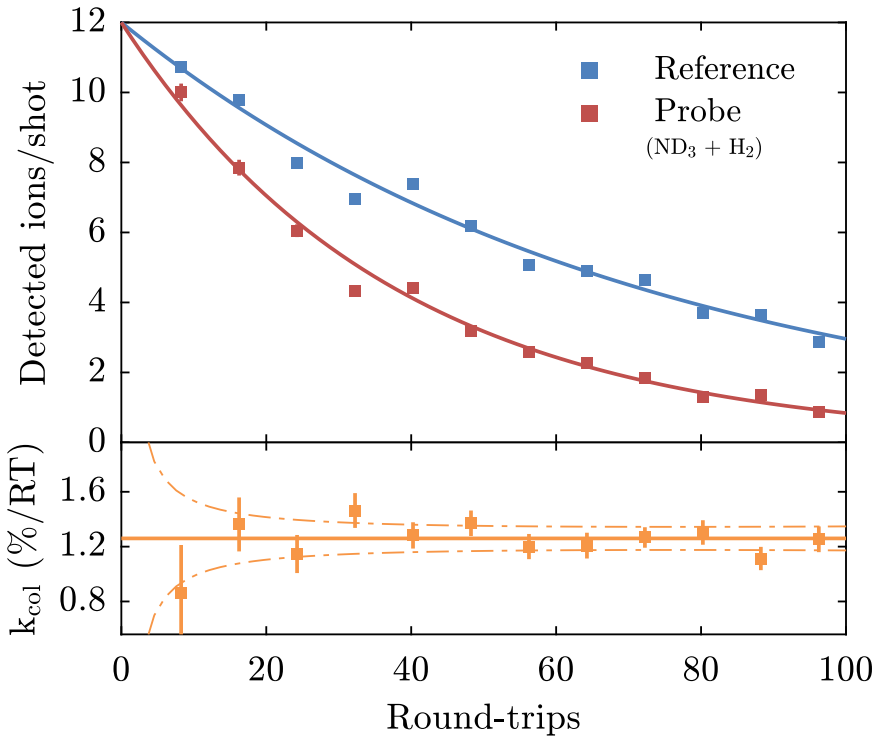

Figure 2.2 – Upper frame: Number of detected ND_3 ions per shot as a function of the number of round-trips spent in the synchrotron, for both the probe (red) and the reference packets (blue). Each data point is an average over 3240 (reference) or 360 (probe) shots. The solid lines denote exponential fits. Most of the error bars are obscured by the data points. Lower frame: From ratios of the numbers of detected ions, the loss rate due to collisions can be determined at each number of round-trips. The dash-dotted lines show the expected statistical uncertainty based on the number of detected ions per shot. In both frames, the error bars depict 68% confidence limits. In this particular experiment, hydrogen molecules are used as collision partner rather than argon atoms.

of the measured probe beam intensity becomes the limiting factor and the uncertainty of k_{col} increases. The orange dash-dotted lines show the expected statistical uncertainty, assuming the number of detected ions is governed by Poisson statistics, which is in good agreement with the experimental results. Note that the deviations from a perfect exponential decay of the probe and reference signals observed in the upper panel of Fig. 2.2 are absent in the extracted loss rate shown in the lower panel. This is a crucial feature of our method: fluctuations due to, for instance, intensity and/or wavelength drifts of the laser, temperature variations of the valve, or collective oscillations of the packet inside the synchrotron are common to the reference and probe signals and are divided out.

Of critical importance is the delay between the trigger of the valve that releases the argon atoms and the arrival time of the ND_3 probe packet in the detection zone. This delay determines whether the ammonia molecules collide with atoms located more in the leading or trailing end of the argon packet, or, in fact, whether they collide at all. Furthermore, as the flight time from the valve to the synchrotron is much larger than the opening time of the valve, there is a strong correlation between the position of the argon atoms and their velocity. Hence, the delay determines the velocity of the argon atoms that are encountered by the ammonia beam.

The loss rates of ND_3 molecules (with velocities of 121.1 m/s and 138.8 m/s) due to collisions with argon atoms (with velocities around 570, 524, 475, and 422 m/s) were measured as a function of the aforementioned delay. Each data point is the result of 2,400 shots–corresponding to a measurement time of 4 minutes. To be robust against possible drifts of the argon beam density, the data were taken while toggling between the two ammonia speeds after every data point and picking the timings from a list in a random order.

The results for an ammonia velocity of 121.1 m/s with beams of argon with average velocities of 570 and 422 m/s are shown in Fig. 2.3. Each measurement can be seen to feature two peaks, resulting from the fact that the argon beam intersects the synchrotron at two distinct locations. These peaks become less well resolved as the argon packets become slower and concomitantly longer.

Additional data were taken at three specific timings for both ammonia velocities. These data are shown as the colored symbols in Fig. 2.3. Each of these is the result of 21 600 shots, corresponding to a measurement time of 36 min per point. To detect and correct for possible drifts of the argon beam density, we cycled nine times through the six different configurations. No significant drifts were detected.

The solid curves in Fig. 2.3 show results of a simulation of our experiment. The simulation uses as input (i) the longitudinal position and velocity distributions of the argon beams taken from the time-of-flight profiles at two locations, (ii) the shape and size of the cross section of the argon beams taken from measurements where the height of the laser beam was scanned, from measurements where the position of the valve was scanned, and from the geometry of our beam machine, (iii) the horizontal displacement of the argon beam from the equilibrium orbit determined from the time difference between the maxima in the measured loss rates, and (iv) the velocity and equilibrium radius of the synchronous molecule taken from simulations of the synchrotron [68]. For each combination of valve temperature and ammonia velocity, the simulated curves are scaled vertically to fit the black data points in Fig. 2.3. As seen from the figure, the simulations describe the measurements very well, which confirms that we have an excellent understanding of the experiment.

The scaling factors obtained by fitting the simulations to the measurements are the products of the collision cross sections and the absolute column densities of the argon beams at the corresponding valve temperatures. Hence, by dividing the scaling factors by the relative column densities of the argon

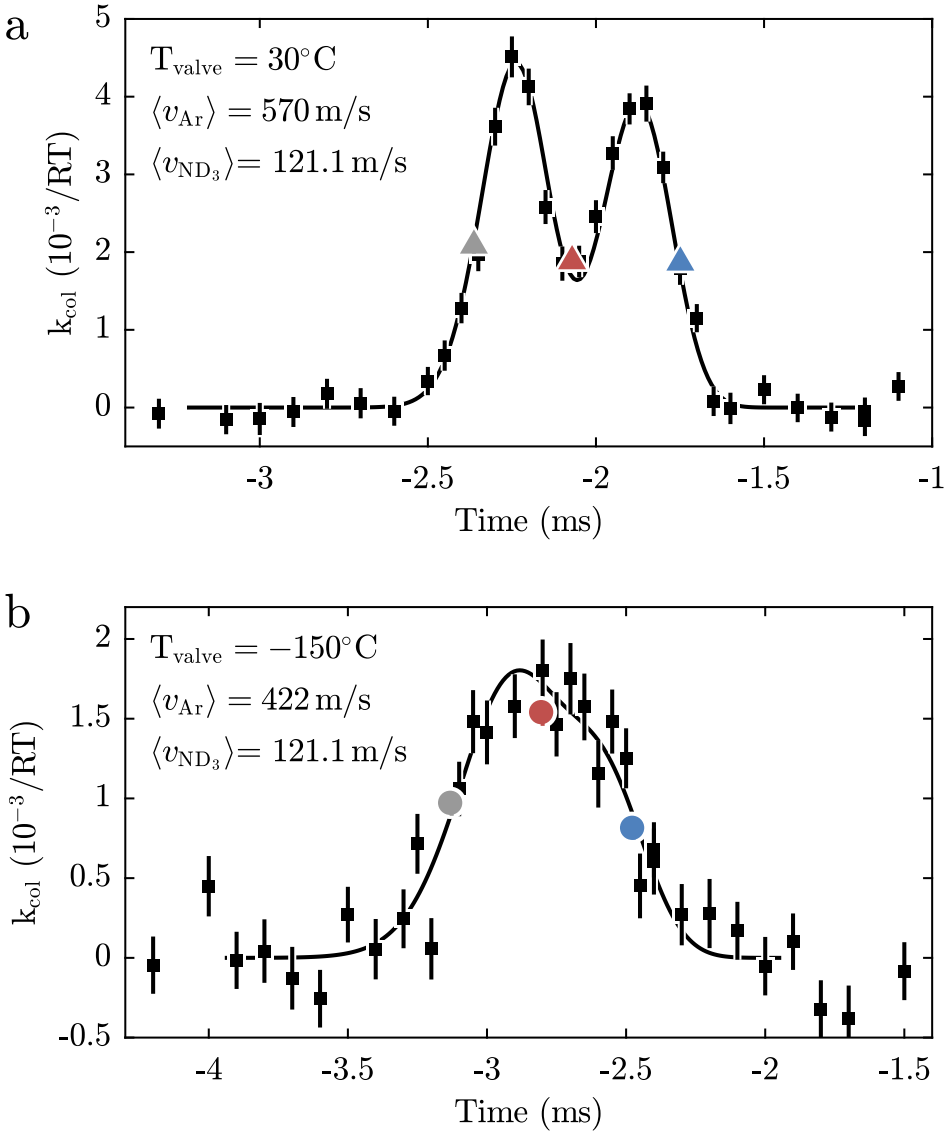

Figure 2.3 – ND_3 loss rate due to collisions with argon atoms versus timing of the valve that releases the argon atoms, for two different valve temperatures. The black squares consist of 2400 shots each, the colored points of 21 600 shots each. The lines depict results of a simulation of the experiment, individually scaled to fit the data (see the main text).

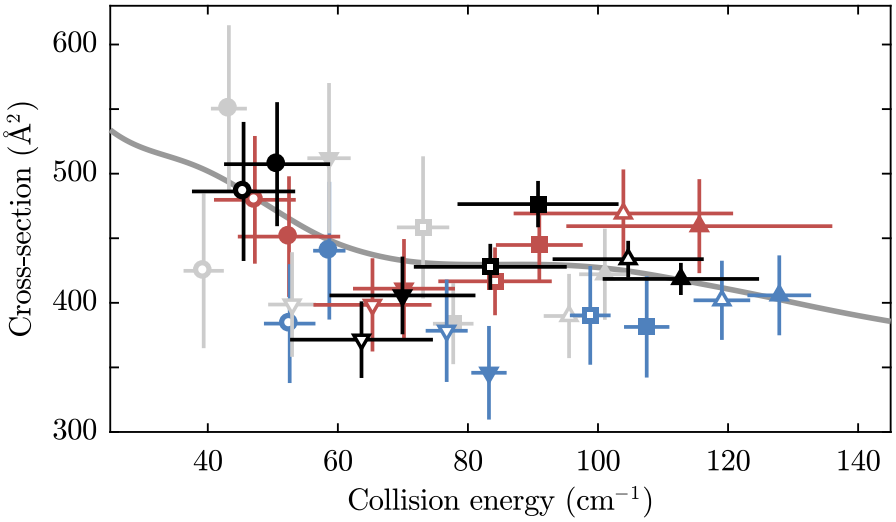

Figure 2.4 – Total, integrated, ND_3 + Ar collision cross section versus collision energy. The collision energy is varied in three different ways (see the main text). The line shows a theoretical calculation [58], convoluted with a normal distribution with a standard deviation of $5\,cm^{-1}$. The measurements are collectively fit to this calculation with a single global scaling factor.

beams, derived from time-of-flight measurements in the detection zone of the synchrotron, we obtain the relative total cross sections. We correct for the fact that a small but significant fraction of the elastic collisions does not eject molecules from the ring; see Appendix A. The resulting cross sections are shown as the black data points in Fig. 2.4. The blue, red, and gray points in Fig. 2.4 are found by scaling the simulations to the data points measured at the front, center, and back of the argon packet (the colored points shown in Fig. 2.3). The vertical error bars represent the statistical uncertainties of the measurements (the standard error), ranging from 7 to 15%, while the horizontal error bars represent the spread in collision energy, retrieved from the simulations, and range from 5 to $10\,cm^{-1}$. The data taken in the fast part of the beam (the blue datapoints) have the best energy resolution. The data points taken by averaging over the entire velocity distribution have smaller uncertainties but their energy resolution is worse. The collision cross sections determined from the different data sets agree with each other within their combined errors, although the cross sections retrieved from colliding ammonia molecules with the fast part of the argon beam (blue data points) appear to be systematically smaller than the cross sections retrieved from colliding ammonia molecules with the slow or center part of the argon beam.

The solid line depicted in Fig. 2.4 is the result of theoretical calculations described in Ref. [58], convoluted with a normal distribution with a standard deviation of $5\,cm^{-1}$. The measurements are collectively fit to this calculation

with a single global scaling factor that represents the density of the argon beam at T = −150°C, which is found to be $7.8{\times}10^9\,\mathrm{cm}^{-3}$. This density is in agreement with a crude estimate of the density from the REMPI-measurements. In future, we plan to measure the density more accurately using a femtosecond laser [71]. Although the ND_3 + Ar collision cross section in this energy range does not show spectacular features, the shallow minimum around $70\,\mathrm{cm}^{-1}$ predicted by theory is reproduced in the experiment.

2.4 Conclusions

In conclusion, we have performed collision experiments between argon atoms in a supersonic beam and ND_3 molecules stored in a synchrotron. Our measurements demonstrate that storing molecules for many round-trips increases the sensitivity dramatically, and that co-propagating beams allow low collision energies to be studied, hence providing a robust and general method to measure the total cross section for low energy collisions. Our method has a number of additional features that make it attractive. (i) By comparing packets that are simultaneously stored in the synchrotron, the measurements are independent of the ammonia intensity and immune to variations of the background pressure in the synchrotron. (ii) As the probe packets interact with many argon packets, shot-to-shot fluctuations of the argon beam are averaged out. By toggling rapidly between different ammonia velocities and timings, slow drifts of the argon beam intensity are eliminated.

The collision energy is currently limited by the large difference between the velocity of the stored molecules and the velocities in the supersonic beam. Lower collision energy could be reached by using molecules from cryostatically cooled beams as collision partner [72] and/or by using a larger synchrotron which would be able to store ammonia molecules at a higher velocity. Ideally, a synchrotron would be used that can store molecules directly from a supersonic beam without deceleration. Furthermore, by storing beams both clockwise and anticlockwise in the synchrotron, it is possible to measure collision energies from 0–$2000\,\mathrm{cm}^{-1}$. Note that, if the velocities of the beams are more similar, the energy resolution will also be improved [24], ultimately limited to ∼10 mK; the temperature of the stored ammonia packets. A higher resolution can also be obtained (at the cost of increasing the collision energy) by crossing the beams at right angles. This would make it possible to resolve the fine-structure on the elastic cross section due to scattering resonances [58]. Finally, collision studies with paramagnetic atoms and molecules such a hydrogen – the most abundant atom in the universe – could be performed in a magnetic synchrotron, as described in Chapter 4.

APPENDIX A

Appendix: Collisions that do not lead to loss

In our experiment, we measure the signal from ammonia molecules stored in a synchrotron while they are made to collide with beams of argon atoms at different speeds. Although most collisions lead to loss, a small but significant fraction of elastic collisions takes place at such large distances that there is very little energy transfer and the ammonia molecules remain trapped in the ring. In order to infer an accurate value for the total, integrated, relative collision cross-section from our measurements, we need to correct for this effect. We do this by combining our knowledge of the trapping potential with the differential collision cross-section (the cross-section as a function of scattering angle) calculated using quantum close-coupling calculations of ND_3-argon collisions.

We first look at the trapping potential experienced by the ammonia molecules. According to measurements and simulations performed by Zieger *et al.* [68], ND_3 molecules in the low-field-seeking component of the $J = 1, K = 1$ state will be lost from the ring if they have a transverse velocity larger than 5 m/s. Hence, an ND_3 molecule with a forward velocity of 121.1 or 138.8 m/s (the two velocities used in the experiment) that travels over the equilibrium orbit with a transverse velocity close to zero, the so-called *synchronous molecule*, will be lost if a collision with an argon atom deflects the molecule from its trajectory by an angle that exceeds 2.36° or 2.06°, respectively. We will refer to this angle as the *maximum deflection angle*. For molecules with a non-zero transverse velocity and/or a displacement from the equilibrium orbit, the required deflection angle may be larger or smaller, depending on whether a collision deflects the molecule towards the equilibrium orbit or away from it. As the position and velocity distributions are symmetric around the position and velocity of the synchronous molecule, the maximum deflection angle for

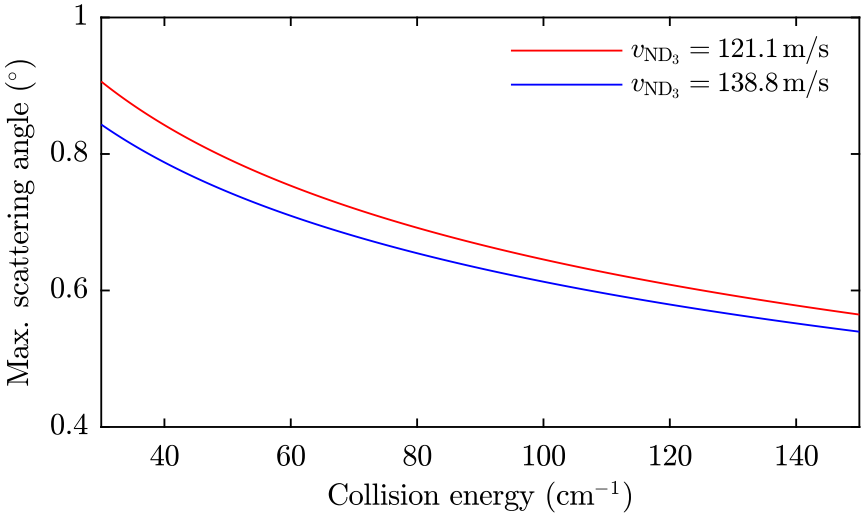

Figure A.1 – Maximum deflection angle in the center-of-momentum frame as a function of collision energy for ammonia molecules traveling with a velocity of 121.1 m/s (red curve) or 138.8 m/s (blue curve) colliding with argon atoms. An ammonia molecule that is deflected by an angle that exceeds this maximum will be lost from the synchrotron.

the synchronous molecule will be taken as the maximum deflection angle for the whole packet. Using the maximum deflection angle in the laboratory frame, we can calculate the corresponding maximum deflection angle in the center-of-momentum frame, which will depend both on the ammonia velocity and the relative velocity. Fig. A.1 shows this angle as function of the collision energy for molecules with 121.1 m/s (black curve) and 138.8 m/s (red curve).

The total elastic cross-section is found from the differential cross-section by integrating over all angles. In contrast, our loss signal is proportional to the differential elastic cross-section integrated over all angles larger than the angle shown in Fig. A.1. If the scattering would be isotropic, the difference between these two quantities would be negligibly small ($\ll$1%). However, the elastic cross-section at intermediate and high collision energies can be sharply forward-peaked (in fact, the reason for the elastic cross-section being much larger than the inelastic cross-sections is because elastic collisions also take place at large impact parameters) and the difference can be significant.

We have performed quantum close-coupling calculations for ND_3 + Ar collisions using the approach described in Ref. [58]. Fig. A.2 shows the inelastic (red curve), elastic (blue curve) and total (black curve) cross-section resulting from these calculations. Note the fine structure in the elastic cross-section, caused by scattering resonances.

Fig. A.3 shows the differential cross-section for elastic collisions resulting from quantum close-coupling calculations calculations for collision energies of

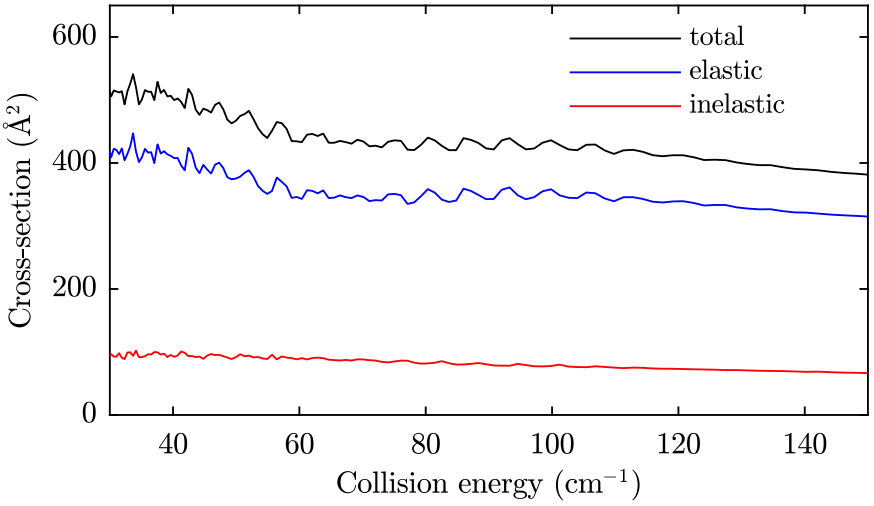

Figure A.2 – Calculated inelastic (red curve), elastic (blue curve) and total (black curve) cross-section for collisions between argon atoms and ND_3 molecules in the low-field-seeking component of the $J = 1, K = 1$ state as function of the collision energy.

30 (black curve) to 150 cm^{-1} (blue curve). As can be seen, the collisions are indeed sharply forward-peaked, particularly at high energy.

Fig. A.4 shows the ratio of (1) the loss cross-section relevant for our experiment, i.e., the cross-section found by integrating the differential inelastic cross-section over all angles and integrating the elastic cross-section over all angles larger than the maximum angle shown in Fig. A.1, and (2) the total cross-section found by integrating the elastic and inelastic cross-section over all angles. The red and blue curves show this ratio for ammonia velocities of 121.1 and 138.8 m/s, respectively. The smooth lines show the correction factor convoluted with a normal distribution with a standard deviation of 5 cm^{-1}. The experimentally measured loss cross-sections should be multiplied by this correction factor to obtain the total cross-section.

As can be seen, the correction is at most 12%. Moreover, the correction factor is not very sensitive to the collision energy and varies at most with 4 percentage points in this range. The reason for this is the fact that while the maximum deflection angle is larger at low energy, the collisions are more sharply forward-peaked at high energy. Thus the two effects cancel partly. As a result, while the uncertainty of the maximum transverse velocity of the ammonia molecules results in an uncertainty of the absolute argon density, it will **not** significantly (<4%) influence the *shape* of the cross-section as a function of collision energy.

In conclusion, a factor has been determined that corrects for the fact that not all collisions lead to loss. As this factor is both close to one and not very

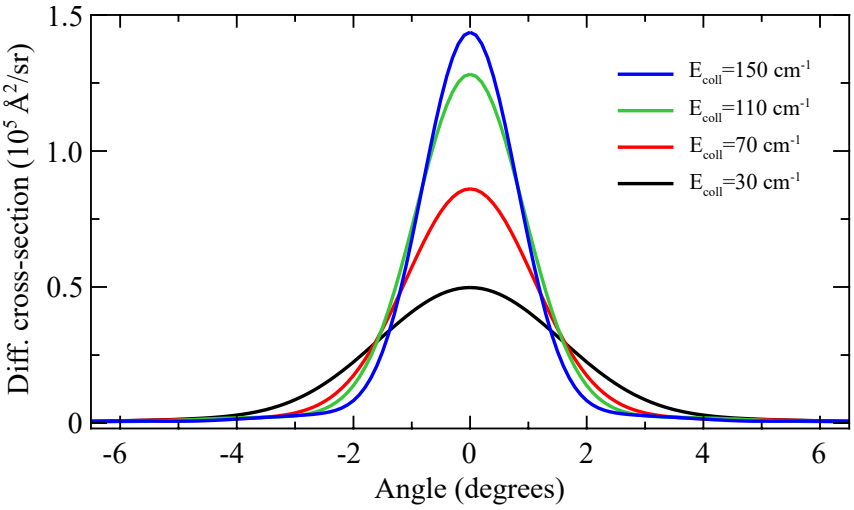

Figure A.3 – Calculated differential cross-section for elastic collisions between argon atoms and ND_3 molecules in the low-field-seeking component of the $J = 1, K = 1$ state.

sensitive to the collision energy, it changes our results only slightly. However, this might not always be the case. On the bright side, if the correction factor is important, it implies that the differential cross-section can be extracted from measurements taken at different ammonia velocities.

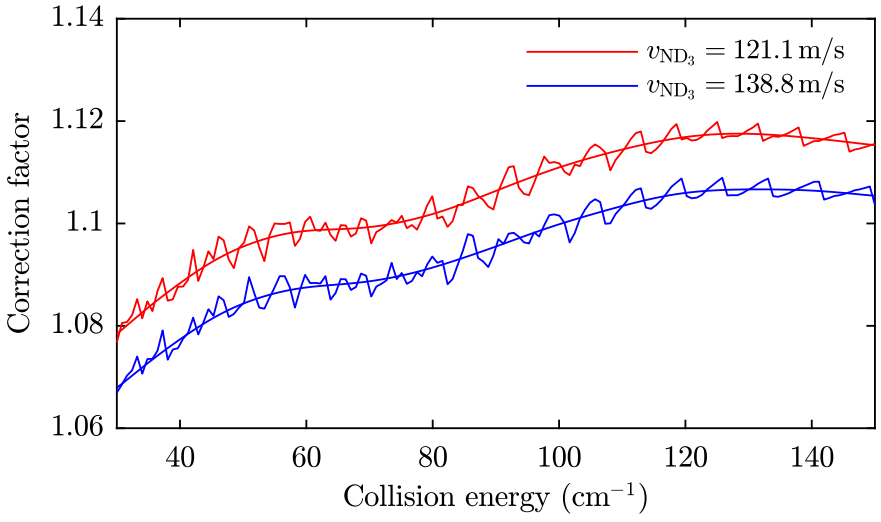

Figure A.4 – Calculated correction factor that accounts for the fact that some elastic collisions will not lead to loss from the synchrotron, for ammonia velocities of 121.1 (red curve) and 138.8 m/s (blue curve). The smooth lines show convolutions of the correction factor, using a normal distribution with a standard deviation of 5 cm^{-1}. The experimentally measured cross-sections should be multiplied by this correction factor to obtain the total cross-section.

Chapter 3

A detailed account on the measurement of cold collisions in a molecular synchrotron[1]

In the previous chapter, we have demonstrated a general and sensitive method to study low energy collisions that exploits the unique properties of a molecular synchrotron. The relative, total, integrated cross sections for ND_3 + Ar collisions in the energy range of 40–140 cm^{-1} were determined from the rate at which ammonia molecules were lost from the synchrotron due to collisions with argon atoms in co-propagating supersonic beams. Where the previous chapter focused on results, this chapter presents the experiments in a more detailed way. In particular, we derive the model that was used to extract the relative cross section from the loss rate, and present measurements to characterize the spatial and velocity distributions of the stored ammonia molecules and the supersonic argon beams.

[1]Based on Aernout P. P. van der Poel, Hendrick L. Bethlem, *A detailed account on the measurement of cold collisions in a molecular synchrotron*, to be submitted.

3.1 Introduction

Collision studies at low temperatures are of interest from both a practical and theoretical viewpoint. Interstellar clouds, which make out a large fraction of our universe, typically have temperatures well below 100 K. Collision data of simple molecules at low temperatures is crucial for understanding the chemistry that goes on in these clouds, which is of special interest because it is from these clouds that solar systems form [61]. Furthermore, at low temperatures the de Broglie wavelength, associated with the relative velocity of the colliding molecules, becomes comparable to or larger than the intermolecular distances and quantum effects become important. Particular interesting are resonances of the collision cross section as a function of collision energy. The position and shape of these resonances are very sensitive to the exact shape of the potential energy surface (PES) and thus serve as precise tests of our understanding of intermolecular forces [3, 62–64]. Precise knowledge of the PES is fundamental to fields such as combustion physics, atmospheric physics, or in fact any field involving chemical reactions.

Although several techniques have been developed to create samples of cold molecules [4, 10, 13], the obtained densities are low (typically 10^8 molecules/cm^3). As the cross sections of collisions involving neutral molecules or atoms are small (typically below 500 Å^2), the main challenge to studying cold collisions is to reach a sufficiently high sensitivity. In recent years, several experiments have managed to measure low energy collisions by leveraging the unique properties of the systems they study. For instance, by exploiting the extreme state-purity of Stark-decelerated beams combined with sensitive ion-detection techniques, van de Meerakker and co-workers have measured quantum-state changing collisions of OH and NO molecules with rare gas atoms to temperatures as low as 5 K [37, 38, 42, 65]. Costes and co-workers have studied inelastic collisions of O_2 and CO with H_2 molecules and helium at energies between 5 and 30 K using cryogenically cooled beams under a small (and variable) crossing angle. Even lower temperatures have been obtained by using magnetic or electric guides to merge two molecular beams. Narevicius and co-workers and Osterwalder and co-workers have exploited the advantages of metastable helium to study Penning ionization reactions with various atoms and molecules [22, 23, 25–27, 29–31, 67]. In a similar fashion, Merkt and co-workers have measured collisions between ground-state hydrogen molecules and hydrogen in highly excited Rydberg states that were merged on a chip [32]. Finally, cold collision have been studied by sending slow beams of atoms and molecules through trapped samples of calcium ions [44, 46], lithium atoms [48] and OH radicals [47], exploiting the fact that collision signal can be accumulated over long time-intervals.

We have developed a method that enables the study of elastic collisions at low energy by exploiting the unique properties of a molecular synchrotron. Our approach combines the low collision energies obtained in experiments that use merged molecular beams with the high sensitivity of experiments that monitor

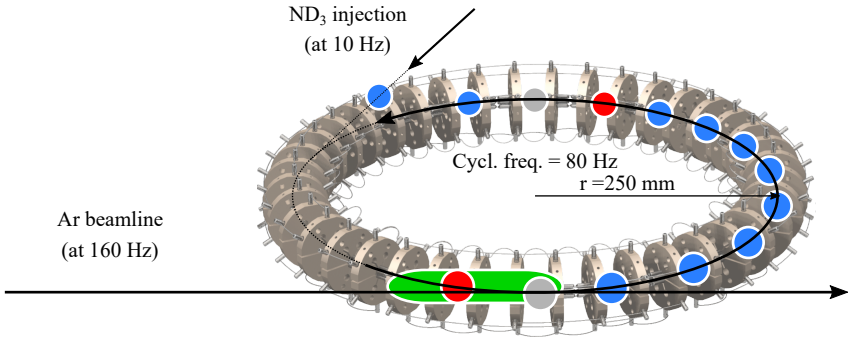

Figure 3.1 – Schematic sketch of the synchrotron and argon beamline. The red circles denote probe packets of ammonia molecules which are targeted by the argon beam (shown in green). The blue circles denote reference packets of ammonia, which do not encounter argon atoms and provide a simultaneous background measurement. The grey circles denote reference packets of ammonia that encounter a tail of the argon beams, and are therefore discarded.

trap loss. In Chapter 2, the total cross section for ND_3 + Ar collisions was determined from the rate at which ammonia molecules were lost from the synchrotron due to collisions with argon atoms in supersonic beams. This chapter provides further details on this experiment. Before going into detail, we will first outline the main principles and virtues of our technique.

3.2 Main principles

In its simplest form, a storage ring is a trap that confines molecules along a circle rather than around a point. As such, a storage ring for molecules in low-field seeking states can be made by bending an electrostatic hexapole focuser into a circle [53]. Since in such a storage ring no longitudinal forces exist to keep the faster and slower molecules together, injected packets of molecules will disperse until the ring is filled homogeneously. A method to prevent this, is by breaking the ring into two half-circles [54] and switch the voltages in such a way that molecules are bunched together as they fly through the gap between the two half rings. The resulting synchrotron was further improved by building up the circle from 40 straight hexapole elements [56, 57, 68]. This has a number of advantages: As the ring has a higher symmetry, instabilities due to the variation of the trapping force are less important and the transverse depth of the ring is larger. Bunching is more effective when it happens 40 times per round-trip; trapping of state-selected, deuterated ammonia molecules (ND_3) in well-defined, mm-sized packets has been demonstrated for up to 10 s. Furthermore, the fact that elements can be switched individually means that different packets can be injected and detected independently, allowing the synchrotron to hold up to 19 packets simultaneously. As the stored packets of ammonia molecules have both a small velocity spread (corresponding to a temperature of $\sim$10 mK)

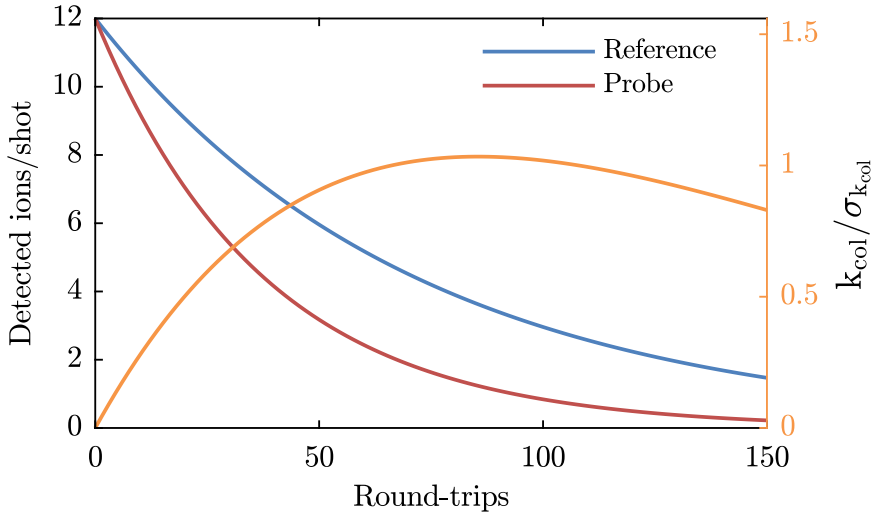

Figure 3.2 – Model of the probe (red) and reference (blue) signals (using numbers from the experiment that will be discussed in Sec. 3.5), and the signal-to-noise ratio (orange, right y-axis) that results when these signals are used to calculate the loss rate due to collisions k_{col} of the probe packets.

and widely (100–150 m/s) tunable velocities, they are well suited for collision studies as will be demonstrated in this chapter.

The main idea of our experiment is illustrated in Fig. 3.1. A beamline is added tangentially to the synchrotron, so that certain packets of ammonia molecules encounter a fresh packet of collision partners every round-trip. This beamline is co-propagating with respect to the ammonia molecules, so that the crossing angle is zero and low collision energies can be achieved [20, 21, 24, 28, 66]. The experiment is triggered in such a way that some of the ammonia packets—the *probe* packets—encounter fresh packets of collision partners every round-trip, while other packets—the *reference* packets—do not. When after a certain number of round-trips the packets are detected, the probe and reference signals are compared to find the rate at which ammonia molecules are lost from the synchrotron due to collisions. The longer the packets are stored before detection, the more molecules are lost from the probe beam. In this way, collision signal is accumulated and the sensitivity to measure collisions is strongly enhanced.

The expected enhancement in sensitivity is illustrated in Fig. 3.2. The signals of the probe (red, S_{probe}) and reference packets (blue, S_{ref}), using numbers from the experiment that will be discussed in Sec. 3.5, are shown as a function of storage time in the synchrotron. Both signals are modeled by exponential decays. While the probe and reference packets share the same background loss rate (in this calculation $k_{\mathrm{bg}} = 1.46\%$ per round-trip), the probe packets are modeled to experience additional loss due to collisions with

particles from the collision partner beamline (at a rate of $k_{\mathrm{col}} = 1.26\%$ per round-trip). After a given number of round-trips RT, the loss rate due to collisions can be found using

$$k_{\mathrm{col}} = \frac{1}{\mathrm{RT}} \ln(\frac{S_{\mathrm{ref}}}{S_{\mathrm{probe}}}). \tag{3.1}$$

The uncertainty in the loss rate is found from the statistical uncertainties in the probe and reference signals. Since the number of detected ions follows Poison statistics, the uncertainty is given by the square-root of this number:

$$\sigma_{\mathrm{k_{col}}} = \frac{1}{\mathrm{RT}} \sqrt{(\frac{1}{S_{\mathrm{ref}}}) + (\frac{1}{S_{\mathrm{probe}}})}. \tag{3.2}$$

The orange curve shows the ratio of the calculated loss rate k_{col} and its uncertainty $\sigma_{k_{\mathrm{col}}}$, after a single measurement only (i.e., a single measurement of a probe and a reference packet, requiring two shots). This signal-to-noise ratio increases dramatically the first tens of round-trips, due to the factor of $\frac{1}{\mathrm{RT}}$ in $\sigma_{k_{\mathrm{col}}}$. After about 90 round-trips, roughly 2 times the lifetime of the probe packet, the statistical uncertainty in S_{probe} becomes the limiting factor and the signal-to-noise ratio decreases again. For the numbers used in this calculation, the expected signal-to-noise ratio at the optimal number of round-trips is $\sim$1 after a single measurement of the probe packet and reference packet. The uncertainty can thus be reduced to below 1% by measuring 20,000 shots, or a little over half an hour when measuring at a rate of 10 Hz. Note that the signal-to-noise ratio at the optimal number of round-trips is 34 times larger than after a single round-trip. Consequently, the sensitivity of the synchrotron reduces the measuring time by over a factor of 1,000 with respect to a hypothetical crossed beam experiment with the same densities. This enhancement in sensitivity is what motivated us to do this experiment.

When we started this project, we set out to measure collisions between hydrogen and ammonia molecules at low energies, as hydrogen is the most abundant molecule in the universe while ammonia is the most abundant polyatomic molecule. Furthermore, due to the small mass of hydrogen, the ND_3 + H_2 collision cross section displays interesting resonances [73]. As a first step, we measured collisions between ammonia and hydrogen molecules at high energies. These measurements are presented in Figures 3.13 and 3.14. To reach low energies, we planned to seed hydrogen molecules in argon. Since the argon atoms of course also collide with the ammonia molecules, it was necessary to first measure the ND_3 + Ar collision cross section, which is the main topic of this chapter. Collisions between ammonia (NH_3 and ND_3) and noble gases at high energy have been extensively studied by different groups [74–82].

The rest of this chapter is organized as follows: Sections 3.3 and 3.4 provide a detailed overview and characterization of the experimental setup. We present measurements of the argon beams at two positions along the beamline to determine the position and velocity distributions at any position and time.

Section 3.5.1 present measurements of the loss rate of stored ammonia molecules in the ring due to collisions with hydrogen and argon beams at a fixed energy. To be able to retrieve collision cross sections from the measurements, a detailed analysis is required that combines trajectory simulations of ammonia molecules in the synchrotron with a model of the collision partner beamline. This critical piece of the puzzle, which importantly also provides the collision energy distributions probed in the experiments, is described in detail in Section 3.5.2. Everything comes together in Section 3.5.3, where measurements are presented of the ND_3 + Ar cross section as a function of collision energy. Finally, in Section 3.6 conclusions are drawn and possible future experiments are discussed.

3.3 Molecular synchrotron

Our molecular synchrotron, schematically depicted in Fig. 3.3, consists of 40 electric hexapole elements arranged in a half-meter-diameter circle. Voltages of up to $\pm 5\,\mathrm{kV}$ are applied to the electrodes in order to transversely trap ammonia molecules in the low-field seeking sublevel of the $J = 1$, $K = 1$ rovibrational ground state within the hexapoles. The molecules are bunched longitudinally by switching the voltages temporarily to higher voltages as the molecules fly through the gap between one hexapole and the next. In our experiments, up to 14 of these packets are stored simultaneously, with velocities of 100–150 m/s.

New packets are injected into the synchrotron by an injection beamline consisting of a Gentry type pulsed valve (R.M. Jordan company), which releases packets of 5% ammonia seeded into xenon with velocities around 350 m/s, a Stark decelerator, which decelerates ammonia molecules in the $J = 1$, $K = 1$ rovibrational ground state to velocities down to 100 m/s, a buncher which focuses the molecules longitudinally into the synchrotron, and hexapole elements which focus the molecules transversely. To allow the molecules to enter the synchrotron, 4 hexapole elements of the synchrotron are temporarily switched off. The beamline is synchronized with the cyclotron frequency of the stored molecules in such a way that new packets are injected two hexapole segments in front of the packets that are already stored, at a rate around 10 Hz. For molecules that are stored at a velocity of 121.1 m/s, this implies that they make 6+38/40 round-trips before a new packet is injected, while molecules stored at a velocity of 138.8 m/s make 7+38/40 round-trips before a new packet is injected.

The velocity of the injected ammonia molecules is determined by the trigger sequence applied to the Stark decelerator, and can be changed almost instantaneously; it takes 1.4 s to load the synchrotron with new packets after changing the cyclotron frequency and the trigger sequence. In this way, the collision energy can be varied on relatively short timescales to counteract possible drifts of the intensity and timing of the argon beam during collision measurements.

At the same rate that new packets are injected, the oldest packet in the

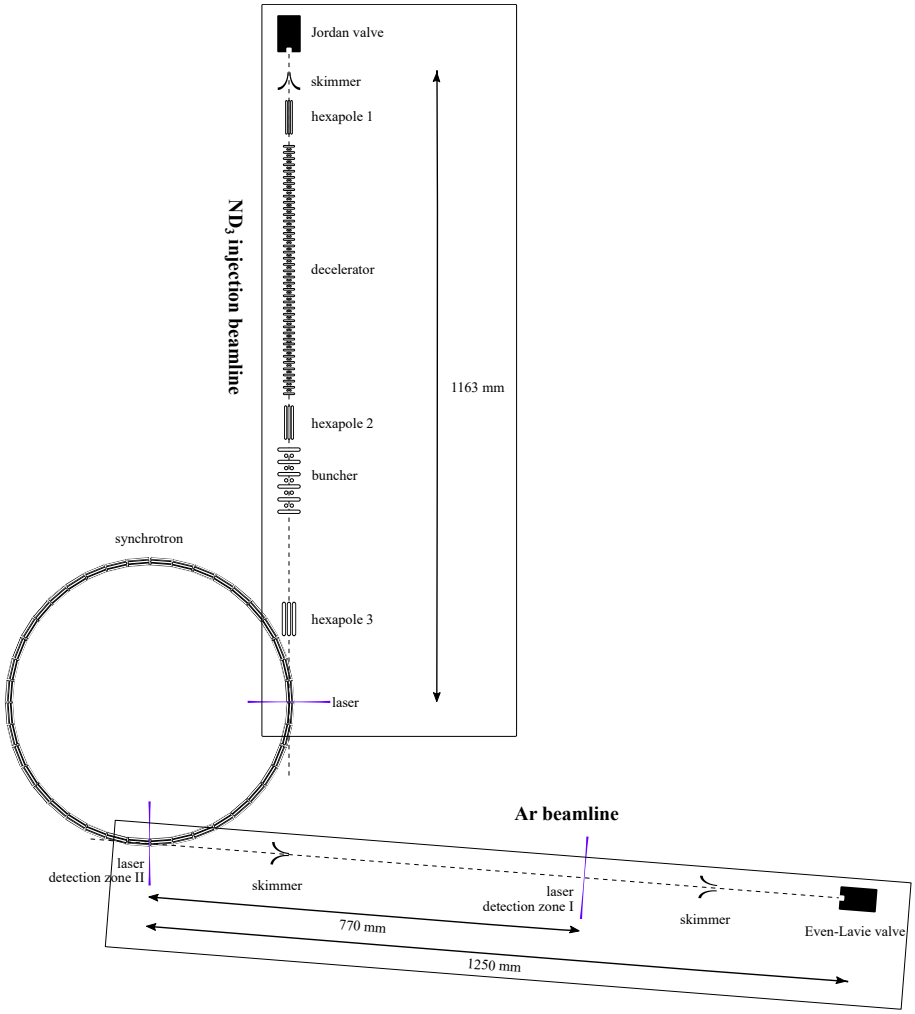

Figure 3.3 – Top view of the experimental set-up (to scale). ND_3 molecules are decelerated to velocities of 100–150 m/s using a Stark decelerator and injected into a molecular synchrotron consisting of 40 electric hexapole elements arranged in a half-meter-diameter circle. Ammonia molecules can be detected at the injection point or at a quarter ring downstream (detection zone II). The argon beamline consists of a cooled solenoid valve that is skimmed by a 5 mm and a 1.5 mm skimmer. Argon atoms are detected 770 mm in front of the synchrotron (detection zone I) or inside the synchrotron (detection zone II). The argon beamline makes an angle of 94,5 degrees with respect to the injection beamline such that the argon beam moves parallel to the first hexapole in the synchrotron behind detection zone II.

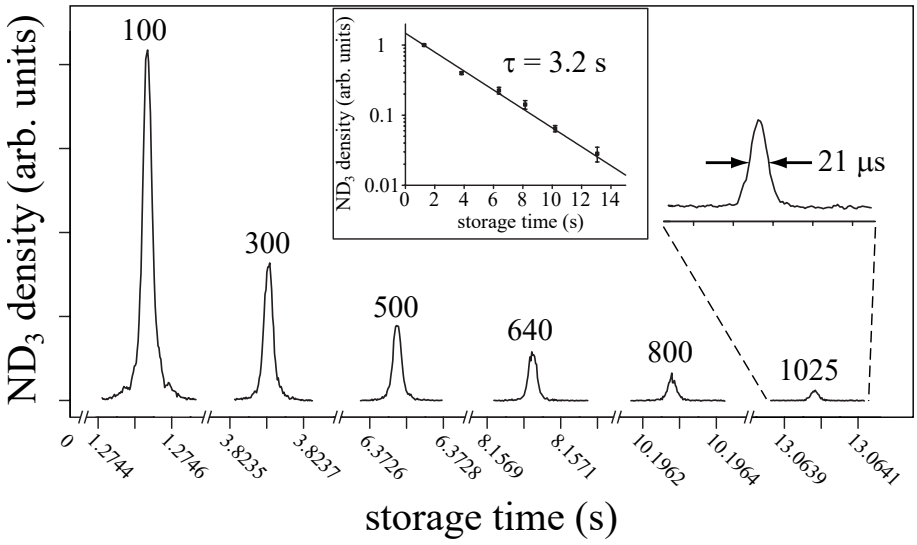

Figure 3.4 – Time-of-flight measurements of ammonia molecules traversing the synchrotron. The numbers above the peaks denote the number of round-trips the molecules have completed at the time of measurement. The inset shows that the 1/e trapping time is 3.2 s. Reprinted with permission from Ref. [56] ©2010 APS.

synchrotron is detected at one of two detection zones: A focused laser pulse (typically 5 ns long, 10 mJ/pulse, 317 nm) ionizes ammonia molecules by 2+1 Resonance-Enhanced Multi-Photon Ionization (REMPI) *via* the electronic B-state. The UV-beams are focused in-between the hexapole elements using lenses with focal lengths of 50 mm, which are mounted on three-dimensional translation stages to allow precise scanning of the position of the laser focus. The two adjacent hexapole elements are switched to a voltage configuration that accelerates the ions upwards to a drift tube, for time-of-flight mass-spectrometry. The ions are detected on a Multi-Channel-Plate (MCP) detector. The two detection zones in the synchrotron are marked by a laser beam in Fig. 3.3. During the collision measurements, the ammonia molecules are detected in detection zone II.

Fig. 3.4 shows the ammonia signal measured in the synchrotron as a function of time. It demonstrates that a packet of ammonia molecules is still clearly visible even after completing more than 1,000 round-trips, corresponding to a trapping time of over 13 seconds. In this time the molecules have traversed a distance of over a mile [56, 57, 68].

When the system is kept under vacuum for many weeks, the pressure reaches 5×10^{-9} mbar. Under these conditions the 1/e-lifetime of the stored packets is 3.2 s, determined equally by collisions with the background gas and black-body-radiation-induced transitions to non-trappable states [56]. In the experiments

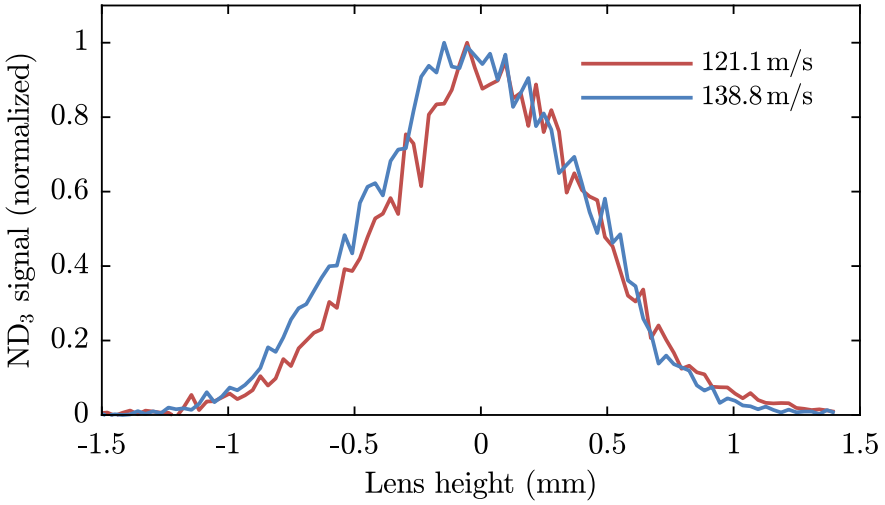

Figure 3.5 – Laser height scans of ammonia packets at two velocities at detection zone II.

described in Section 3.5 the pressure is typically 2×10^{-8} mbar, resulting in a lifetime of 1.0 s.

Fig. 3.5 shows laser height scans of ammonia packets with velocities of 121.1 and 138.8 m/s, both after 90 round-trips. From these measurements in combination with trajectory simulations it is found that the emittance of the stored ammonia under our conditions is $[1\,\text{mm}\cdot5\,\text{m/s}]^2\cdot[4\,\text{mm}\cdot1\,\text{m/s}]$. More details on the synchrotron and injection beamline can be found in Zieger *et al.* [56, 57, 68].

3.4 Collision partner beamline

3.4.1 Longitudinal distribution

A schematic overview of the argon beamline is shown in Fig. 3.3. A supersonic argon beam is formed by releasing a high pressure (∼4 bar) gas into vacuum by a pulsed solenoid valve (Even Lavie type E.L.-5-2005 RT, HRR [69]) running at two times the cyclotron frequency of the synchrotron (153–175 Hz). To help keep the pressure in the source chamber below 1×10^{-4} mbar, an additional turbomolecular pump provides a pre-vacuum of $<5\times10^{-4}$ mbar to the turbo pumps of the source and detection chambers. The 5 mm diameter skimmer between the source and detection chambers and the 1.5 mm diameter skimmer between the detection and the synchrotron chambers allow for differential pumping, and select only the coldest part of the argon beam in order to keep the pressure in the synchrotron chamber below 2.2×10^{-8} mbar during operation.

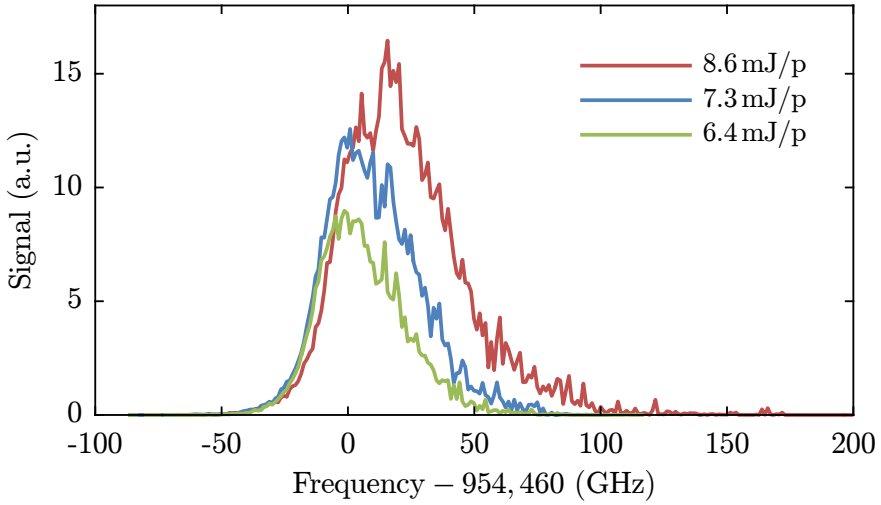

Figure 3.6 – 3+1 REMPI spectra at frequencies around the $3s^2 3p^6(^1S)$ to $3s^2 3p^5(^2P_{1/2})4s$-transition in argon.

In order to tune the velocity of the beam, the temperature of the valve housing can be varied between −150°C and +30°C. The temperature of the valve is regulated as follows: A flow of nitrogen gas is cooled down by passing it through a spiral tube immersed in liquid nitrogen, then passes a heater, and finally flows through a heatsink mounted onto the valve. The current flow through the heater is controlled by a Eurotherm 2408 PID-controller, which uses a thermocouple attached to the heatsink to read out its temperature. The time it takes for the valve temperature to reach its target temperature and stabilize can be between 45 minutes for a set temperature of 30°C and 2 hours for −150°C. To avoid losing time, we typically operate the valve at a constant temperature throughout the day.

The argon atoms can be detected at two locations: in detection zone I, approximately half-way the argon beamline, and in detection zone II, inside the synchrotron, where also the ammonia molecules are detected. UV laser pulses (5 ns long pulses with typically an energy of 10 mJ/pulse at λ =314 nm) are focused into the detection zones to ionize the argon atoms by 3 + 1 REMPI *via* the $3s^2 3p^5(^2P_{1/2})4s$-state [70]. In detection zone I, the resulting ions are extracted upwards by a stack of electrostatic ion lenses and mass-selectively detected on an MCP detector. Inside the synchrotron (detection zone II) the ions are extracted by switching the two adjacent hexapole elements to the appropriate voltages, as discussed in Section 3.3. Fig. 3.6 shows spectra measured at three different laser powers illustrating that the transition is significantly broadened and shifted by the field of the laser. The hydrogen

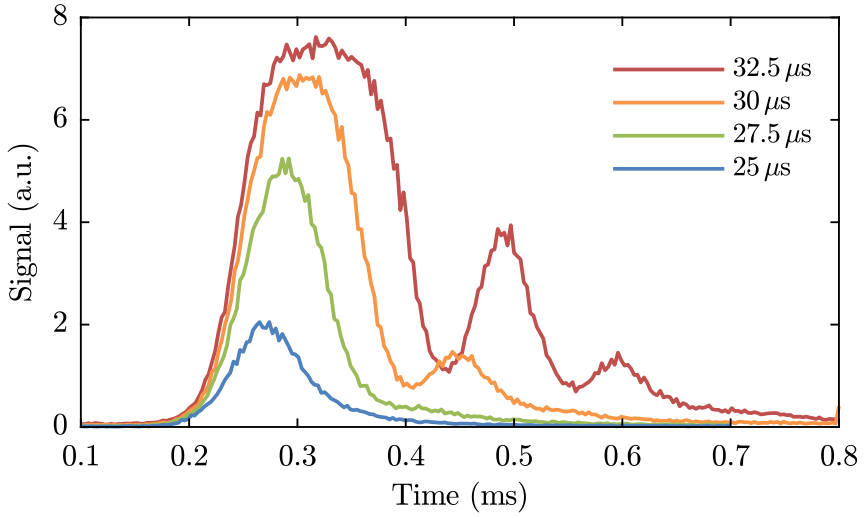

Figure 3.7 – Time-of-flight measurements of hydrogen beams. The durations of the current pulses that open the solenoid valve are indicated in the upper right corner. In these measurements the valve was kept at room-temperature and a backing pressure of 3 bar was used.

molecules are detected using 3+1 REMPI *via* the electronic C-state at 290 nm [83].

Fig. 3.7 shows typical time-of-flight (TOF) measurements of hydrogen molecules. In these measurements, the current pulse that is applied to the valve is set to different values as indicated in the figure. The exit aperture of our valve is shut by a plunger, which is pushed into the seal by the combined force of a spring and the pressure of the gas behind it. To open the valve, the plunger is pulled backwards by sending a short current pulse through a solenoid. The length of this pulse determines how much energy is imparted on the plunger, and thus how far it is pulled back before it returns to its normal position. As shown in Fig. 3.7, when a current pulse of 25 μs is applied, the resulting TOF distribution resembles an asymmetric Gaussian profile. When the duration of the current pulse is increased, the beam becomes more intense, however the shape of the TOF-profile changes markedly. When the duration of the current pulse is increased further, the observed profile exhibits additional peaks which are attributed to the plunger bouncing once or several times, releasing multiple pulses of gas. This is highly unwanted during collision experiments, as it complicates the interpretation of our measurements. For this reason, the duration of the current pulses are limited to prevent bouncing. Note that the onset of bouncing depends on the backing pressure and the temperature of the valve. The bouncing is most prominent at high temperatures, whereas at low temperatures the duration of the current pulse is limited by the pumping capacity.

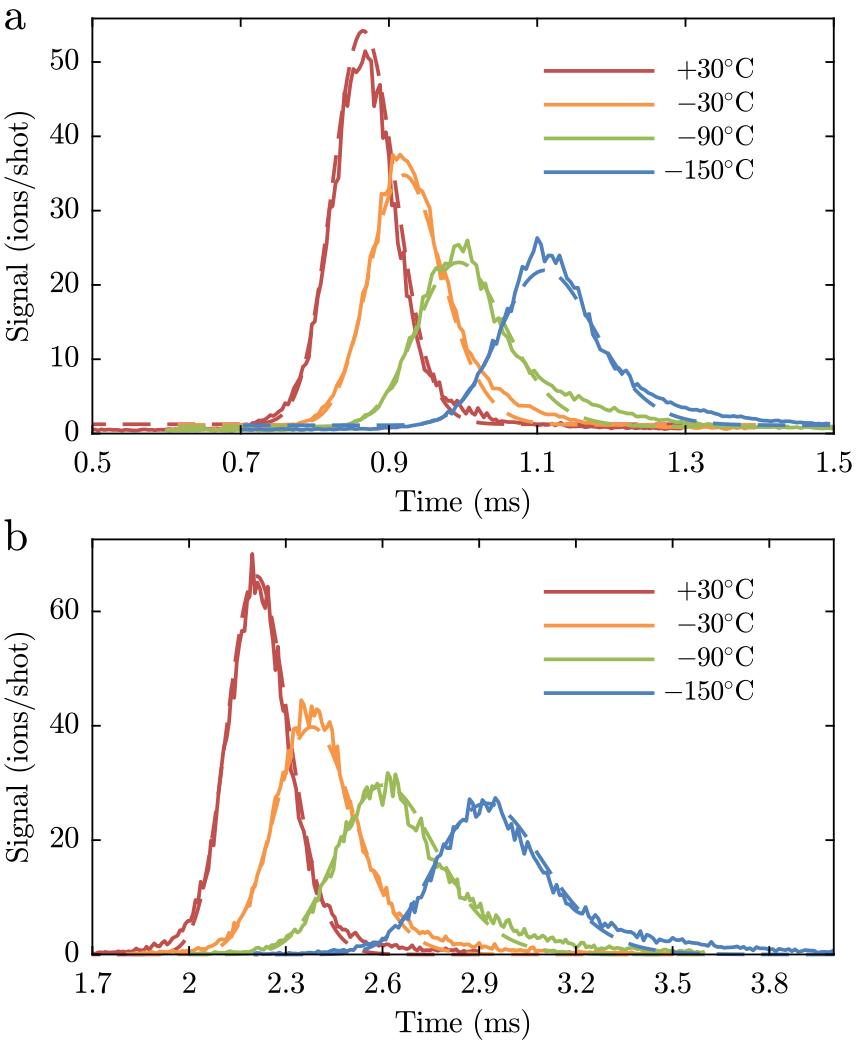

Figure 3.8 – Argon time-of-flights as measured in detection zones I (a) and II (b), with different temperatures of the pulsed valve. For each temperature, a model for the argon beam is fitted simultaneously through the two time-of-flight measurements. The resulting fit parameters are listed in Table 3.1.

In our experiment, described in the next sections, we collide stored ND_3 molecules with argon beams. In order to measure the cross sections as a function of collision energy, we operate the valve that releases the argon beam at four different temperatures (-150, -90, -30 and 30°C) and use two ammonia velocities (121.1 and 138.8 m/s), which imply that the valve will operate at two repetition frequencies (153 and 175 Hz). To characterize the beams under

these conditions, we have recorded many TOF profiles at both detection zones (I and II). Typical measurements taken with the valve running at 153 Hz are shown in Fig. 3.8. Note that the MCP used in the first detection zone is rather old and its quantum efficiency has degraded over time. Whereas the density of the beam at the first detector is at least a factor of 10 higher than the density at the second detector, the number of ions detected per shot at both detectors is similar.

The longitudinal properties of the argon beam are modeled as follows. In general, the spatial density distribution $n_{\mathrm{Ar}}(z|v,t)$ of argon atoms with a velocity between v and $v + \mathrm{d}v$ at a time t can be described by

$$n_{\mathrm{Ar}}(z|v,t) = N\, f^v(v)\, \mathrm{d}v\, f^z(z|v,t),$$

where N is the number of atoms in the packet, $f^v(v)$ is the time-independent, normalized, velocity distribution, and $f^z(z|v,t)$ is the normalized position distribution of argon atoms with a velocity between v and $v + \mathrm{d}v$ at time t. We assume the velocity distribution $f^v(v)$ to be given by the normal distribution $g^v(v|\langle v\rangle, \sigma_{\mathrm{v}})$ with average $\langle v\rangle$ and standard deviation σ_{v}. The position distribution $f^z(z|v,t)$ at a certain time t can be extrapolated from the position distribution at the source $f^z(z|v,t=0)$. This initial distribution is assumed to be a normal distribution with $\langle z\rangle = z_{\mathrm{valve}}$. From the opening time of the valve and the velocity of the atoms in question, the standard deviation is given by v times pw. Here pw stands for pulse width, i.e. the time that the valve is open. In time, the center of the initial position distribution moves with velocity v while the shape remains constant, as all the atoms have the same velocity v. Thus, the position distribution at a certain time t is given by the normal distribution $g^z(z|z_{\mathrm{valve}} + vt, v\ pw)$. Finally, the measured signal $S(z,t)$ at position z and at time t is proportional to the argon density, which is found by integrating $n_{\mathrm{Ar}}(z|v,t)$ over all velocities:

$$S(z,t) \propto \int_{-\infty}^{+\infty} g^v(v|\langle v\rangle, \sigma_{\mathrm{v}})\, g^z(z|z_{\mathrm{valve}} + vt, v\ pw)\, \mathrm{d}v. \tag{3.3}$$

Equation 3.3 is simultaneously fitted to the TOF profiles measured at detection zone I and detection zone II. The fit parameters, $\langle v\rangle$, σ_{v}, pw, and z_{valve}, are determined by minimizing the weighted sum of the squares of the residuals, and are presented in Table 3.1.

Since our ultimate goal is to measure collision cross sections, the argon beam intensities are very important to measure accurately. Therefore, time-of-flight measurements were made at detection zone II (close to where the collisions will happen), at each of the four valve temperatures and two repetition rates, in a single day. Care was taken to keep the laser power within $8.00 \pm 0.05\,\mathrm{mJ/p}$. The measurements are shown in Fig. 3.9. They are fitted with the arrival time distribution for a beam with a normal velocity distribution originating from a

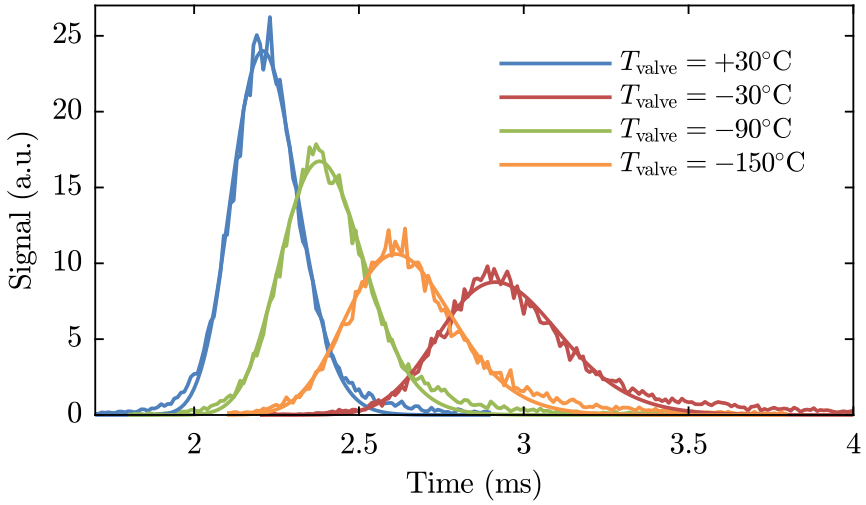

Figure 3.9 – Argon time-of-flight measurements (with fits) in detection zone II at the different valve temperatures, for the purpose of argon beam intensity calibration. Measured in a single day; care was taken to keep the laser power within $8.00 \pm 0.05\,\text{mJ/p}$.

point source, given by

$$S(t) = S_0 \exp\left\{ -\left(\frac{1}{t} - \frac{1}{\langle\tau\rangle}\right)^2 \Big/ \left(2\frac{\Delta\tau^2}{\langle\tau\rangle^4}\right)\right\}, \tag{3.4}$$

where S_0 is the peak signal, $\langle\tau\rangle$ the mean arrival time, and $\Delta\tau$ a measure of the width of the distribution similar to a standard deviation. The distribution resembles a normal distribution that is unevenly stretched along the time axis: the slower part of the beam needs a longer time to arrive at the detection zone, and therefore has more time to disperse. The relative beam intensities are given by the fit maxima (S_0), normalized to the argon beam at $T_{\text{valve}} = -150°\text{C}$. The resulting calibrations are also presented in Table 3.1.

T_{valve} (°C)	f_{rep} (Hz)	v_{ND_3} (m/s)	Δt_{pulse} (μs)	rel. int.	$\langle\tau\rangle$ (ms)	$\Delta\tau$ (μs)	L (mm)	$\langle v_{Ar}\rangle$ (m/s)	$\sigma_{v_{Ar}}$ (m/s)	pw (μs)	Δz (m)
+30	153	121.1	27.3	3.00 ± 0.20	2.207	96	137	570.56	24.01	22.41	1.265
	175	138.8		2.74 ± 0.18	2.205	94	134	571.41	24.09	22.48	1.265
−30	153	121.1	25.2	2.02 ± 0.12	2.380	124	163	524.08	27.57	11.24	1.255
	175	138.8		1.91 ± 0.11	2.378	122	160	524.73	27.30	13.73	1.254
−90	153	121.1	23.6	1.31 ± 0.11	2.604	162	192	474.51	28.48	10.00	1.245
	175	138.8		1.21 ± 0.10	2.597	159	189	475.40	29.22	10.00	1.245
−150	153	121.1	22.8	1.11 ± 0.10	2.921	173	183	421.92	24.32	10.00	1.241
	175	138.8		1.00 ± 0.09	2.916	175	185	423.40	24.98	10.00	1.242

Table 3.1 – Overview of the properties of the argon beam at different temperatures of the valve housing T_{valve}, repetition rates f_{rep} (which are determined by the velocity of the stored ammonia molecules), ammonia velocities v_{ND_3}, and durations of the current pulse applied to the valve Δt_{pulse}. The second block lists properties of the beams measured at detection zone II: the relative beam intensity, mean arrival time, $\langle\tau\rangle$, the width of the arrival time distribution $\Delta\tau$, and the full width at half maximum (FWHM) length of the argon packet $L = \langle v_{Ar}\rangle \times 2\sqrt{2\ln 2}\,\Delta\tau$. Finally, the last block lists the parameters found from a simultaneous fit to the time-of-flight distributions measured at both detectors: the mean $\langle v_{Ar}\rangle$ and standard deviation $\sigma_{v_{Ar}}$ of the velocity distribution, duration of valve opening time, and the effective distance between the valve and detection zone II.

3.4.2 Transverse distribution

The geometry of the beamline, i.e., the skimmers and the gap between the hexapole rods through which the argon beam enters the synchrotron, determines partially, but not completely the transverse spatial and velocity distributions of the argon. Following the recommendations given in Ref. [69], we have installed a skimmer with a large aperture (Beams dynamics, type II, 5 mm) at a distance of 200 mm in front of the valve. The effective size of the source, i.e., the transverse size of the argon beam when the density has dropped to such extent that collisions cease to be important (the freezing point), is smaller than the aperture of the first skimmer. Hence, this effective size, together with the second skimmer and the gap between the electrodes, determines the transverse spatial and velocity distribution of the argon beam in the synchrotron.

To determine the effective size of the source, we have performed two types of measurements: (i) we have recorded the argon signal in the synchrotron while scanning the horizontal and vertical positions of the valve, and (ii) we have scanned the height of the laser focus for two positions of the valve. The results of both measurements are shown in Fig. 3.10. The blue squares in Fig. 3.10(a) show the signal when the valve is displaced in the horizontal direction, while the red triangles show the signal when the valve is displaced in the vertical direction. Note that, since the skimmer is located at $\sim$80% along the path between the valve and the detection zone, a displacement of 4 mm of the valve results in a beam displacement of $\sim$1 mm in the detection zone. At two vertical positions of the valve, the vertical distribution is measured by scanning the laser focus as shown in Fig. 3.10(b). The orange curve is measured while the valve is close to the center position (indicated by the arrow "A" in Fig. 3.10(a)), while the purple curve is measured when the valve is 4 mm down from the center (indicated by the arrow "B" in Fig. 3.10(a)).

These measurements are compared with simulations that calculate the trajectories of argon atoms through the machine. The simulation starts by initializing argon atoms with random positions and velocities, given by Gaussian distributions. The atoms then fly in a straight line from the valve to the detection zone. They are counted if they fly through both skimmers and arrive at the laser focus. The results of simulations performed with effective source sizes of 1.5, 3, 4.5, and 6 mm are depicted by the gray lines in Fig. 3.10. The widths of the velocity distributions are unimportant, as the divergence of the beam at the source is much large than what is accepted by the skimmers, and are set to be $>$10 m/s. From the measurements, we conclude that the effective size of the source is $\sim$4.5 mm.

Fig. 3.11 shows a simulation of the transverse distribution of the argon beam at the longitudinal position where the atoms (first) collide with the stored ammonia molecules. This simulation uses the parameters found from the experiment. In order to simplify the analysis of our collision experiment, we will approximate the beam by a cylinder with a diameter of 1.66 mm, indicated by the red circle in Fig. 3.11; the density of the gas within this cylinder is assumed

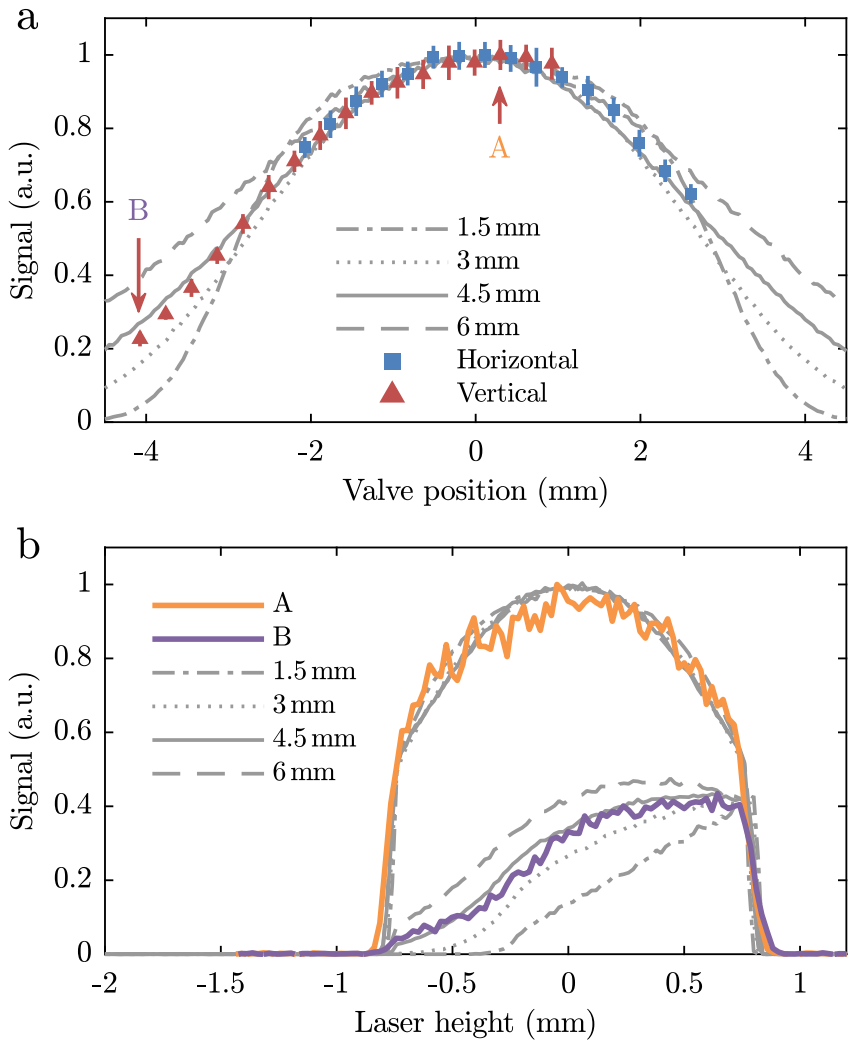

Figure 3.10 – (a) Argon signal in detection zone II as function of the horizontal (blue squares) or vertical (red triangles) position of the valve. Error bars represent standard errors of the means. (b) Scan of the vertical position of the laser focus when the valve is positioned close to the center (corresponding to arrow "A" in panel a) or 4 mm below the center (corresponding to arrow "B" in panel a). The grey lines in (a) and (b) show simulations with different values of the effective size of the beam source.

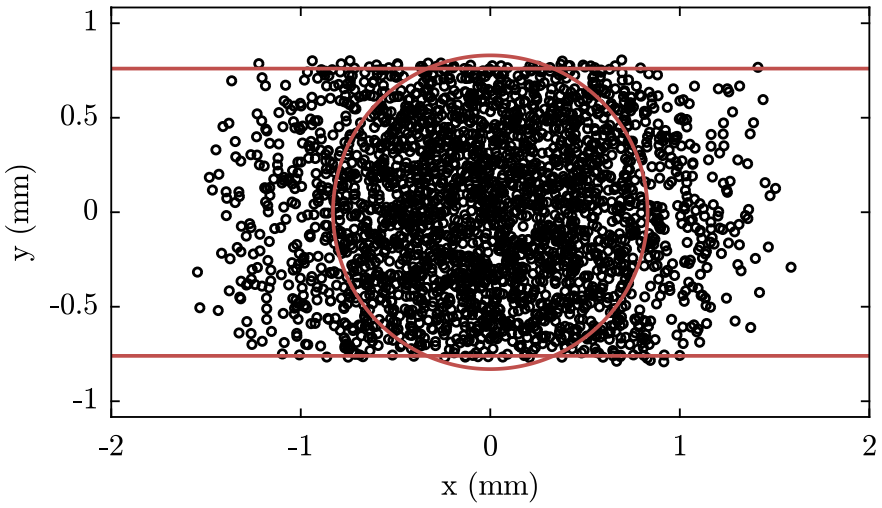

Figure 3.11 – Transverse position distribution of simulated argon atoms at the longitudinal position where the atoms first collide with the stored ammonia molecules. The horizontal lines reflect the cut-off of the electrodes that make up the hexapole element through which the argon beam first enters the synchrotron. The circle approximates the circular cut-off due to the second skimmer. The resulting flattened circle shows the transverse shape of the argon beam that is used in trajectory simulations of ammonia molecules.

to be independent of the radial direction and is taken to be equal to the peak density. In this way, the number of atoms in the model equals the number of atoms in the experiment. To account for the effect of the gap, the distribution is limited to 1.52 mm in the vertical direction. The size of the beam increases by 5% over the course of 40 mm. The intensity decreases concomitantly so that the number of molecules remains constant.

In our collision experiments presented in Section 3.5.3, we aligned the argon beam 1.6 mm inwards with respect to the equilibrium orbit of the stored ammonia molecules, such that it intersects their path twice: once close to the detection zone in the synchrotron, and once 58 mm downstream. Although this ends up degrading the energy resolution, it simplifies the analysis of our measurements by allowing the measurement of the alignment. More discussion on this in Section 3.5.3.

3.5 Measuring collisions

3.5.1 Collisions at a specific collision energy

We now arrive at the heart of this chapter: the collision measurements. As explained in Section 3.3, we store multiple packets of ammonia molecules

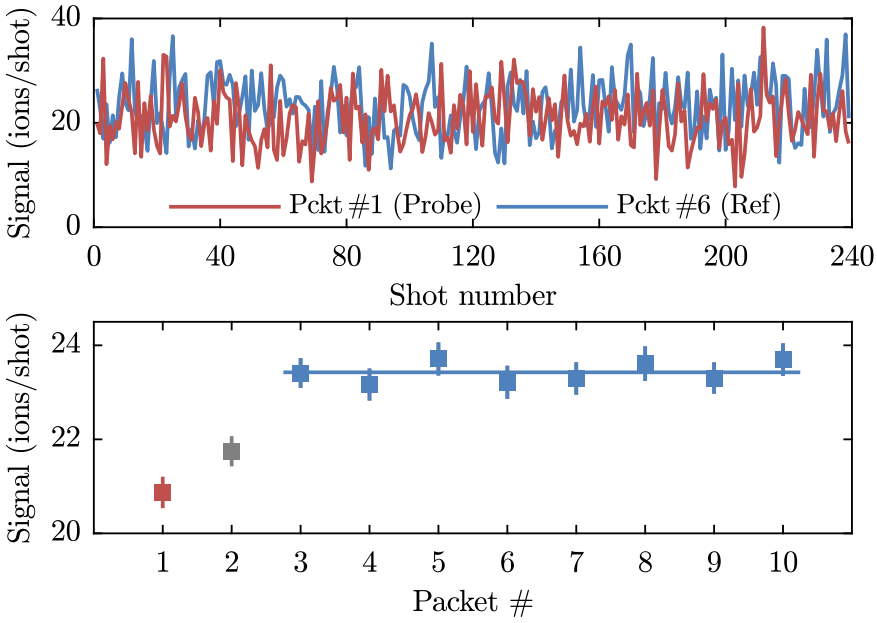

Figure 3.12 – (a) Single-shot measurements of ammonia packets after 90 round-trips. The red trace corresponds to the probe packet, the blue trace to one of the reference packets. (b) 240-shot averages of the probe packet (red), a discarded reference packet (grey), and 8 reference packets (blue). The error bars denote standard errors of the means. The blue line depicts the average of the 8 reference packets.

in a synchrotron while sending in beams of atoms and molecules that are made to collide with some of the packets–the probe packets. Packets that do not encounter the co-propagating beam–the reference packets–provide a simultaneous measurement of background loss. In the experiments discussed here, 14 packets of ammonia molecules are stored simultaneously, each packet stored two hexapole segments in front of the previous one. The valve that releases the collision partner (either argon or hydrogen) runs at twice the cyclotron frequency such that every tenth ammonia packet encounters a fresh partner beam every round trip.

Fig. 3.12 shows a typical measurement of an experiment where ammonia molecules, revolving in the synchrotron with a mean velocity of 121.1 m/s, are detected after 90 (and a quarter) round-trips. These molecules are made to collide with beams of argon atoms with mean velocities of 474.5 m/s. Typically, we take data in blocks of 4 minutes corresponding to 2400 individual measurements, taken at a rate of 10 Hz. Subsequently, measurements that are taken at the same delay with respect to the partner beam are grouped together, resulting in ten sets of 240 measurements each. The measurements in each set are averaged and further analysed. The top panel of Fig. 3.12 shows two traces

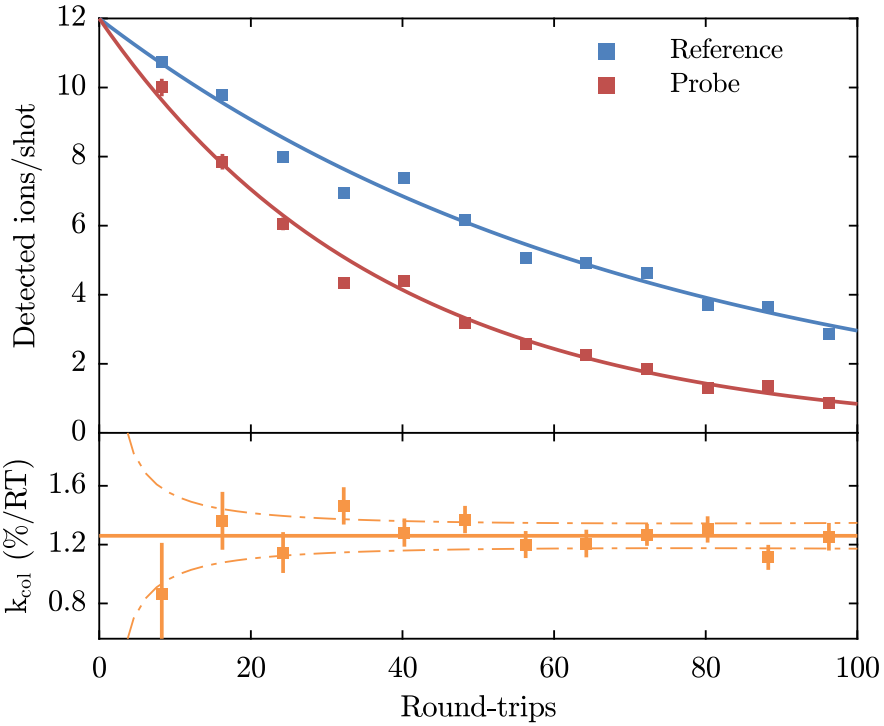

Figure 3.13 – Results of an experiment in which the ammonia probe packets are collided with beams of hydrogen molecules. Top panel: Measurement of the probe (red squares) and reference packets (blue squares). Bottom panel: From each set of measurements at each number of round-trips, the loss rate due to collisions with hydrogen molecules is calculated using Equation 3.1 and presented by the orange squares. The error in the loss rate is seen to decrease with the number of round-trip, as expected from the calculations shown by the orange dashed lines.

corresponding to the probe packet (red) and one of the reference packets (blue). The noise on the measured traces has a standard deviation of 5.3 ions per shot which is only slightly larger than the $\sqrt{23.4} = 4.8$ ions per shot expected for a Poissonian distribution. The difference is attributed to noise added by the MCP detector. The lower panel of Fig. 3.12 shows the averages for each of the 10 sets, along with the standard errors of their means (SE $= \sigma/\sqrt{n}$). The signal of the probe packet (#1) is about 11% smaller than the average of packets #3–10, corresponding to a loss rate of $k_{col} = (1.28 \pm 0.18)\times10^{-3}$ per round-trip. As observed, the argon beam also has some overlap with packet #2 in this particular experiment; this packet is therefore discarded. Depending on the timing of the partner beam, in other experiments also packets #3, #9, and/or #10 are discarded.

Fig. 3.13 shows the results of measurements in which ammonia molecules

are detected after several numbers of round-trips, while being bombarded with intense beams of hydrogen molecules. Note that the error bars, which reflect the statistical spread of the ion signal in the form of the standard error, are (in most cases) smaller than the symbols. The upper panel depicts the reference (blue) and probe (red) signals. Both data sets have been fit with exponential decays given by

$$S = S_0\, e^{-k\cdot \mathrm{RT}}, \tag{3.5}$$

with S_0 the signal after 0 round-trips, k the (total) loss rate, and RT the number of round-trips the ammonia molecules are stored before detection. A loss rate of $\mathrm{k_{ref}} = (1.41 \pm 0.08)\%$ per round-trip is found for the reference packets, which is consistent with the loss rate expected from collisions with back-ground gas in the synchrotron at a pressure of 2×10^{-8} mbar. For the probe packets, a loss rate of $\mathrm{k_{probe}} = (2.67 \pm 0.11)\%$ per round-trip is found, which implies a loss rate due to collisions with hydrogen molecules of $\mathrm{k_{col}} = (1.26 \pm 0.14)\%$ per round-trip.

The data points in the lower panel of Fig. 3.13 show the loss rates due to collisions with hydrogen molecules calculated at every number of round-trips, using Equation 3.1. The standard error, derived from the statistical uncertainty of the ion signals using Equation 3.2, decreases dramatically during the first tens of round-trips, demonstrating that the ability to store molecules in a synchrotron does indeed lead to increased sensitivities. The error follows nicely the orange dash-dotted lines, which depict the statistical uncertainty one would expect based on the number of detected ions per shot. Furthermore, while the probe and reference signals show deviations from the exponential curves, caused by changing systematics in the experiment, these fluctuations are common to the probe and reference signals and are as such absent from the determined loss rates.

As discussed in Section 3.2, the optimal number of round-trips depends on both the background loss rate as well as the loss rate due to collisions with particles in the partner beam. While in the case presented in Fig. 3.13 the error in determining the loss rate is optimal after 85 round-trips, it would be advantageous to store the molecules longer if the loss rates would be smaller. In the current configuration of the synchrotron, however, ammonia molecules with velocities of $v_{\mathrm{ND_3}} = 121.1\,\mathrm{m/s}$ or $v_{\mathrm{ND_3}} = 138.8\,\mathrm{m/s}$ cannot be stored longer than 94 (and a quarter) or 103 (and a quarter) round-trips, respectively, without decreasing the rate at which packets are injected and detected below 10 Hz. A lower detection rate would in turn imply that the ion count rate goes down, resulting in a lower signal-to-noise ratio. Lowering the detection rate is thus only useful if the sensitivity increases enough to justify the loss in signal (i.e. faster than the square root of the number of detected ions).

As can be seen from Equations 3.2 and 3.5, the error in the loss rate depends on the background loss rate k_{bg}. If we would decrease the pressure in the synchrotron chamber by a factor of four (e.g. from 2×10^{-8} mbar to 5×10^{-9} mbar), this would decrease the loss rate due to collisions with the

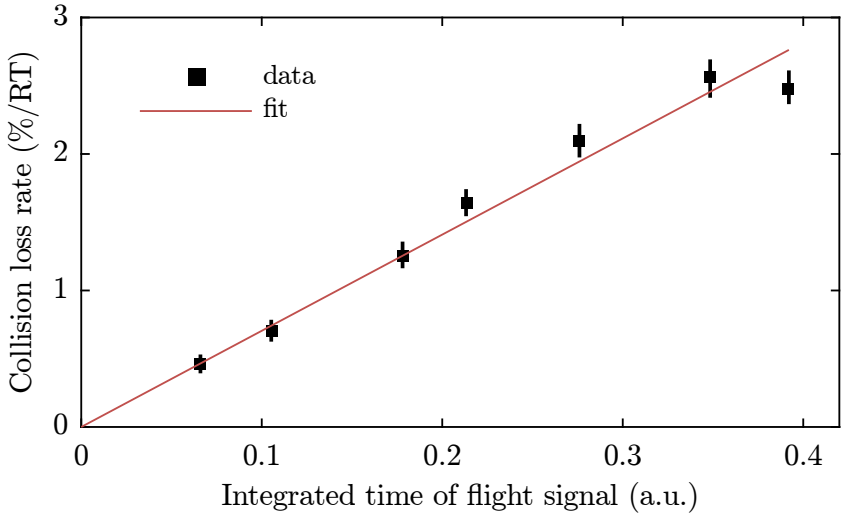

Figure 3.14 – For several backing pressures, a collision experiment is performed to find the loss rate due to collisions with hydrogen molecules, and a time-of-flight measurement is performed in detection zone II to measure the amount of molecules in the beam. The resulting loss rates are plotted here as a function of the integrated time-of-flight measurements. The error bars denote standard errors.

background gas by a factor of four. The loss rate due to transitions to non-trappable states induced by black-body radiation [84] would, however, remain unchanged, ultimately limiting the lifetime to 7 s [56]. As a result, the optimal signal-to-noise ratio after a single measurement would be $k_{\mathrm{col}}/\sigma_{k_{\mathrm{col}}} = 1.8$ after 133 round-trips, rather than $k_{\mathrm{col}}/\sigma_{k_{\mathrm{col}}} = 1.0$ after 85 round-trips.

The number of collisions that take place depends on the overlap of the ammonia packet with the hydrogen beam. In this case, the hydrogen beam (traveling at about 2000 m/s) is much faster than the ammonia beam (traveling at about 140 m/s), so that the loss rate depends on the integrated time-of-flight signal of the hydrogen beam. Fig. 3.14 shows the results of an experiment in which the intensity of the hydrogen beam is changed by increasing the hydrogen backing pressure behind the valve. The measured loss rate of the stored ammonia molecules due to collisions with hydrogen molecules is plotted as a function of the integral over the time-of-flight profiles of the hydrogen beam. As expected, the dependence of the loss rate on the number of molecules in the beam is linear.

While being trapped in the synchrotron, ammonia molecules oscillate around the position and velocity of the synchronous molecule — the molecule that travels with exactly the right speed along the equilibrium orbit. Molecules that oscillate with a large amplitude may have a slightly different overlap with the beam, resulting in a different loss signal. To check whether this is the case, time-of-flight measurements were made of the probe and reference packets after

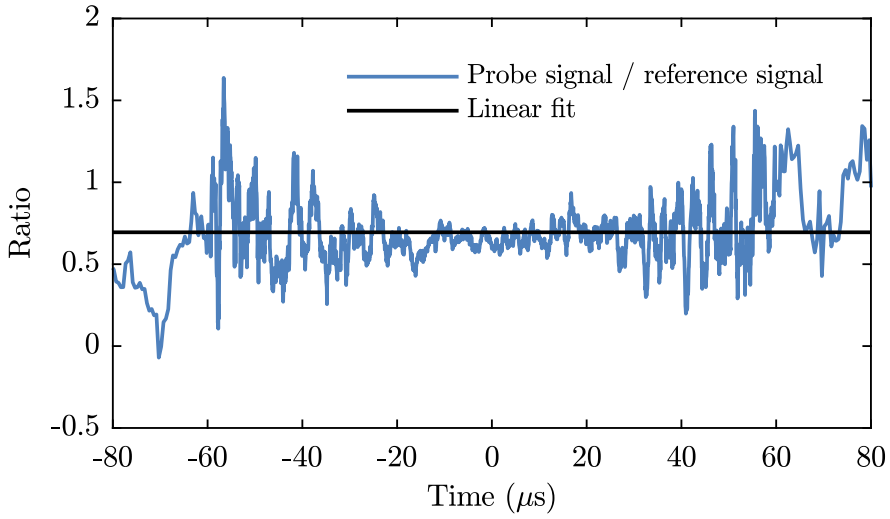

Figure 3.15 – Ratio of the signals of the probe and reference beams as a function of detection time. The black line shows a weighted linear fit.

completing 103 and a quarter round-trips in the synchrotron. Fig. 3.15 shows the signal of the probe beam divided by that of the reference beam as a function of time. Each data point is averaged over 20 shots. The signal of the probe packet is smaller than that of the reference packet, so that the ratio of the two is below 1. As the density of the ammonia packets decreases away from the center, the noise in the wings of the distribution is larger than at the center. No significant deviation from a straight line is observed over the time-of-flight profile. This is an important conclusion as it will greatly simplify our analysis (*vide infra*).

3.5.2 Model to extract the relative cross section from the measured loss rates

The measurements presented in the previous paragraph demonstrate the unique properties of a molecular synchrotron for studying collisions, in particular the high sensitivity owing to the fact that collision signal can be accumulated over the long time that the molecules are stored. Our next goal is to determine the relative (integral, total) cross sections from the measured loss rates. In order to determine these, a detailed understanding of how the ammonia molecules move through the argon packets is required. Which parts of the argon packet do the ammonia molecules encounter? What are the velocities of the argon atoms in these parts? What is the density of the argon beam in these parts? To answer these questions, trajectory simulations will be performed. Concretely, the goal of the simulations is to find (1) an expectation value for the amount

of encountered argon atoms, and (2) the corresponding distribution of collision energy.

The number of argon atoms encountered can be found by integrating the argon density over the volume probed by the ammonia molecules as they revolve around the synchrotron. As a warming up exercise, let us first consider the simple case of an ammonia molecule flying along a path C through a homogeneous gas of argon atoms, with $\langle v_{\mathrm{Ar}} \rangle = 0$ and number density n. Through-out this section, the position and velocity of the ammonia molecule will be denoted by $\vec{r} = (x, y, z)$ and $\vec{v} = (v_x, v_y, v_z)$, respectively. We will first assume that the collision cross section σ_{tot} is independent of relative velocity. In this case, the average number of argon atoms encountered by the ammonia molecule is

$$\langle N_{\mathrm{coll}} \rangle = \int_C \sigma_{tot}\, n \, \mathrm{d}s = \int_{t_i}^{t_f} \sigma_{\mathrm{tot}}\, n\, |v(t)|\, \mathrm{d}t = L\, \sigma_{\mathrm{tot}}\, n,$$

where the path C is parametrized by

$$C : z(t), v(t), \quad t_i \leq t \leq t_f,$$

and where

$$L = \int_{t_i}^{t_f} |v(t)|\, \mathrm{d}t$$

is simply the path length.

In the actual experiment, of course, the argon gas is not homogeneously distributed. On the contrary: since the argon beam results from a supersonic atomic beam, it will have a distribution that depends strongly on position and time. Furthermore, the velocity distribution of the argon atoms is important: both the effective path length $\mathrm{d}l = |\vec{v}_{\mathrm{rel}}(t)|\, \mathrm{d}t$ and the collision cross section $\sigma_{\mathrm{tot}}(E_{\mathrm{col}})$ depend on the velocity of the argon atoms. Thus, we need the argon atom number density $n(\vec{r}|\vec{v}_{\mathrm{Ar}}, t)$ as function of position, for any argon velocity and time, so that we can find the number of argon atoms that are encountered by an ammonia molecules using

$$\langle N_{\mathrm{coll}} \rangle = \langle \sigma_{\mathrm{tot}} \rangle \int_{t_i}^{t_f} \int_{-\infty}^{+\infty} n(\vec{r}|\vec{v}_{\mathrm{Ar}}, t)\, \mathrm{d}t\, \mathrm{d}v_{\mathrm{rel}},$$

where $\langle \sigma_{\mathrm{tot}} \rangle$ is the result of averaging the collision cross section $\sigma_{\mathrm{tot}}(v_{\mathrm{rel}})$ over the velocities of all argon atoms that are encountered. In our experiments, this average is the only thing we can ever measure. We will now make this general expression more specific such that we obtain a expression that reflects the conditions of our experiment.

As discussed in Section 3.4.1, the longitudinal distribution of the argon beam can be described by multiplying a gaussian velocity distribution with a gaussian spatial distribution, as expressed in Eq. 3.3. Transversely, the argon beam is assumed to be homogeneously distributed over the area that makes up the transverse cross section of the argon beam. As the beam is divergent, the size of this area depends on the longitudinal position and will be denoted by $S(z)$. Note that Fig. 3.10b reveals that the profiles are actually not entirely flat, but the approximation is sufficiently accurate for our purpose. Since contributions of the transverse velocity components of the argon atoms to the collision energy are negligible, we assume $v_{\mathrm{Ar,x}} = v_{\mathrm{Ar,y}} = 0$ so that $v_{\mathrm{Ar}} \equiv |\vec{v}_{\mathrm{Ar}}|\, v_{\mathrm{Ar,z}}$. A general expression of the argon beam is then given by

$$n_{\mathrm{Ar}}(\vec{r}|v_{\mathrm{Ar}}, t) = N\, f^{v}_{\mathrm{Ar}}(v)\, \mathrm{d}v\, f^{z}_{\mathrm{Ar}}(z|v, t)/S(z),$$

for $(x, y) \in S(z)$, where N is the number of atoms in the packet.

The transverse cross section $S(z)$ can be parameterized by

$$S(z) = S(z_0) \cdot (1 + (d(z - z_0))^2),$$

where $S(z_0)$ is the cross section at the position where the argon beam crosses the equilibrum orbit (the first time), and where d describes the divergence of the beam. The cross section of the beam at z_0 is shown in Fig. 3.11. Both $S(z_0)$ and d are determined from the trajectory calculations described in Section 3.4.

As the total number of atoms in the beam is not of interest, we will write the argon beam density as:

$$n_{\mathrm{Ar}}(\vec{r}|v_{\mathrm{Ar}}, t) \equiv n_0\, L \cdot f^{v}_{\mathrm{Ar}}(v_{\mathrm{Ar}})\, \mathrm{d}v_{\mathrm{Ar}} \cdot f^{z}_{\mathrm{Ar}}(z|v_{\mathrm{Ar}}, t) \cdot q(\vec{r}), \tag{3.6}$$

where n_0 is the peak number density in the packet at z_0 and a L is a measure for the length of the (Gaussian-shaped) packet, respectively, such that $n_0\, L = N/S(z_0)$ is the column density of the argon packet at z_0. The newly introduced function

$$q(\vec{r}) = \begin{cases} \frac{1}{1+(d(z-z_0))^2} & \text{if } (x, y) \in S(z) \\ 0 & \text{otherwise,} \end{cases}$$

is a shorthand to reduce the length of future equations. This function describes whether the transverse position of the ammonia molecule is located within the argon beam (or not), and also accounts for the decreasing density of the argon beam due to its divergence.

Finally, since we are interested in the number of argon atoms encountered as a function of the collision energy rather than as a function of argon atom velocity, we perform a change of integration variable from v_{Ar} to v_{rel} using the relation

$$v_{\mathrm{rel}} = |v_x\hat{x} + v_y\hat{y} + (v_z - v_{\mathrm{Ar}})\hat{z}|.$$

Putting all of this together, we find for the expectation value for the number of encountered argon atoms

$$\begin{aligned}\langle N_{\text{coll}}\rangle\,(t_{\text{valve}}) &= \langle\sigma_{\text{tot}}\rangle\, n_0\, L \int_{t_i}^{t_f} \mathrm{d}t \int_{-\infty}^{+\infty} \mathrm{d}v_{\text{rel}} \ldots \\ &\quad \left\{ f^z_{\text{Ar}}(z|v_{\text{Ar}},t)\cdot f^v_{\text{Ar}}(v_{\text{Ar}})\cdot v_{\text{rel}}\cdot \frac{\mathrm{d}v_{\text{Ar}}}{\mathrm{d}v_{\text{rel}}}\cdot q(\vec{r}(t))\right\} \\ &\equiv \langle\sigma_{\text{tot}}\rangle\, n_0\, L \int_{-\infty}^{+\infty} g^{N_{\text{coll}}}(v_{\text{rel}})\,\mathrm{d}v_{\text{rel}} \\ &\equiv \langle\sigma_{\text{tot}}\rangle\, n_0\, \beta\, L \int_{-\infty}^{+\infty} f^{N_{\text{coll}}}(v_{\text{rel}})\,\mathrm{d}v_{\text{rel}} \\ &= \langle\sigma_{\text{tot}}\rangle\, n_0\, \beta\, L,\end{aligned} \tag{3.7}$$

where a few new quantities have been introduced. Firstly, $g^{N_{\text{coll}}}(v_{\text{rel}})\,\mathrm{d}v_{\text{rel}}$ is the result of the path integral over the argon density distribution. In order to aid the interpretation of this result, however, it is separated out into a parameter β and distribution $f^{N_{\text{coll}}}(v_{rel})\,\mathrm{d}v_{rel}$. The former, called the beam-overlap, is a parameter between 0 and 1 that describes the effective length of the part of the argon packet that is probed by the ammonia molecules, relative to the total length of the packet. The latter is a normalized distribution function that describes the distribution of the relative velocities of the argon atoms that are encountered. This function determines the energy resolution of the determined cross section.

The model is implemented as follows. Firstly, the trajectory simulations calculate the beam-overlap, in the form of $g^N(v_{\text{rel}})\,\mathrm{d}v_{\text{rel}}$. The cross section and beam densities are not included. The beam-overlap is calculated by numerically integrating the path of the synchronous molecule from t_i to t_f. The simulation calculates, on every (variably-sized) time-step Δt_i, for every velocity $v_{\text{rel,j}}$ on a grid with spacing Δv_{rel}:

$$\begin{aligned}&g^z_{\text{Ar}}\left\{z(t)|z_{\text{valve}} + v_{\text{Ar}}(v_{\text{rel}},\vec{v}(t))\cdot(t-t_{\text{valve}}), v\ pw\right\}\cdot\ldots \\ &g^v_{\text{Ar}}\left\{v_{\text{Ar}}(v_{\text{rel}},\vec{v}(t))|\left\langle v_{\text{Ar}}\right\rangle,\sigma_{\text{v}_{\text{Ar}}}\right\}\cdot\ldots \\ &\frac{\mathrm{d}v_{\text{Ar}}}{\mathrm{d}v_{rel}}\, q\left\{\vec{r}(t)\right\}\ v_{\text{rel,j}}\,\Delta t_i\,\Delta v_{rel},\end{aligned} \tag{3.8}$$

where g^z_{Ar} and g^v_{Ar} are the normal distributions from Eq. 3.3, and adds it to a histogram over v_{rel}. This provides us with the relative velocity distribution of the beam-overlap, $g^{N_{\text{coll}}}(v_{\text{rel}})$, which is then integrated over v_{rel} to find the beam-overlap, β. The simulations were performed using ammonia distributions with different temperatures and by using either a complete model that derives the force on the ammonia molecules from the electric field in

the synchrotron, which was calculated by SIMION [85], or a toy model that assumes a linear restoring force towards the synchronous molecule, using the trapping frequencies from Zieger *et al.* [68]. As the results of these simulations did not differ significantly from each other, we have decided to perform all calculations using the toy model and assuming a zero temperature for the ammonia molecules. Since in this case each round-trip is identical, only a single round-trip is simulated. Note that $\langle N_{\mathrm{coll}} \rangle$ is then simply the number of collisions per round-trip, k_{col}.

3.5.3 Measuring the collision cross section a function of collision energy

We now have all the tools that we need to reach our final goal; to measure the relative, total, integrated collision cross sections as a function of energy. The collision energy can be tuned in three different ways: by varying the velocity of the stored ammonia packets, by varying the temperature of the pulsed valve that releases the argon atoms, and by varying the timing between the supersonic argon beam and the stored ammonia packets. Unfortunately, when we vary the collision energy, other parameters that influence the loss rates of the stored molecules will change as well. For instance, by changing the temperature of the valve that releases the argon beam, the average velocity of the beam will change, but so will the intensity, the velocity distribution and the beam overlap. When we change the velocity of the stored ammonia molecules, the argon beam will remain the same but the beam overlap will change. Luckily, the model that was derived in the previous section tells us how to take all these effects into account.

We will first look at collision measurements as a function of the delay between the trigger of the valve that releases the argon atoms and the arrival time of the ND_3 probe packet in the detection zone. This delay determines whether the ammonia molecules collide with atoms located more in the leading or trailing end of the argon packet, or, in fact, whether they collide at all. As the flight time from the valve to the synchrotron is much larger than the opening time of the valve, there is a strong correlation between the position of the argon atoms and their velocity. Hence, the delay determines the velocity of the argon atoms that are encountered by the ammonia beam. Note that in our experiments, the relative velocities are such that ammonia molecules only see part (20–30%) of the argon packet during the time they spend in the collision zone.

Figures 3.16 and 3.17 show the ammonia loss rate measured as a function of the delay, for ammonia with velocities of 121.1 m/s and 138.8 m/s, respectively. The temperature of the valve that releases the argon atoms is kept at temperatures between −120 to 30°C as indicated in the figures. Each data point is the result of a 4 minute collision measurement, such as the one depicted in Fig. 3.12. To be robust against possible drifts of the argon density, the data were taken while toggling between the two ammonia speeds after every data

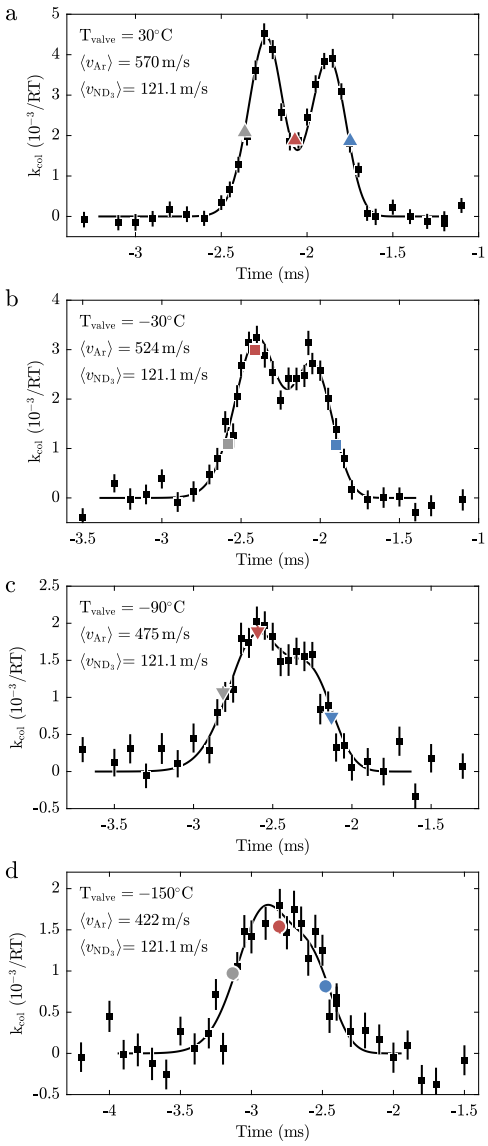

Figure 3.16 – Measured loss rate as a function of the delay between the trigger of the valve and the arrival time of the ammonia packets at the detection zone, for $v_{ND_3} = 121.1\,m/s$. Panels a–d depict measurements with different temperatures of the valve housing that result in different average velocities, as indicated in the top left corners. The black squares represent measurements containing 2400 shots each, while the coloured points represent measurements containing 21,600 shots each. The error bars, for the coloured points obscured by the symbols, denote the standard errors. The black lines show the results of simulations described in Section 3.5.2, scaled to fit the data in each panel. The reduced χ^2's of the fits are 0.93, 1.01, 1.09, and 1.31 for panels a–d, respectively.

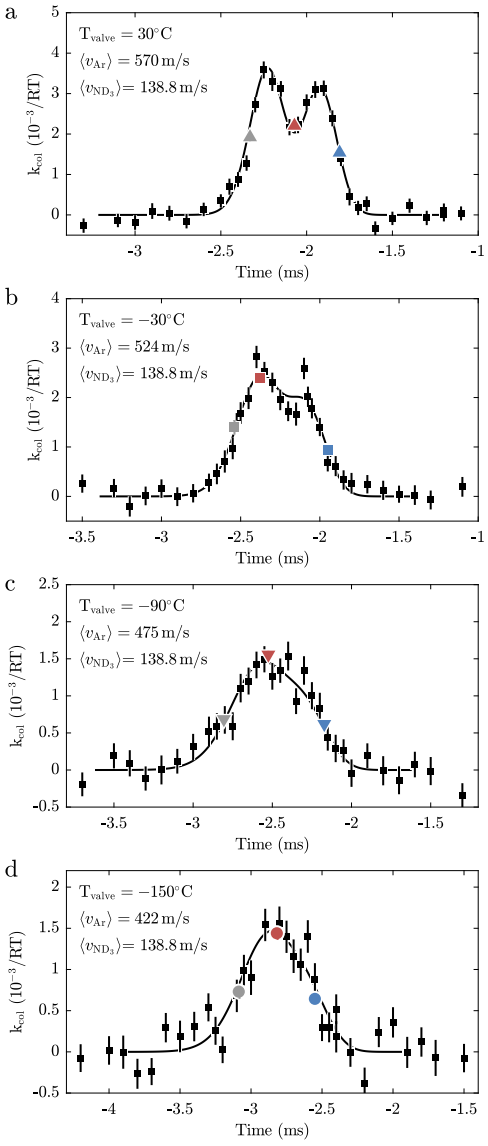

Figure 3.17 – Same as Fig. 3.16, but for $v_{ND_3} = 138.8\,m/s$. The reduced χ^2's of the fits are 0.98, 0.89, 0.79, and 1.39 for panels a–d, respectively.

point and picking the timings from a list in a random order. As observed, the scans feature two peaks rather than one, resulting from the fact that the argon beam intersects the synchrotron at two distinct locations. These peaks become less well resolved as the argon packets become slower and concomitantly longer.

Additional data were taken at three specific timings of the argon beams, shown in Fig. 3.16 and Fig. 3.17 as the blue, red and grey symbols. The blue data points are measured using a short time delay between the valve and the arrival time of ammonia packet. Hence, in this case, the ammonia molecules probe the fast part of the argon beam. The red points are measurements that probes the central part of the argon beam, while the grey points are measurement that probes the slow part. Each of these measurements is the result of 21,600 shots, corresponding to a measurement time of 36 minutes per point. To detect and correct for possible drifts of the Ar beam density during the measurements, we cycled nine times through the six different configurations. No significant drifts were detected.

The solid curves in Fig. 3.16 and Fig. 3.17 show results of simulations of our experiment using the model discussed in Section 3.5.2. The simulation uses as input the velocity and equilibrium radius of the synchronous molecule taken from simulations of the synchrotron [68] as discussed in Section 3.3, and the longitudinal and transverse position and velocity distributions of the argon beams derived in Section 3.4. The horizontal displacement of the argon beam relative to the equilibrium orbit of the ammonia molecules was varied in order to optimize the fit (simultaneously for all 8 curves). From this we find (1) that the argon beam is displaced by 1.6 mm from the ammonia molecules' equilibrium orbit, which corresponds to a 58 mm distance between the two points around which the particles interact, and (2) the position of the crossing point with respect to detection zone II. The former determines the time difference between the peaks in Figures 3.16 and 3.17, while the latter determines an off-set for the time axis. Furthermore, the simulations are scaled vertically to match the experimental data for each of the 8 curves individually. As seen from the figure, the simulations describe the measurements very well. For instance, the width of the distributions is well reproduced and so is the difference in signal at the two peaks. This agreement confirms that we have an excellent understanding of the experiment.

From the simulations we retrieve the distributions of the relative velocities of the encountered argon atoms, which are shown in Figures 3.18 and 3.19. Each panel in Figures 3.18 and 3.19 corresponds to a panel in Figures 3.16 and 3.17. The black curves in Figures 3.18 and 3.19 show the distribution of collision energies integrated over the entire argon beam – this distribution is relevant when the cross section is found by scaling the simulation to the entire delay scan shown in Figures 3.16 and 3.17. The blue, red and grey curves in Figures 3.16 and 3.17 show the collision energy distributions for the data points taken in the front, middle and back part of the argon gas pulse, respectively. As in this case only part of the argon beam is probed, the distributions are more sharply peaked. As expected, the blue curve is centered at higher collision

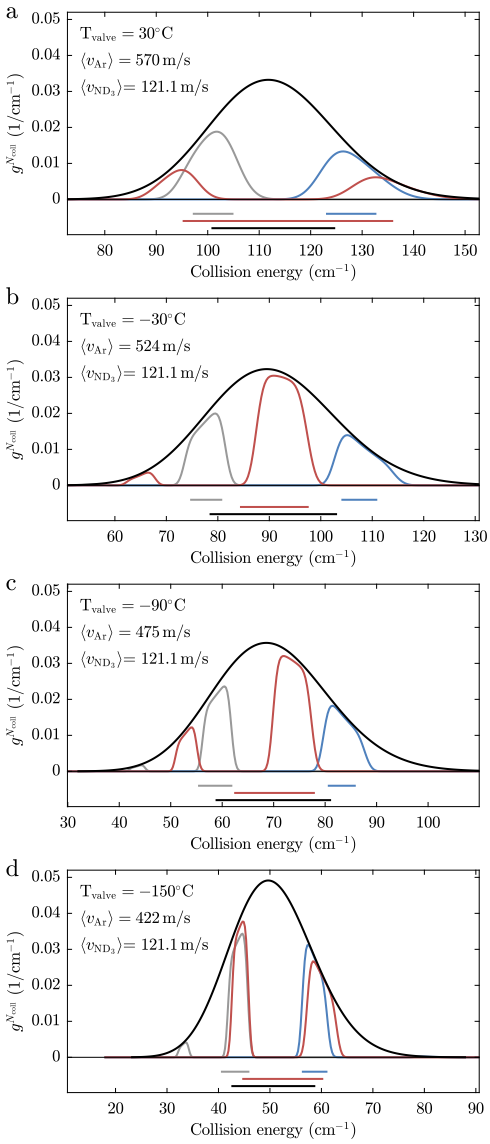

Figure 3.18 – Collision energy distributions for collision experiments with $v_{ND_3} = 121.1\,m/s$ determined from simulation. The black curves represent the distribution for collision measurements that combine the measurements at each valve timing, i.e. all the black squares in Figures 3.16 and 3.17. Since the complete argon packet is probed in this way, this distribution corresponds simply to the longitudinal velocity distribution of the argon beam at a particular temperature. The grey, red, and blue curves represent the collision energy distributions for the collision measurements indicated by the grey, red, and blue data points in Figures 3.16 and 3.17. The grey, red, blue, and black bars in the bottom of each graph represent the widths of the distributions, as they are displayed by the horizontal error bars in Fig. 3.20.

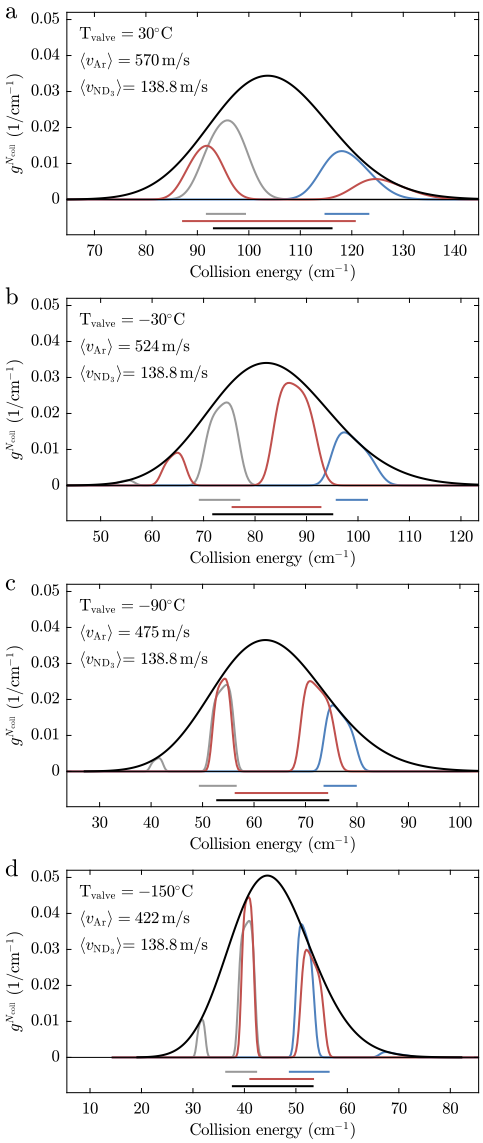

Figure 3.19 – Same as Fig. 3.18, but for $v_{ND_3} = 138.8\,m/s$.

energies than the average, while the grey curve is centered at lower collision energies. The red curve is bi-modal which is an obvious disadvantage of the chosen alignment of the argon beam.

The bars below Figures 3.18 and 3.19 depict the standard deviation of the collision energy distributions, which are a measure for the energy spread of the collisions which are probed in our measurement. Clearly, the interpretation of the standard deviation is not obvious in the case of bi-modal distributions, but we will use these for lack of a better measure.

We are now ready to retrieve the relative cross section as function of energy. Rewriting Eq. (3.7), we obtain an equation that relates the cross section to the measured loss rates:

$$\langle \sigma_{\mathrm{tot}} \rangle = \frac{n_{0,c}\, n_{0,\mathrm{rel}}\, \beta\, L}{k_{\mathrm{col}}},$$

where the argon beam densities (at position z_0) are written as the product of $n_{0,c}$, the absolute density of the argon beam at $T_{\mathrm{valve}} = -150°\mathrm{C}$ and $f_{\mathrm{rep}} = 153\,\mathrm{Hz}$, and $n_{0,\mathrm{rel}}$, the relative argon beam densities as presented in Table 3.1, together with the length of the argon pulses L. The beam overlap, β, is taken from the simulations.

Before presenting our final result, there is one more thing to consider. In our experiment we determine the loss rate of ammonia molecules stored in a synchrotron due to collisions with argon atoms. Although most collisions lead to loss, a small ($\sim$10%) but significant fraction of elastic collisions takes place at such large distances that the ammonia molecules remain trapped in the ring. To correct for this effect we multiply the found loss rates with an energy dependent correction factor. This correction factor is calculated by combining our knowledge of the trapping potential with the differential collision cross section (the cross section as a function of scattering angle) from quantum close-coupling calculations of ND_3 + Ar collisions, performed by Loreau and van der Avoird [58]. A detailed explanation is given in Appendix A of Chapter 2.

Fig. 3.20 presents the resulting cross sections together with their uncertainties and collision energy distributions as determined by the simulations. The blue, red, and gray points in Fig. 3.20 are obtained from measurements at the front, center, and back of the argon beams at four different temperatures of the valve. The black data points result from averaging over all timings; these are the scaling factors obtained by fitting the simulated delay scans to the measurements shown in Figures 3.16 and 3.17. The open and closed symbols are measured with ammonia molecules that have a velocity of 138.8 and 121.1 m/s, respectively. The uncertainties in the cross sections, in the range of 7–14%, are a combination of the uncertainties of the relative argon intensities (presented in Table 3.1, typically between 6–9%) and the uncertainties in the measured loss rates (as shown in Figures 3.16 and 3.17, typically between 2–11%). The fact that we find consistent results when the collision energy is changed in different ways, gives us great confidence in the measured cross sections. Note that the loss rates from which the cross sections are derived vary from 0.5×10^{-3} to 3×10^{-3} per round-trip.

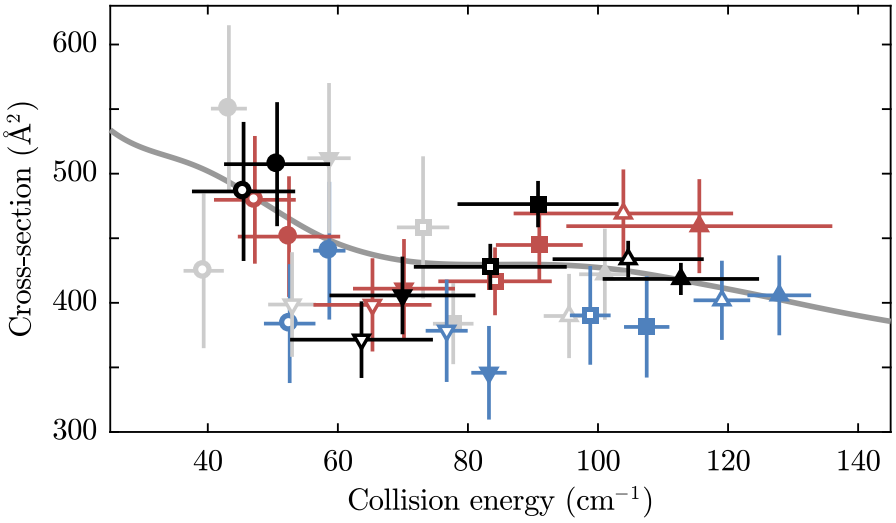

Figure 3.20 – Total, integrated, ND_3 + Ar collision cross section versus collision energy. The meaning of the black, grey, red, and blue points is described in the main text. The vertical error bars denote standard errors, the horizontal error bars denote the collision energy distributions as depicted in Figures 3.18 and 3.19. The grey line shows the result of scattering calculations, convoluted with a normal distribution with a standard deviation of $5\,\mathrm{cm}^{-1}$ [58]. The measurements are collectively fit to this calculation with a single global scaling factor that represents the density of the argon beam at T = −150°C, which is found to be $7.8{\times}10^9\,\mathrm{cm}^{-3}$. $\chi^2_{\mathrm{red},\nu=31} = 1.3$.

The solid line also shown in Fig. 3.20 is the result of theoretical calculations performed by Loreau and van de Avoird [58], convoluted with a normal distribution with a standard deviation of $5\,\mathrm{cm}^{-1}$. The measurements are collectively fit to this calculation with a single global scaling factor that represents the density of the argon beam at T = −150°C, which is found to be $7.8{\times}10^9\,\mathrm{cm}^{-3}$ about 1.2 m down-stream from the valve. This density is in agreement with a crude estimate of the density from the REMPI-measurements. In future, we plan to measure the density more accurately using a femtosecond laser, in a similar fashion as Meng *et al.* [71]. Although the ND_3 + Ar collision cross section in this energy range does not show spectacular features, the shallow minimum around $70\,\mathrm{cm}^{-1}$ predicted by theory is reproduced in the experiment.

3.6 Conclusions

We have performed the first scattering experiment using a molecular synchrotron. Our measurements demonstrate that, by accumulating collision signal over the long time that the ammonia molecules are stored, the sensitivity is spectacularly increased. This high sensitivity has allowed us to measure the relative, total, integral cross section for ND_3 + Ar collisions over an energy

range of 40—140 cm^{-1} with a precision of a few percent. The collision energy was tuned in three different ways: (1) by changing the temperature of the valve that releases the argon atoms, (2) by changing the velocity of the stored packets of ammonia, and (3) by choosing which part of the argon packet, dispersed during its 1.2 m traversal from the valve to the synchrotron, is probed by the ammonia molecules. These measurements give consistent results and agree with theoretical scattering calculations.

Besides the enhanced sensitivity and the low energy that is obtained by using co-propagating beams, our method has a number of additional features that make it attractive: (i) By comparing packets that are simultaneously stored in the synchrotron, the measurements are independent of the ammonia intensity and immune to variations of the background pressure in the synchrotron. (ii) As the probe packets interact with many argon packets, shot-to-shot fluctuations of the argon beam are averaged out. By rapidly toggling between different ammonia velocities and timings, slow drifts of the argon beam intensity are eliminated.

A detailed characterization of the argon beams was crucial for obtaining a high precision. To retrieve the collision cross section from the measured loss rates, trajectory simulations were used to evaluate the overlap of the ammonia packet with the argon beam. These simulations were also used to access collision energy distributions that occur experimentally.

Measurements have shown that the (in-plane) alignment of the argon with respect to the synchrotron needs to be carefully considered. In the experiments presented here, the alignment was chosen in such a way that the argon beam crossed the path of the ammonia molecules at two distinct positions. This made it easy to check the validity of the simulations. A better energy resolution would be obtained, however, when the beamline would either be moved further inwards such that the collision zones are sufficiently far away from each other, or be moved outwards until only a single collision zone is left. The highest resolution would be obtained (at the cost of increasing the collision energy) by crossing the beams at right angles. This would make it possible to resolve the fine-structure on the elastic cross section due to scattering resonances [58].

The collision energy is currently limited by the large difference between the velocity of the stored molecules and the velocities in the supersonic beam. Lower collision energy can be reached by using molecules from cryostatically cooled beams as collision partner [72]. As these beams typically have a much longer temporal profile, they would overlap with multiple packets. However, even in this case there will be packets that have no overlap and can serve as reference. Another strategy would be to use a larger synchrotron which would be able to store ammonia molecules at a higher velocity. Ideally, a synchrotron would be used that can store molecules directly from a supersonic beam without deceleration, resulting in higher densities. As the radius of the ring scales with the square of the forward velocity, such a ring would have to be $\sim$10 times larger (if the same voltages are used). Such a ring could be used to store beams both clockwise and anticlockwise, which makes it possible to perform

calibration measurements at high energy. In this way it will be possible to measure collision energies from 0–2000 cm^{-1} in the same apparatus. Note that if the velocities of the beams are more similar, the energy resolution will also be improved [24], ultimately limited to the temperature of the stored ammonia packets. Finally, collision studies with paramagnetic atoms and molecules, such as hydrogen – the most abundant atom in the universe – could be performed in a magnetic synchrotron, as described in Chapter 4.

CHAPTER 4

A compact design for a magnetic synchrotron to store beams of hydrogen atoms[1]

In this chapter, a design is presented for an atomic synchrotron consisting of 40 hybrid magnetic hexapole lenses arranged in a circle. We show that for realistic parameters, hydrogen atoms with a velocity up to 600 m/s can be stored in a 1-meter diameter ring, which implies that the atoms can be injected in the ring directly from a pulsed supersonic beam source. This ring can be used to study collisions between stored hydrogen atoms and supersonic beams of many different atoms and molecules. The advantage of using a synchrotron is two-fold: (i) the collision partners move in the same direction as the stored atoms, resulting in a small relative velocity and thus a low collision energy, and (ii) by storing atoms for many round-trips, the sensitivity to collisions is enhanced by a factor of 100-1000. In the proposed ring, the cross-sections for collisions between hydrogen, the most abundant atom in the universe, with any atom or molecule that can be put in a beam, including He, H_2, CO, ammonia and OH can be measured at energies below 100 K. We discuss the possibility to use optical transitions to load hydrogen atoms into the ring without influencing the atoms that are already stored. In this way it will be possible to reach high densities of stored hydrogen atoms.

[1]Based on Aernout P.P. van der Poel, Katrin Dulitz, Timothy Softley, Hendrick L. Bethlem, *A compact design for a magnetic synchrotron to store beams of hydrogen atoms*, New. J. Phys. **17**, 055012 (2015).

4.1 Introduction

The ability to control the translational energy and the energy spread of a molecular beam enables collision studies that probe molecular interaction potentials in great detail [11, 14, 15]. A holy grail of this research is to be able to observe resonances in the collision cross-section as a function of collision energy. These resonances occur when the kinetic energy of two colliding molecules is converted into rotational energy as a result of the anisotropy of the potential energy surface (PES). This leaves the molecules with insufficient translational energy to overcome the Van der Waals attraction, transiently binding the molecules together [63]. These long-lived excitations of the collision complex appear as sharp resonances in graphs of the cross-section as a function of the collision energy. The position and width of these resonances provide an extremely sensitive probe of the interaction potential energy surfaces [62, 86]. Since these resonances arise from the rearrangement of rotational energy, they do not occur for cold atom-atom collisions. Another motivation for research into cold collisions is the fact that, at low temperatures, the collision process becomes sensitive to externally applied electric or magnetic fields, which gives a handle to control and steer the outcome of a chemical reaction [87, 88].

The crossed-molecular-beam method pioneered by Dudley Herschbach and Yuan T. Lee has yielded a detailed understanding of how molecules interact and react [59, 60]. In this method, beams of atoms and molecules in high vacuum are crossed at right angles and made to collide. Inhomogeneous electric and magnetic fields can be used to prepare the molecules in selected quantum states and to orient them before the collision, while laser techniques in combination with sophisticated ion optics can be used to determine both the quantum state of the products and their kinetic energy. The collision energy in a crossed-beam experiment is determined by the velocity of the molecular beams and is typically around $1000\,\mathrm{cm}^{-1}$. Therefore, while there is plenty of data available at high energy, experimental data for low-energy collisions is scarce.

Recently, collision studies have been performed between Stark-decelerated beams of OH radicals and conventional beams of rare gas atoms in a crossed-beam geometry. In these experiments, the total collision energy is tuned from 100 to $600\,\mathrm{cm}^{-1}$ by varying the velocity of the OH radicals, while the velocity of the rare-gas beam is kept fixed. In this way the threshold behavior of state-to-state inelastic scattering cross-sections was accurately determined [37, 89, 90]. Experiments have also been conducted using collisions between Stark-decelerated OH molecules and a state-selected beam of NO molecules [38].

Low collision energy can also be attained by performing crossed-beam experiments at low crossing angle [3]. In recent experiments, scattering resonances were observed in collisions between O_2 or CO and hydrogen molecules at energies between 5 and 30 K [20, 21]. Even lower temperatures can be obtained by using magnetic [22, 23] or electric guides [26, 27] to merge two molecular beams into a single beam. The collision angle is zero in this case, so that the relative velocity of the reactants in the centre-of-mass frame be-

comes simply the difference between the two beam speeds. In contrast to a crossed-beam experiment this difference can become zero even at high beam velocities, thus rendering the slowing of the molecules unnecessary. Until now, experiments with merged supersonic beams have been restricted to penning ionization collisions of metastable He or Ne atoms.

In a different approach, trapped ions at millikelvin temperatures are monitored while a slow beam of molecules passes through the trap to study reactive ion-molecule collisions [45, 46]. The advantage of this method is that the ions are stored for a long time while their number can be accurately determined, allowing the detection of reactions even when they occur at a rate of one per minute. In a similar fashion, collisions of slow beams of ammonia with magnetically trapped OH molecules were observed [47].

Here, we discuss the possibility to study collisions between hydrogen atoms stored in a magnetic synchrotron and supersonic beams of different atoms and molecules, combining the virtues of the two approaches mentioned above:

(i) The collision partners move in the same direction as the stored molecules, resulting in a small relative velocity and thus a low collision energy.

(ii) The sensitivity to collisions is enhanced by orders of magnitude by storing the atoms during many round-trips.

We present a design for a synchrotron consisting of 40 hybrid magnetic hexapole lenses arranged in a circle. We show that, for realistic parameters, a significant fraction of a supersonic beam of hydrogen atoms with a velocity of 600 m/s can be directly loaded into a 1-meter diameter ring.

4.2 Storage rings for neutral particles

In its simplest form, a storage ring is a trap in which the particles possess a minimum potential energy on a circle rather than having a minimum potential energy at a single location in space. The advantage of a storage ring over a trap is that packets of particles with a non-zero mean velocity can be confined. While circling the ring, these particles can be made to interact with other particles repeatedly, at well-defined times and at distinct positions [53]. A simple storage ring for polar molecules or paramagnetic atoms and molecules can be devised by bending a magnetostatic or electrostatic hexapole guide into a torus, such as the 1m-diameter magnetic storage ring used by Kügler *et al.* to store cold neutrons [91] or the 0.25m diameter electrostatic storage ring used by Crompvoets to store Stark-decelerated ammonia molecules [53]. A strong-focusing storage ring for slow (100 m/s) atomic hydrogen in high-field seeking states was proposed by Thompson *et al.* [92].

In a storage ring, an injected packet of atoms and molecules will gradually spread out along the ring as a result of its longitudinal velocity spread, eventually filling the entire ring. To fully exploit the possibilities offered

by a ring structure, it is necessary that the particles remain in a bunch as they revolve around the ring, ensuring a high density of stored particles and making it possible to inject multiple packets into the ring without affecting the packet(s) already stored. Thus, in addition to the transverse forces that focus the particles and keep them on a circular orbit, we need to apply a force in the longitudinal direction. In modern-day particle accelerators, the different tasks are performed by separate elements (RF-cavities for bunching, magnetic quadrupoles for transverse focusing, and dipole magnets for bending). An elaborate design of a synchrotron for polar molecules in low-field and high-field seekings states based on this approach was presented by Nishimura *et al.* [93]. Because of its low degree of symmetry, however, this design is seriously hindered by non-linearities in the forces experienced by the molecules.

A different approach was taken by Heiner *et al.* who demonstrated a synchrotron consisting of two hexapoles which were bent into a semi-circle and separated by a short gap [54]. By appropriately switching the voltages applied to the electrodes as the molecules pass through the gaps between the two half rings, molecules experience a force that keeps them together in a compact bunch. In this design, the necessary bunching, bending and focusing forces are delivered by a single element. This allows for a much more compact design of high symmetry that is much less sensitive to non-linearities. A synchrotron consisting of 40 straight electric hexapoles arranged in a circle with a radius of 250 mm was subsequently demonstrated by Zieger *et al.* [56]. In this ring, packets of bunched molecules were observed to make up to 1025 round-trips, thereby passing a distance of over 1 mile. Up to 26 molecular packets were stored simultaneously in this ring structure; 13 revolving clockwise and 13 revolving counter-clockwise [68].

In this paper, we discuss the feasibility of a magnetic synchrotron. Compared to electric fields, magnetic fields offer many technical challenges but also some new possibilities. A synchrotron consisting of 40 electromagnetic hexapoles, the exact counterpart of the electric synchrotron discussed above, would demand an impractically large cooling capacity owing to Ohmic heating caused by the required application of very high currents. However, large magnetic fields can also be produced by permanent magnets. Nowadays, inexpensive magnets made from rare-earth metals with a surface magnetization of up to 1.4 T are commercially available in various sizes. Such magnets have been used in a number of experiments to manipulate paramagnetic atoms and molecules. For instance, curved quadrupole, hexapole and octupole guides based on permanent magnets in a Halbach configuration [94] have been used to manipulate slow atomic beams [95–98]. By extending such a guide, a simple magnetic storage ring can be devised. However, methods are needed (i) to allow loading atoms into such a ring and (ii) for bunching the atoms stored in it. Here, we present a design for a synchrotron that uses hybrid hexapole lenses. This design combines the strong magnetic fields offered by permanent magnets with the flexibility of electromagnets.

The paper is organized as follows. In Section 4.3, we will describe the

magnetic field resulting from a single hybrid lens and show that, by changing the currents through the electromagnets, we can provide all necessary forces for loading, bending, focusing and bunching. In Section 4.4, we calculate the transverse and longitudinal acceptance for a ring composed of 40 of these lenses arranged in a circle with a diameter of 1 meter. Finally, in Section 4.5 we discuss how we plan to use this synchrotron for studying collisions between atomic hydrogen and various atoms and molecules at low temperatures.

4.3 A hybrid magnetic hexapole

Figure 4.1(a) shows a schematic drawing of a hybrid lens composed of six permanent magnets and six current-carrying wires with a diameter of 0.45 mm, each wound six times around the aluminum housing. The inner radius of the lens is chosen to be $r_i = 4\,\text{mm}$. A 1.8 mm wide slit allows atoms to be injected off axis

The permanent magnets are made from NdFeB that have a remanence of $B_0 = 1.3\,\text{T}$. The magnetization vector of each magnet is rotated by 180 degrees with respect to its neighboring magnet to approximate a hexapole field. Figure 4.1(d) shows a density plot of the magnetic field magnitude B (in T) and flux lines (using B_ϕ) obtained from simulations in Radia 4.29 [99] when the current through the coils is zero. In Fig. 4.1(b), the black curves (denoted by $I = 0\,\text{A}$ in the legend) show the radial dependence of this field for different angles ϕ. The red curve shows a quadratic fit, $B = a_H r^2$, to the calculated magnetic fields, yielding $a_H = 0.031\,\text{T/mm}^2$. Note that adding six more magnets, with their magnetization pointing alternately towards or away from the centre, results in a field that is not only a better approximation to a hexapole field but also two times stronger. Unfortunately, such a field cannot be used as the magnets would block the injection beam.

The permanent-magnet array provides the necessary force to keep atoms confined in the ring. In order to inject new packets into the ring, it is necessary to temporarily reduce the field, which is done by applying a current pulse through the six sets of 0.45 mm thick wires that are wound around the aluminium housing. Figure 1(e) shows the magnetic field magnitude and flux lines inside the lens when a current of 380 A runs in an alternating direction through the six coils. The radial dependence of this field for different angles ϕ is shown by the blue curves in figure 1(b) (denoted by $I = 380\,\text{A}$ in the legend). As observed, the magnetic field of the permanent magnets is almost completely canceled by the electromagnet, illustrating that both fields have a very similar shape. Note that the field far away from the hexapole (not shown) is sufficiently small that it would not deflect the injection beam significantly.

In order to apply a focusing force in the longitudinal direction of the ring to bunch the atoms, we superimpose an oscillating dipole field to the confinement field provided by the permanent magnets. Such a field is created by running opposite currents through the two sets of wires to the left and to the right.

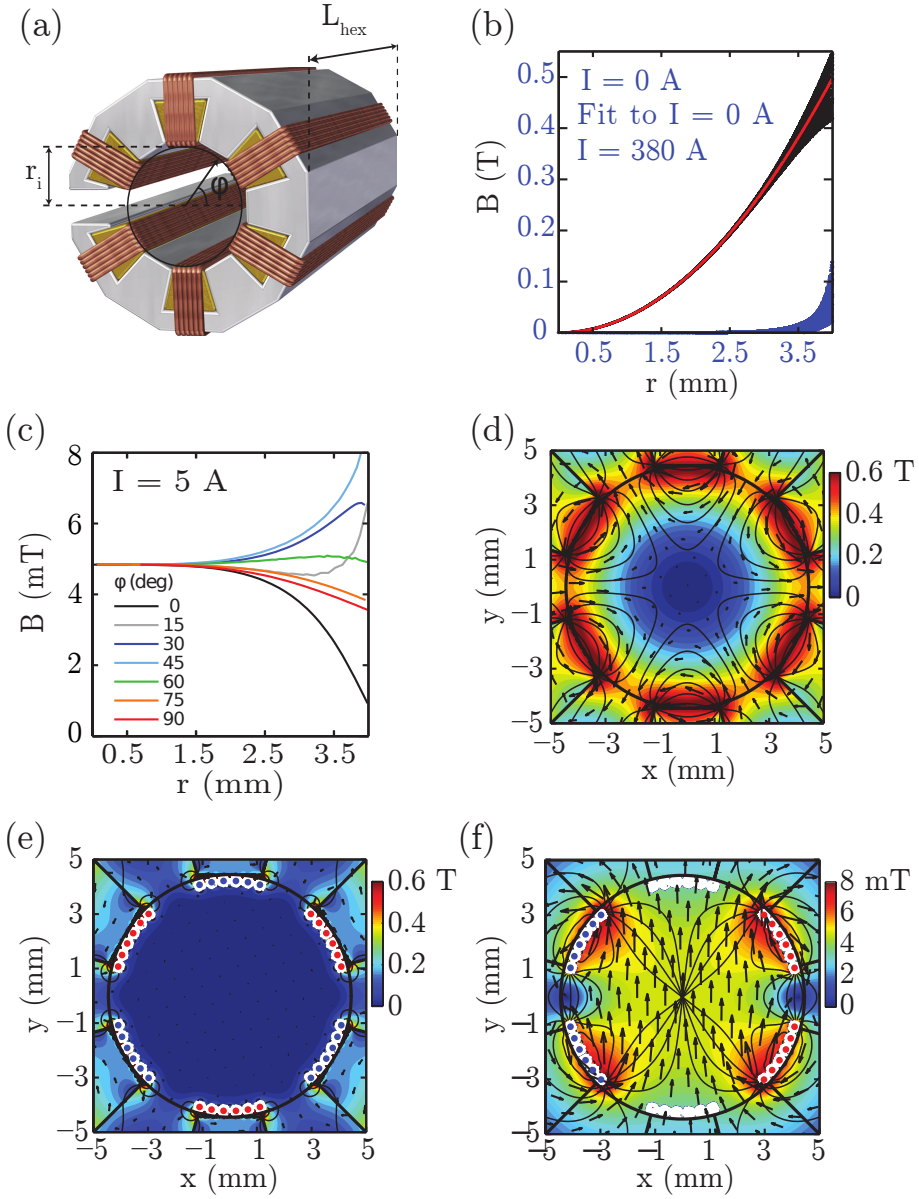

Figure 4.1 – (Continued on the following page.)

Figure 4.1 – (a) Schematic drawing of a hybrid lens composed of six permanent magnets and six sets of six wires held by an aluminium housing. The inner radius of the lens is $r_i = 4\,\text{mm}$ and a 1.8mm-wide slit allows atoms to be injected off axis. (b) Magnetic field magnitude B in the centre of the hexapole assembly (for several angles ϕ) for the configurations in (d) and (e), in which currents of 0 A and 380 A are applied to the electromagnets, respectively. The simulated data for the permanent-magnet arrangement is well-approximated by a quadratic dependency to $a_H r^2$ (red line, yielding $a_H = 0.03\ \text{T/mm}^2$), where a_H is the magnetic field curvature. (c) Magnetic field magnitude B in the centre of the hexapole assembly (for several angles ϕ) for configuration (f). (d) Density plot of the magnetic field magnitude B (in T) and flux lines (using B_ϕ) in the centre of an assembly of six permanent magnets in hexapole configuration, obtained from simulations in Radia 4.29. (e) Same as in (d) but superimposed with a magnetic hexapole field from the six sets of current-carrying wires (filled white circles) operated at a current of 380 A, such that the magnetic field of the permanent magnets is nearly canceled out. Red (blue) dots indicate that the current is directed into (out of) the plane of projection. (f) Density plot of the magnetic field magnitude B (in T) and flux lines (using B_ϕ) for the wires in a dipole configuration. Filled red (blue) dots and open red (blue) dots indicate that currents of 5 A are directed towards (out of) the plane of projection, respectively.

When a current of 5 A is applied, a near uniform field with a magnitude of $B = 5\,\text{mT}$ is generated, as shown in figure 1(f). The corresponding radial dependence is shown by the curves in figure 1(c) (denoted by $I = 5\,\text{A}$). By oscillating this field synchronously with the velocity of the stored packet, atoms can be accelerated or decelerated without influencing the transverse motion. Note that by adding the dipole field to the confinement field, the magnetic field zero is displaced from the geometric centre of the hexapole. By oscillating the dipole field, the zero-point is oscillating around the geometrical centre. As the atoms need to be in sufficiently high magnetic fields to prevent Majorana transitions, the maximum bunching field that can be applied is limited. At 5 A the point of zero magnetic field moves by about 0.4 mm.

As permanent magnets are magnetized by applying a high field to them, one may worry whether the currents used for bunching and injection will demagnetize them. For NdFeB material at room temperature, the applied B field must be quite high to induce a significant decrease of the magnetization [100], and the effect of the bunching field on the permanent magnets is negligible. However, the field required for injection might lead to a slight demagnetization. If this turns out to be significant, this can be compensated by running a small current in the opposite direction to increase the magnetic field. Alternatively the magnets may be remagnetised by applying a strong current pulse in the opposite direction as used for injection.

4.4 A synchrotron consisting of 40 hybrid magnetic hexapoles

In this section, we will estimate the transverse and longitudinal trapping frequencies and the acceptance of a synchrotron consisting of many lenses of the type discussed in the previous section, using models that were developed to analyse the motion through electric storage rings and synchrotrons [53, 54, 56]. Although these models are based on a number of approximations and simplifications, the high degree of symmetry of the ring ensures that the values obtained are sufficiently reliable.

4.4.1 Transverse motion in a hexapole torus

Let us start by considering a storage ring obtained by bending a linear hexapole guide into a torus with a radius R_{Ring}. A hydrogen atom in a low-field seeking state inside this torus will experience two forces; a force directed towards the centre that results from the inhomogeneous magnetic field and a centrifugal force that depends on its forward velocity. These forces cancel at a certain radius which we will refer to as the *equilibrium radius*, r_{equi}:

$$\frac{m v_\phi^2}{R_{\mathrm{Ring}} + r_{\mathrm{equi}}} = -\mu \frac{dB}{dr}(r_{\mathrm{equi}}) = -2\mu a_H r_{\mathrm{equi}}, \tag{4.1}$$

where m is the mass of the hydrogen atom, v_ϕ its longitudinal velocity, and μ the magnetic moment that is in general a function of the magnitude of the magnetic field. If we neglect the hyperfine structure splitting, i.e., if we assume that the Zeeman shift is linear even in zero field, we find

$$r_{\mathrm{equi}} \approx \frac{m v_\phi^2}{2 R_{\mathrm{Ring}} \mu_B a_H} = \frac{v_\phi^2}{R_{\mathrm{Ring}} \omega_r^2}, \tag{4.2}$$

where $\omega_r/2\pi$ is the (radial) betatron frequency and μ_B is the Bohr magneton. If an atom with a certain longitudinal velocity starts at the radius that is appropriate for its speed, it will form a closed orbit with a constant radial position while it revolves around the ring. Atoms flying with the same forward velocity but with a different radial position, or with a non-zero radial velocity, will oscillate around this hypothetical atom with the betatron frequency. The amplitude of this motion is limited by the aperture of the hexapole. For higher velocities, the equilibrium orbit will move closer to the magnets, and the maximum amplitude of atoms oscillating around the equilibrium orbit is correspondingly decreased. The acceptance of the ring, the maximum area in phase space that the atoms may occupy in order to be stably confined, is thus given by

$$\mathrm{Acceptance} = \pi \omega_r (r_i - r_{\mathrm{equi}})^2. \tag{4.3}$$

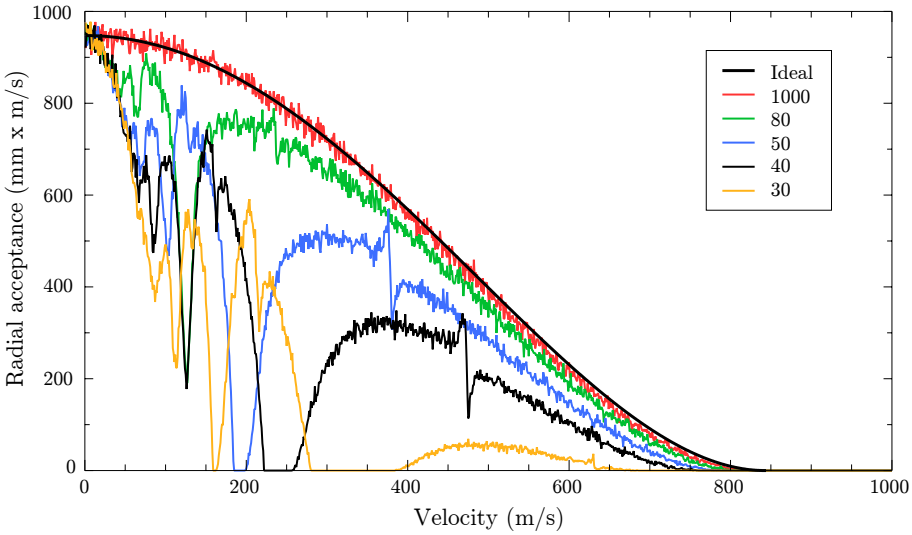

Figure 4.2 – The radial acceptance of a ring composed of 30, 40, 50, 80, and 1000 segments is plotted as a function of forward velocity. A ring consisting of 1000 straight hexapoles is essentially identical to the ideal case (bold black line). Reducing the number of segments reduces the acceptance of the ring and additionally introduces stop-bands.

In a ring made by bending the hexapole guide as discussed in Section 4.3, the betatron frequency is ∼3 kHz. This implies that a hydrogen atom with a longitudinal velocity of 600 m/s will have an equilibrium radius of 2 mm in a torus of 1 meter diameter. The radial acceptance at 600 m/s is an ellipse with (full) axes of $2r = 4$ mm and $2\omega_r r = 76$ m/s.

4.4.2 Transverse motion in a segmented ring

In order to keep the atoms in a tight bunch as they revolve around the ring, and to be able to inject multiple packets, it is necessary to break the symmetry of the ring, i.e., to make a ring composed out of many segments separated by short gaps. Rather than curved hexapoles, we consider the use of straight hexapoles as these are much simpler to construct. In this section, we will use Monte-Carlo simulations to determine how the acceptance of a ring depends on the number of segments. Similar calculations for an electric synchrotron were presented in [50, 68].

In our simulation, the magnetic force on the atoms in the hexapole is assumed to be perfectly linear with a force constant of $k_{\mathrm{hex}} = m\omega_r^2$, where m is the mass of the atom and $\omega_r/2\pi$ is the betatron frequency, taken to be 3 kHz. Using this force as an input, the trajectories of the atoms are calculated using a second-order Runge-Kutta method. At every time step, it is checked

whether or not the distance of the atom with respect to the centreline of the hexapole in which it is located (at that instant), exceeds the aperture r_i of the hexapole; $r_i = 4\,\text{mm}$ in our simulations. The two-dimensional acceptance for a given longitudinal velocity and number of ring-segments is found from the fraction of molecules that remains in the ring after 20 ms, multiplied by the initial phase-space area.

Figure 4.2 shows the resulting acceptance for a ring composed of 30, 40, 50, 80, and 1000 straight hexapoles, whose lengths are adjusted accordingly to accommodate the one-meter diameter of the ring. In the simulation the gaps are assumed to be small. For each data point, 4000 molecules are generated with an initial position, x, and initial velocity, v_x, randomly chosen within a certain range that is larger than the acceptance. The z position is initially set to zero, while v_z is set to a value between 0 and 1000 m/s. The bold black curve in Fig. 4.2 shows the acceptance expected for an ideal hexapole torus. Not surprisingly, the acceptance of a ring composed out of 1000 straight hexapoles is virtually the same as that of an ideal ring. Note that losses due to Majorana transitions near the centre of the hexapoles are neglected, leading to an overestimate of the acceptance at low velocities (at high velocities, the atoms never cross the geometrical centre of the hexapole).

When the number of segments is decreased, two effects are observed: (i) it is seen that at high velocities the acceptance decreases, and (ii) that at specific velocities the acceptance is seen to have sharp dips. The former effect can be understood from the fact that in a straight hexapole the molecule will, on average, be further away from the geometrical centre than in a curved ring. The dips at certain velocities are so-called stop-bands [101] resulting from the fact that the confinement force in a segmented ring is a periodic function. At stop-bands, the periodic force is resonant with the betatron oscillation, causing the atoms to be lost from the synchrotron as the amplitudes of their trajectories grow without bound. These resonances are absent if the length of a single hexapole is much smaller than the distance it takes for the atoms to make one transverse oscillation[2], i.e., if the phase-advance in a segment is $\ll 2\pi$. These stop bands were studied in a molecular synchrotron by Heiner *et al.* [55] and Zieger *et al.* [68]. For the remainder of this paper we will consider a ring that consists of 40 segments as a compromise between construction demands and the expected performance. For a 1-meter diameter ring, this implies that each segment has a length of 78.5 mm. From our simulations, the radial acceptance of such a ring for hydrogen atoms flying at 600 m/s is an ellipse with full axes of 2.5 mm and 40 m/s, i.e., a factor of 3 smaller than for an ideal hexapole ring with the same diameter. The vertical acceptance is $5.4\,\text{mm} \times 100\,\text{m/s}$; note however that the vertical extent of the stored beam is limited by the 1.8 mm gap used for injecting the beam.

[2]Motional resonances are inevitably introduced by small misalignments of the individual hexapoles that lead to a periodic kick every round-trip.

4.4.3 Longitudinal motion in a segmented ring

In the electric synchrotron demonstrated by Zieger *et al.* [56], bunching is achieved by temporarily ($\sim$20 μs) increasing the voltages by 25% as the molecules pass the gaps between successive segments. For a magnetic ring, this would require unacceptably large currents. Therefore, we consider a scheme whereby successive segments are connected to separate power supplies which generate sinusoidally varying currents with a relative phase of π. This bunching scheme is identical to that used in linear accelerators for charged particles [101]. A hypothetical atom – the so-called *synchronous* atom – flying with a velocity v_s will pass the gaps when the currents are zero and it will keep its original velocity. Atoms that are slightly behind the synchronous atom will pass the gap when the magnetic field in the segment in front of them is reduced with respect to its nominal value, while the magnetic field in the segment behind them is increased. As a consequence, these atoms will be accelerated. Vice versa, atoms that are slightly in front of the synchronous atom will pass the gap slightly earlier when the magnetic field in the segment in front of them is larger than the magnetic field in the segment behind them and they will therefore be decelerated. As a result, atoms with a position and velocity close to those of the synchronous atom will oscillate around the synchronous atom as it revolves the ring.

In order to calculate the longitudinal acceptance, we follow a procedure similar to the one used to describe phase stability in a Stark or Zeeman decelerator [8, 102]. When an atom moves from segment n to segment $(n+1)$, it gains or loses an amount of kinetic energy that depends on the phase of the oscillating dipole field at the time that the atom passes the gap and is given by:

$$\begin{aligned}\Delta K(\phi) &= \mu\left[(B_{\mathrm{hex,n+1}} + B_{\mathrm{dip},n+1}\sin\phi_{n+1}) - (B_{\mathrm{hex,n}} + B_{\mathrm{dip},n}\sin\phi_n)\right] \\ &= 2\mu_B B_{\mathrm{dip}}\sin\phi, \end{aligned} \tag{4.4}$$

where we have used the condition that the dipole fields in successive segments have a phase difference of π, i.e., $\phi_{n+1} = \phi_n + \pi$, and the magnetic dipole moment of hydrogen in large fields is equal to one Bohr magneton. In order to describe the motion of non-synchronous atoms relative to the motion of the synchronous atom, we introduce the relative velocity, $\Delta v = v - v_s$, and phase, $\Delta\phi = \phi - \phi_s = \Delta z \cdot \omega / v_s$, with ω the frequency of the oscillating dipole field. Furthermore, the step-wise change in kinetic energy is regarded to originate from a continuously acting average force $\bar{F}(\phi) = \Delta K(\phi)/L$, where L is the distance between successive bunching segments. The equation of motion is then given by

$$\frac{d^2\phi}{dt^2} - \frac{2\mu_B B_{\mathrm{dip}}}{mL}\frac{\omega}{v_s}(\sin\phi - \sin\phi_s) = 0. \tag{4.5}$$

This equation is the familiar expression for a pendulum driven by a constant torque. Atoms close to the synchronous atom will oscillate around the synchronous atom with a frequency of:

$$\omega_z = \sqrt{\frac{2\mu_B B_{\mathrm{dip}}}{mL}\frac{\omega}{v_s}\cos\phi_s}. \tag{4.6}$$

We will be interested only in the case of $\phi_s = 0$, i.e., when the synchronous molecule remains at a constant speed as it revolves around the ring.

From Equation 4.6, we see that the synchrotron frequency is largest when L is small, i.e., if many bunching segments are used, and if the frequency of the applied magnetic field is large. As will be discussed in Section 4.4.4, we will need to switch off at least three segments in order to load packets into the ring. Since switching between the bunching configuration shown in Fig. 4.1(d) and the loading configuration shown in Figure 4.1(e) would require very sophisticated electronics, we consider the situation where every fourth segment in the ring is used for bunching, thus $L = 4L_{\mathrm{hex}}$. The oscillation frequency ω determines the capture range of the longitudinal well. By choosing $\omega/2\pi = 5{\cdot}v_s/L_{hex} = 38\,\mathrm{kHz}$ the buckets will have a length of ∼16 mm. Assuming an oscillating field of 5 mT, we find a synchrotron frequency of $\omega_z/2\pi = 42\,\mathrm{Hz}$ for hydrogen atoms with a velocity of around 600 m/s. The longitudinal acceptance becomes a diamond with diagonals of 16 mm and 3.0 m/s.

4.4.4 Loading atoms in a segmented ring

The use of permanent magnets makes it possible to generate strong confinement forces without the need for large currents. However, it introduces the problem of how to load the ring. The magnetic field of the hybrid hexapole lens presented in Section 4.3 can be turned off by running a current of 380 A through the wires. From experiments with the electric synchrotron consisting of 40 hexapoles, we know that switching off three segments is sufficient to allow beams to enter the synchrotron, which implies that we need a current pulse with a duration of ∼400 μs.

Alternatively, it may also be possible to let hydrogen atoms enter the ring in a high-field-seeking state, and to use an optical transition to transfer the atoms to a low-field seeking state. For instance, a transition could be driven from the $1S_{1/2}m_J = -1/2$ to the $2P_{3/2}m_J = 1/2$ state. In high field, this state decays primarily to the $1S_{1/2}m_J = +1/2$ state [103]. Because it is not necessary to switch off the confinement fields in this scheme, it would allow loading the ring without influencing the atoms that are already stored. In this way it may be possible to reach high densities of stored hydrogen atoms.

Type of motion	Frequency/2π	Acceptance	Trap depth
Cyclotron (Ω_{cycl})	190 Hz		
Synchrotron (ω_{z})	42 Hz	16 mm × 3.0 m/s	0.14 mK
Horiz. betatron (ω_{r})	2950 Hz	2.5 mm × 40 m/s	24 mK
Vertical betatron (ω_{y})	2950 Hz	5.4 mm × 100 m/s	150 mK

Table 4.1 – Typical frequencies and acceptances for hydrogen atoms in the $m_J = +1/2$ ground state with a forward velocity of $v_s = 600$ m/s stored in a 1-meter diameter magnetic synchrotron consisting of 40 hybrid lenses as shown in Fig. 4.1. Bunching is performed by running a 5 A AC current with $\omega/2\pi = 38$ kHz through the electromagnets of every fourth hexapole lens. The transverse acceptances are elliptical in phase-space, the numbers given here thus correspond to their (full) axes. The longitudinal acceptance is shaped like a diamond and described by its diagonals.

4.5 Studying cold collisions in a magnetic synchrotron

Our main interest for developing a magnetic synchrotron lies in its use for studying cold collisions between hydrogen atoms and various atoms and molecules, as discussed at length in Chapters 2 and 3. In the envisioned experiment, schematically depicted in Fig. 4.3(a), 10 packets of hydrogen atoms are made to revolve for a few seconds in the ring while colliding with pulses of atoms and molecules that are released from a high-repetition-rate pulsed valve. The hydrogen atoms are stored at a velocity of 600 m/s, while the velocity of the collision partner will be tuned to around 600 m/s by choosing the appropriate buffer gas and controlling the temperature of the pulsed valve. In this way, the collision energy can be tuned down to 0 K, with a resolution determined by the properties of the pulsed beam (note that, in a merged beam experiment, the energy resolution can be smaller than the energy spread of the colliding beams [24]). The packets of atomic hydrogen are injected and detected at a rate of 10 Hz or slower, depending on the storage time. The high-repetition-rate pulsed valve running at five times the cyclotron frequency, is synchronized with the trapped packets in such a way that half of the stored packets (the probe beam) will meet with a packet from the pulsed valve during every round-trip, while the other half of the stored packets is used as a reference (the reference beam). Figure 4.3(b) shows a simulation of the expected signal in such an experiment. The blue and red curves show the number of hydrogen atoms in the reference and probe beam, respectively, as a function of the number of round-trips. Due to collisions with particles from the pulsed valve, the number of atoms in the probe beam will decay faster than that in the reference beam. From the difference in lifetime, the relative collision cross-section can be determined. In the simulation it is assumed that every (inelastic or elastic) collision leads to a loss. This is not necessarily the case at very low temperatures, when the trap depth becomes comparable to the collision energy. In order to convert the measured loss rates into a cross-section, the trap depth should be accurately measured.

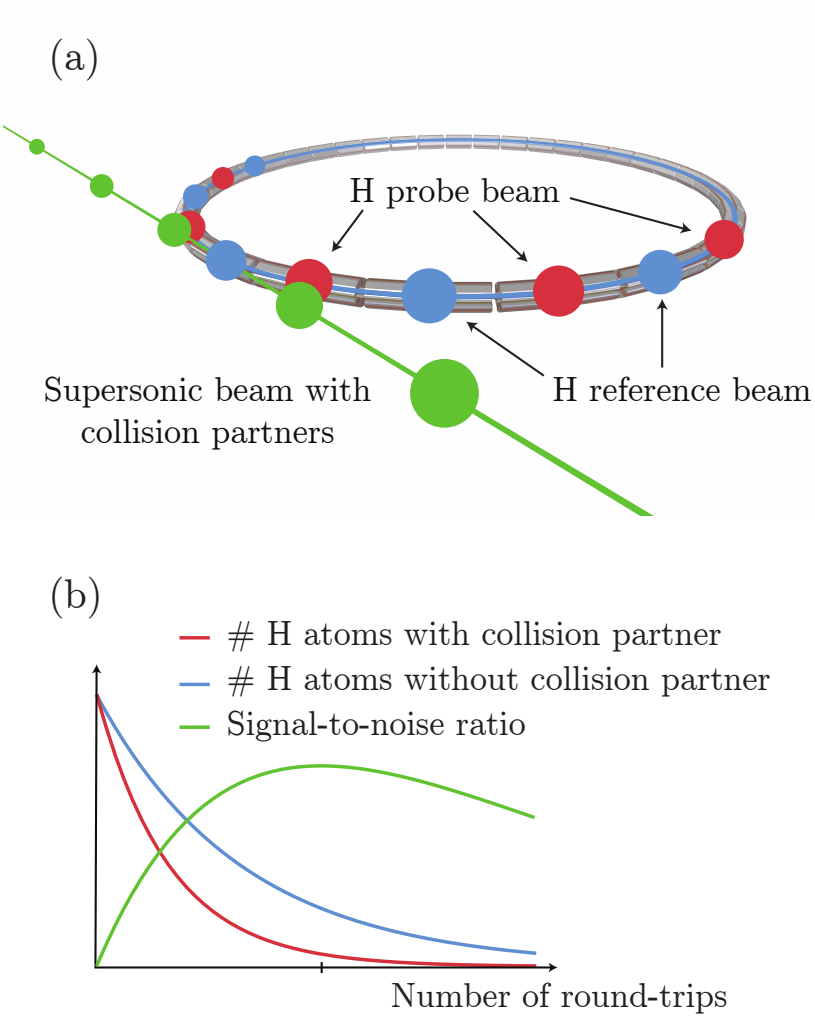

Figure 4.3 – (a) Schematic of the setup used for studying collisions in the synchrotron. (b) Schematic graphs of the hydrogen signal as function of the number of round-trips with (red) and without (blue) collisions, and (green) the S/N of the total (elastic + inelastic) collision cross-section that is determined from it. Here we have assumed the loss rate due to collisions k_{col} to be a third of the background loss rate k_{bg}.

The number of collisions taking place for the atoms in the synchrotron scales with the number of round-trips, hence there will be an increase in the ratio of the number of atoms in the reference beam with respect to the number of atoms in the probe beam. At the same time, however, the number of atoms in both beams decreases, increasing the error in determining these numbers.

The green line in Fig. 4.3(b) shows the collision rate (determined by measuring the number of atoms in the probe and reference beams after a certain time) divided by its error, i.e., the resulting signal-to-noise ratio (S/N). Initially, the S/N increases linearly with the number of round-trips until it flattens off and reaches a maximum at the number of round-trips corresponding to $\sim$2 times the lifetime τ_{probe} of the probe beam. For typical values of the densities and cross-sections, the lifetime of the hydrogen beams is much longer than a second, i.e., the maximum storage time for an experiment with a repetition rate of 10 Hz where ten packets are simultaneously stored in the ring. The repetition rate therefore needs to be reduced, lowering the number of detected atoms per second. However, the increased storage time compensates for this effectively, since the error in the measured decay rate goes as $1/\sqrt{n} \cdot 1/\tau$ for $\tau \ll 2\tau_{\mathrm{probe}}$, with n the number of detected atoms and τ the time the atoms spend in the synchrotron. We find that, for typical densities and cross-sections, a synchrotron offers a 100–1000 times enhanced S/N compared to a merged-beam experiment at a 10 Hz repetition rate.

4.6 Conclusions

In this Chapter, we have presented a design of a compact synchrotron based on 40 straight hybrid magnetic hexapole lenses that is able to store hydrogen atoms at velocities up to 600 m/s. Permanent magnets are used to create strong transverse-confinement forces, while electromagnets are used for bunching and for temporarily lowering the magnetic fields to allow hydrogen atoms to enter the ring. The hexapole lenses can be mounted in a similar way as in the electric synchrotron that was demonstrated by Zieger *et al.* [56]. The high degree of symmetry of the design ensures that the ring will be robust against misalignments and field imperfections. The electronics required to generate the necessary current pulses are routinely used in experiments with Zeeman decelerators [104–107]. The oscillating currents necessary to create the longitudinal trapping potential can be generated by using a resonant circuit. The modest heat load due to Ohmic losses in the coils can easily be taken care of by cooling the base plate that is thermally connected to the aluminum housing and magnet assemblies. With analytical models that were previously used to characterize an electric synchrotron, we have calculated the oscillation frequencies and acceptance for hydrogen atoms. The results are summarised in table 4.1 along with the parameters used in the simulation. The ring should be able to store a reasonable fraction of a supersonic beam at 600 m/s; the transverse acceptance is comparable to, while the longitudinal acceptance is about 20 times smaller than, the phase space occupied by atoms in a typical supersonic beam. Assuming a beam density of 10^{10} /cm^3, this corresponds to 5×10^7 atoms per bucket.

While we have performed our analysis for hydrogen atoms, the synchrotron will in principle also store other paramagnetic atoms or molecules. The max-

imum velocity that can be stored scales with the square root of the magnetic moment over the mass of the particle. This ratio is listed for various atoms and molecules in van de Meerakker *et al.* [11]. Although it does not seem feasible to store other atoms or molecules directly from a supersonic source (i.e., with a velocity above 300m/s), various atoms and molecules could be stored if injected from a cryogenic buffer gas source [72].

A magnetic synchrotron can be used to study collisions between hydrogen (the most abundant atom in the universe) and virtually any atom or molecule, including hydrogen molecules (the most abundant molecule in the universe), He, CO and ammonia at energies below 100 K. This will be highly relevant for astrophysical models. As a result of the low mass of atomic hydrogen, it is expected that the (total) cross-section for collisions between hydrogen and any molecule will exhibit many resonances in this energy range, which make them exciting systems to study and will contribute to a better understanding of the processes governing collision processes at low energies.

Bibliography

[1] R. D. Levine and R. B. Bernstein, *Molecular Reaction Dynamics and Chemical Reactivity* (Oxford University Press, 1987).

[2] J. N. Murrell and S. D. Bosanac, *Introduction to the Theory of Atomic and Molecular Collisions* (John Wiley & Sons, 1989).

[3] J. Toennies, W. Welz, and G. Wolf, *Molecular beam scattering studies of orbiting resonances and the determination of van der Waals potentials for H-Ne, Ar, Kr, and Xe and for H_2–Ar, Kr, and Xe*, The Journal of Chemical Physics **71**, 614 (1979).

[4] L. D. Carr, D. DeMille, R. V. Krems, and J. Ye, *Cold and ultracold molecules: Science, technology and applications*, New Journal of Physics **11** (2009).

[5] N. F. Ramsey, *Molecular Beams* (Oxford University Press, 1956).

[6] G. Scoles, *Atomic and Molecular Beam Methods* (Oxford University Press, 1988).

[7] Š. Urban, R. D'cunha, K. N. Rao, and D. Papoušek, *The $\Delta k = \pm 2$ "forbidden band" and inversion-rotation energy levels of ammonia*, Canadian Journal of Physics **62**, 1775 (1984).

[8] H. L. Bethlem, F. M. H. Crompvoets, R. T. Jongma, S. Y. T. van de Meerakker, and G. Meijer, *Deceleration and trapping of ammonia using time-varying electric fields*, Physical Review A **65**, 053416 (2002).

[9] H. L. Bethlem, G. Berden, and G. Meijer, *Decelerating Neutral Dipolar Molecules*, Physical Review Lett **83**, 1558 (1999).

[10] S. Y. T. van de Meerakker, H. L. Bethlem, and G. Meijer, *Taming molecular beams*, Nature Physics **4**, 595 (2008).

[11] S. Y. T. van de Meerakker, H. L. Bethlem, N. Vanhaecke, and G. Meijer, *Manipulation and control of molecular beams*, Chemical Reviews **112**, 4828 (2012).

[12] C. Cheng, A. P. P. van der Poel, P. Jansen, M. Quintero-Pérez, T. E. Wall, W. Ubachs, and H. L. Bethlem, *Molecular Fountain*, Physical Review Letters **117**, 253201 (2016).

[13] M. T. Bell and T. P. Softley, *Ultracold molecules and ultracold chemistry*, Molecular Physics **107**, 99 (2009).

[14] E. Narevicius and M. G. Raizen, *Toward cold chemistry with magnetically decelerated supersonic beams*, Chemical reviews **112**, 4879 (2012).

[15] M. Brouard, D. H. Parker, and S. Y. T. van de Meerakker, *Taming molecular collisions using electric and magnetic fields*, Chemical Society reviews **43**, 7279 (2014).

[16] B. K. Stuhl, M. T. Hummon, and J. Ye, *Cold State-Selected Molecular Collisions and Reactions*, Annual Review of Physical Chemistry **65**, 501 (2014).

[17] N. Balakrishnan, *Ultracold molecules and the dawn of cold controlled chemistry*, Journal of Chemical Physics **145** (2016).

[18] O. Dulieu and A. Osterwalder (Eds.), *Cold Chemistry* (The Royal Society of Chemistry, 2018).

[19] A. Schutte, D. Bassi, F. Tommasini, and G. Scoles, *Orbiting resonances in the scattering of H atoms by mercury at thermal energies*, Physical Review Letters **29**, 979 (1972).

[20] S. Chefdeville, T. Stoecklin, A. Bergeat, K. M. Hickson, C. Naulin, and M. Costes, *Appearance of Low Energy Resonances in CO-Para-H_2 Inelastic Collisions*, Physical Review Letters **109**, 023201 (2012).

[21] S. Chefdeville, Y. Kalugina, S. Y. T. van de Meerakker, C. Naulin, F. Lique, and M. Costes, *Observation of Partial Wave Resonances in Low-Energy O_2-H_2 Inelastic Collisions*, Science **341**, 1094 (2013).

[22] A. B. Henson, S. Gersten, Y. Shagam, J. Narevicius, and E. Narevicius, *Observation of resonances in Penning ionization reactions at sub-kelvin temperatures in merged beams*, Science **338**, 234 (2012).

[23] E. Lavert-Ofir et al., *Observation of the isotope effect in sub-kelvin reactions*, Nature Chemistry **6**, 332 (2014).

[24] Y. Shagam and E. Narevicius, *Sub-Kelvin Collision Temperatures in Merged Neutral Beams by Correlation in Phase-Space*, The Journal of Physical Chemistry C **117**, 22454 (2013).

[25] A. Klein et al., *Directly probing anisotropy in atom–molecule collisions through quantum scattering resonances*, Nature Physics **13**, 35 (2017).

[26] J. Jankunas, B. Bertsche, and A. Osterwalder, *Study of the Ne ($^3P_2$) + CH_3F Electron Transfer Reaction Below 1 Kelvin*, The Journal of Physical Chemistry A **118**, 3875 (2014).

[27] J. Jankunas, B. Bertsche, K. Jachymski, M. Hapka, and A. Osterwalder, *Dynamics of gas phase Ne^*+NH_3 and Ne^*+ND_3 Penning ionisation at low temperatures*, The Journal of Chemical Physics **140**, 244302 (2014).

[28] A. Osterwalder, *Merged neutral beams*, EPJ Techniques and Instrumentation **2**, 10 (2015).

[29] J. Jankunas, K. Jachymski, M. Hapka, and A. Osterwalder, *Observation of orbiting resonances in He ($^3S_1$) + NH_3 Penning ionization*, Journal of Chemical Physics **142** (2015).

[30] J. Jankunas, K. Jachymski, M. Hapka, and A. Osterwalder, *Importance of rotationally inelastic processes in low-energy Penning ionization of CHF_3*, Journal of Chemical Physics **144**, 1 (2016).

[31] K. Jachymski, M. Hapka, J. Jankunas, and A. Osterwalder, *Experimental and Theoretical Studies of Low-Energy Penning Ionization of NH_3,*

CH_3F, and CHF_3, ChemPhysChem **17**, 3776 (2016).

[32] P. Allmendinger, J. Deiglmayr, O. Schullian, K. Höveler, J. A. Agner, H. Schmutz, and F. Merkt, *New Method to Study Ion–Molecule Reactions at Low Temperatures and Application to the $H_2^+ + H_2 \rightarrow H_3^+ + H$ Reaction*, ChemPhysChem **17**, 3596 (2016).

[33] G. Dupeyrat, J. B. Marquette, and B. R. Rowe, *Design and testing of axisymmetric nozzles for ion-molecule reaction studies between 20 K and 160 K*, Physics of Fluids **28**, 1273 (1985).

[34] B. R. Rowe, G. Dupeyrat, J. B. Marquette, and P. Gaucherel, *Study of the reactions $N_2^+ + 2\,N_2 \rightarrow N_4^+ + N_2$ and $O_2^+ + 2\,O_2 \rightarrow O_4^+ + O_2$ from 20 to 160 K by the CRESU technique*, The Journal of Chemical Physics **80**, 4915 (1984).

[35] I. R. Sims et al., *Ultralow temperature kinetics of neutral-neutral reactions. The technique and results for the reactions $CN + O_2$ down to 13 K and $CN + NH_3$ down to 25 K*, The Journal of Chemical Physics **100**, 4229 (1994).

[36] L. A. Mertens et al., *Rotational energy transfer in collisions between CO and Ar at temperatures from 293 to 30 K*, Chemical Physics Letters **683**, 521 (2017).

[37] J. J. Gilijamse, S. Hoekstra, S. Y. T. van de Meerakker, G. C. Groenenboom, and G. Meijer, *Near-threshold inelastic collisions using molecular beams with a tunable velocity*, Science **313**, 1617 (2006).

[38] M. Kirste et al., *Quantum-state resolved bimolecular collisions of velocity-controlled OH with NO radicals*, Science **338**, 1060 (2012).

[39] A. T. J. B. Eppink and D. H. Parker, *Velocity map imaging of ions and electrons using electrostatic lenses: Application in photoelectron and photofragment ion imaging of molecular oxygen*, Review of Scientific Instruments **68**, 3477 (1997).

[40] A. von Zastrow, J. Onvlee, D. H. Parker, and S. Y. T. van de Meerakker, *Analysis of velocity-mapped ion images from high-resolution crossed-beam scattering experiments: a tutorial review*, EPJ Techniques and Instrumentation **2**, 11 (2015).

[41] A. von Zastrow, J. Onvlee, S. N. Vogels, G. C. Groenenboom, A. van der Avoird, and S. Y. T. van de Meerakker, *State-resolved diffraction oscillations imaged for inelastic collisions of NO radicals with He, Ne and Ar*, Nature Chemistry **6**, 216 (2014).

[42] S. N. Vogels, J. Onvlee, S. Chefdeville, A. van der Avoird, G. C. Groenenboom, and S. Y. T. van de Meerakker, *Imaging resonances in low-energy NO-He inelastic collisions*, Science **350**, 787 (2015).

[43] J. Onvlee et al., *Imaging quantum stereodynamics through Fraunhofer scattering of NO radicals with rare-gas atoms*, Nature Chemistry **9**, 226 (2016).

[44] S. Willitsch, M. T. Bell, A. D. Gingell, and T. P. Softley, *Chemical applications of laser- and sympathetically-cooled ions in ion traps*, Physical Chemistry Chemical Physics **10**, 7200 (2008).

[45] S. Willitsch, M. Bell, A. Gingell, S. Procter, and T. Softley, *Cold Reactive Collisions between Laser-Cooled Ions and Velocity-Selected Neutral Molecules*, Physical Review Letters **100**, 043203 (2008).

[46] Y.-P. Chang, K. Długołęcki, J. Küpper, D. Rösch, D. Wild, and S. Willitsch, *Specific Chemical Reactivities of Spatially Separated 3-Aminophenol Conformers with Cold Ca^+ Ions*, Science **342**, 98 (2013).

[47] B. C. Sawyer et al., *Cold heteromolecular dipolar collisions*, Physical Chemistry Chemical Physics **13**, 19059 (2011).

[48] M. Strebel, T. O. Müller, B. Ruff, F. Stienkemeier, and M. Mudrich, *Quantum rainbow scattering at tunable velocities*, Physical Review A **86**, 062711 (2012).

[49] F. M. H. Crompvoets, *A Storage Ring for Neutral Molecules*, Ph.D. thesis, Radboud Universiteit Nijmegen (2004).

[50] C. E. Heiner, *A molecular synchrotron*, Ph.D. thesis, Radboud Universiteit Nijmegen (2009).

[51] P. C. Zieger, *A Synchrotron for Polar Molecules*, Ph.D. thesis, Radboud Universiteit Nijmegen (2012).

[52] D. P. Katz, *A storage ring for polar molecules*, The Journal of Chemical Physics **107**, 8491 (1997).

[53] F. M. Crompvoets, H. L. Bethlem, R. T. Jongma, and G. Meijer, *A prototype storage ring for neutral molecules*, Nature **411**, 174 (2001).

[54] C. E. Heiner, D. Carty, G. Meijer, and H. L. Bethlem, *A molecular synchrotron*, Nature Physics **3**, 115 (2007).

[55] C. E. Heiner, G. Meijer, and H. L. Bethlem, *Motional resonances in a molecular synchrotron*, Physical Review A **78**, 030702 (2008).

[56] P. C. Zieger, S. Y. T. van de Meerakker, C. E. Heiner, H. L. Bethlem, A. J. A. van Roij, and G. Meijer, *Multiple Packets of Neutral Molecules Revolving for over a Mile*, Physical Review Letters **105**, 173001 (2010).

[57] P. C. Zieger, C. J. Eyles, G. Meijer, and H. L. Bethlem, *Resonant excitation of trapped molecules in a molecular synchrotron*, Physical Review A **87**, 043425 (2013).

[58] J. Loreau and A. van der Avoird, *Scattering of NH_3 and ND_3 with rare gas atoms at low collision energy*, Journal of Chemical Physics **143**, 184303 (2015).

[59] Y. T. Lee, *Molecular-Beam Studies of Elementary Chemical Processes*, Science **236**, 793 (1987).

[60] D. R. Herschbach, *Molecular Dynamics of Elementary Chemical Reactions*, Angewandte Chemie - International Edition **26**, 1221 (1987).

[61] E. Roueff and F. Lique, *Molecular excitation in the interstellar medium:*

Recent advances in collisional, radiative, and chemical processes, Chemical Reviews **113**, 8906 (2013).

[62] D. W. Chandler, *Cold and ultracold molecules: Spotlight on orbiting resonances*, Journal of Chemical Physics **132** (2010).

[63] N. Balakrishnan, A. Dalgarno, and R. C. Forrey, *Vibrational relaxation of CO by collisions with ^{4}He at ultracold temperatures*, The Journal of Chemical Physics **113**, 621 (2000).

[64] C. Naulin and M. Costes, *Experimental search for scattering resonances in near cold molecular collisions*, International Reviews in Physical Chemistry **33**, 427 (2014).

[65] J. Onvlee, S. N. Vogels, and S. Y. T. van de Meerakker, *Unraveling Cold Molecular Collisions: Stark Decelerators in Crossed-Beam Experiments*, ChemPhysChem **17**, 3583 (2016).

[66] M. Costes and C. Naulin, *Observation of quantum dynamical resonances in near cold inelastic collisions of astrophysical molecules*, Chemical Science **7**, 2462 (2016).

[67] S. D. Gordon, J. Zou, S. Tanteri, J. Jankunas, and A. Osterwalder, *Energy Dependent Stereodynamics of the Ne($^3P_2$)+Ar Reaction*, Physical Review Letters **119**, 053001 (2017).

[68] P. C. Zieger, C. J. Eyles, S. Y. T. van de Meerakker, A. J. A. van Roij, H. L. Bethlem, and G. Meijer, *A Forty-Segment Molecular Synchrotron*, Zeitschrift für Physikalische Chemie **227**, 1605 (2013).

[69] U. Even, *The Even-Lavie valve as a source for high intensity supersonic beam*, EPJ Techniques and Instrumentation **2**, 17 (2015).

[70] L. Minnhagen, *Spectrum and the energy levels of neutral argon, Ar I*, Journal of the Optical Society of America **63**, 1185 (1973).

[71] C. Meng, A. P. P. van der Poel, C. Cheng, and H. L. Bethlem, *Femtosecond laser detection of Stark-decelerated and trapped methylfluoride molecules*, Physical Review A **92**, 90 (2015).

[72] N. R. Hutzler, H. I. Lu, and J. M. Doyle, *The buffer gas beam: An intense, cold, and slow source for atoms and molecules*, Chemical Reviews **112**, 4803 (2012).

[73] Q. Ma, A. van der Avoird, J. Loreau, M. H. Alexander, S. Y. T. van de Meerakker, and P. J. Dagdigian, *Resonances in rotationally inelastic scattering of NH_3 and ND_3 with H_2*, The Journal of Chemical Physics **143**, 044312 (2015).

[74] R. W. B. Jr, G. Duquette, C. J. N. van den Meijdenberg, A. M. Rulis, G. Scoles, and K. M. Smith, *Molecular beam scattering experiments with polar molecules: measurement of differential collision cross sections for H_2O+H_2, He, Ne, Ar, H_2O and NH_3+H_2, He, NH_3*, Journal of Physics B **8**, 3034 (1975).

[75] H. Meyer, U. Buck, R. Schinke, and G. H. F. Diercksen, *Rotationaly*

inelastic scattering and potential calculation for NH_3+He, The Journal of Chemical Physics **84**, 4976 (1986).

[76] B. Schramm, E. Elias, L. Kern, G. Natour, A. Schmitt, and C. Weber, *Precise Measurements of Second Virial Coefficients of Simple Gases and Gas Mixtures in the Temperature Range Below 300 K*, Berichte der Bunsengesellschaft für physikalische Chemie **95**, 615 (1991).

[77] J. Schleipen and J. ter Meulen, *State-to-state cross sections for rotational excitation of ortho- and para-NH_3 by He and H_2*, Chemical Physics **156**, 479 (1991).

[78] H. Meyer, *Counterpropagating pulsed molecular beam scattering of NH_3–Ar. I. State resolved integral cross sections*, The Journal of Chemical Physics **1011**, 6686 (1994).

[79] H. Meyer, *Counterpropagating pulsed molecular beam scattering of NH_3–Ar. II. State resolved differential cross sections*, The Journal of Chemical Physics **101**, 6697 (1994).

[80] G. C. M. van der Sanden, P. E. S. Wormer, A. van der Avoird, J. Schleipen, and J. J. ter Meulen, *On the propensity rules for inelastic NH_3–rare gas collisions*, The Journal of Chemical Physics **103**, 10001 (1995).

[81] J. J. Kay, S. Y. T. van de Meerakker, E. A. Wade, K. E. Strecker, and D. W. Chandler, *Differential Cross Sections for Rotational Excitation of ND_3 by Ne*, Journal of Physical Chemistry A **113**, 14800 (2009).

[82] F. Pirani, L. F. Roncaratti, L. Belpassi, F. Tarantelli, and D. Cappelletti, *Molecular-beam study of the ammonia-noble gas systems: Characterization of the isotropic interaction and insights into the nature of the intermolecular potential*, Journal of Chemical Physics **135**, 1 (2011).

[83] S. Pratt, P. Dehmer, and J. Dehmer, *Photoionization of excited molecular states. H_2 $C^1\Pi_u^*$*, Chemical Physics Letters **105**, 28 (1984).

[84] S. Hoekstra, J. J. Gilijamse, B. Sartakov, N. Vanhaecke, L. Scharfenberg, S. Y. T. van de Meerakker, and G. Meijer, *Optical pumping of trapped neutral molecules by blackbody radiation*, Physical Review Letters **98**, 133001 (2007).

[85] D. Dahl, *SIMION for the personal computer in reflection*, International Journal of Mass Spectrometry **200**, 3 (2000).

[86] R. N. Zare, *Resonances in reaction dynamics*, Science **311**, 1383 (2006).

[87] R. V. Krems, *Molecules near absolute zero and external field control of atomic and molecular dynamics*, International Reviews in Physical Chemistry **24**, 99 (2005).

[88] R. V. Krems, *Cold controlled chemistry*, Physical Chemistry Chemical Physics **10**, 4079 (2008).

[89] L. Scharfenberg, J. Kłos, P. J. Dagdigian, M. H. Alexander, G. Meijer, and S. Y. T. van de Meerakker, *State-to-state inelastic scattering of Stark-*

decelerated OH radicals with Ar atoms, Physical Chemistry Chemical Physics **12**, 10660 (2010).

[90] L. Scharfenberg, K. B. Gubbels, M. Kirste, G. C. Groenenboom, A. Avoird, G. Meijer, and S. Y. T. van de Meerakker, *Scattering of Stark-decelerated OH radicals with rare-gas atoms*, The European Physical Journal D **65**, 189 (2011).

[91] K. K.-J. Kügler, K. Moritz, W. Paul, and U. Trinks, *Nestor–A magnetic storage ring for slow neutrons*, Nuclear Instruments and Methods **228**, 240 (1985).

[92] D. Thompson, R. V. E. Lovelace, and D. M. Lee, *Storage rings for spin-polarized hydrogen*, Journal of the Optical Society of America B **6**, 2227 (1989).

[93] H. Nishimura, G. Lambertson, J. G. Kalnins, and H. Gould, *Feasibility of a synchrotron storage ring for neutral polar molecules*, Review of Scientific Instruments **74**, 3271 (2003).

[94] K. Halbach, *Design of permanent multipole magnets with oriented rare earth cobalt material*, Nuclear instruments and methods **3**, 1 (1980).

[95] B. Ghaffari, J. Gerton, W. McAlexander, K. Strecker, D. Homan, and R. Hulet, *Laser-free slow atom source*, Physical Review A **60**, 3878 (1999).

[96] A. Goepfert, F. Lison, R. Schütze, R. Wynands, D. Haubrich, and D. Meschede, *Efficient magnetic guiding and deflection of atomic beams with moderate velocities*, Applied Physics B **69**, 217 (1999).

[97] E. Nikitin et al., *Measurement and prediction of the speed-dependent throughput of a magnetic octupole velocity filter including nonadiabatic effects*, Physical Review A **68**, 023403 (2003).

[98] J. P. Beardmore, A. J. Palmer, K. C. Kuiper, and R. T. Sang, *A hexapole magnetic guide for neutral atomic beams*, Review of Scientific Instruments **80**, 073105 (2009).

[99] J. Chavanne, *Radia (version 4.29). Retrieved from: http://www.esrf.eu/Accelerators/Groups/InsertionDevices/Software/Radia [2014, Aug 2],* 2009.

[100] Arnold Magnetic Technologies*, Spec. sheet n42sh, rev. 140112.*

[101] S. J. Humphries, *Principles of Charged Particle Acceleration* (Wiley, New York, 1986).

[102] A. W. Wiederkehr, S. D. Hogan, and F. Merkt, *Phase stability in a multistage Zeeman decelerator*, Physical Review A **82**, 043428 (2010).

[103] O. J. Luiten, *Lyman-α Spectroscopy of Magnetically Trapped Atomic Hydrogen*, Ph.D. thesis, Universiteit van Amsterdam (1993).

[104] N. Vanhaecke, U. Meier, M. Andrist, B. H. Meier, and F. Merkt, *Multistage Zeeman deceleration of hydrogen atoms*, Physical Review A **75**, 031402 (2007).

[105] E. Narevicius, A. Libson, C. G. Parthey, I. Chavez, J. Narevicius, U. Even, and M. G. Raizen, *Stopping Supersonic Beams with a Series of Pulsed Electromagnetic Coils: An Atomic Coilgun*, Physical Review Letters **100**, 093003 (2008).

[106] T. Momose, Y. Liu, S. Zhou, P. Djuricanin, and D. Carty, *Manipulation of translational motion of methyl radicals by pulsed magnetic fields*, Physical Chemistry Chemical Physics **15**, 1772 (2013).

[107] K. Dulitz, M. Motsch, N. Vanhaecke, and T. P. Softley, *Getting a grip on the transverse motion in a Zeeman decelerator*, The Journal of Chemical Physics **140**, 104201 (2014).

Samenvatting

Koude Botsingen in een Synchrotron voor Moleculen

Dit proefschrift beschrijft hoe botsingen met een lage energie te meten zijn met behulp van een synchrotron: een opslagring, een halve meter groot in diameter, waarin met sterke elektrische velden gedeutereerde ammoniakmoleculen opgeslagen kunnen worden. Deze ammoniakmoleculen hebben dan wel geen netto elektrische lading, maar de ladingsverdeling is niet helemaal gelijkmatig: ze zijn aan de ene kant iets positief geladen en aan de andere kant iets negatief. Hierdoor kunnen we hun beweging toch manipuleren met elektrische velden, al zijn daar uitzonderlijk sterke voor nodig.

De pakketjes ammoniakmoleculen zijn zeer koud (slechts 0,01 K, oftewel een honderdste graad Celsius boven het absolute nulpunt), vliegen met ongeveer 100 m/s door de synchrotron, en kunnen honderden rondjes lang opgeslagen worden. Zoals onder beschreven zal worden maakt dit ze ideaal om botsingsmetingen mee uit te voeren.

Bij botsingsmetingen wordt de zogenaamde botsingsdoorsnede gemeten, die (min of meer) beschrijft hoe dicht de deeltjes elkaar moeten passeren om te botsen. Hoe groter deze doorsnede, hoe meer botsingen plaats zullen vinden. Vooral interessant zijn botsingen bij lage botsingsenergieën. Als deze in het laboratorium nauwkeurig gemeten zouden kunnen worden, zou dat helpen om de scheikundige processen die plaatsvinden in gaswolken in het heelal, waarin de temperatuur typisch tussen 10 en 100 K is, beter te begrijpen. Verder voorspelt de kwantummechanica, de theorie van de kleine deeltjes, dat er bij lage botsingsenergien resonanties voorkomen: bij hele specifieke botsingsenergieën blijven de deeltjes kort aan elkaar plakken voordat ze huns weegs gaan. Bij welke specifieke botsingsenergieën dat precies gebeurt leert ons veel over de interactie tussen de deeltjes. Specifiek is dus het doel om, bij lage botsingsenergie, te meten hoe de botsingsdoorsnede afhangt van de botsingsenergie.

Om botsingen te kunnen meten met de synchrotron is een tweede bundellijn nodig met botsingspartners. Als botsingspartners nemen we atomen of moleculen zonder elektrisch dipoolmoment, die dus niets voelen van de elektrische velden in de synchrotron. Ze vliegen rechtdoor, en doorkruisen het pad van de ammoniakmoleculen in de zogenaamde botsingszone.

Elke keer dat de ammoniakmoleculen de botsingszone passeren, worden ze beschoten met botsingspartners. Bij een botsing zal (in bijna alle gevallen) het ammoniakmolecuul uit de ring geknikkerd worden. Door na een bepaalde tijd te meten hoeveel ammoniakmoleculen er nog in het pakketje zitten kunnen we meten hoeveel botsingen hebben plaatsgevonden, en daaruit kan de botsingsdoorsnede bepaald worden. Omdat de pakketjes ammoniakmoleculen in de synchrotron wel 100 rondjes lang opgeslagen kunnen worden, kan het botsings-

signaal 100 rondjes lang worden opgebouwd waardoor het veel makkelijker te meten is. Slechts door deze gevoeligheid is het mogelijk om deze botsingen, die een zeer lage botsingsdoorsnede hebben, te meten.

Het is echter nog niet zo gemakkelijk om deze lage botsingsenergieën in het laboratorium te bereiken. Daarom is een tweede voordeel van het gebruiken van een synchrotron voor botsingsmetingen, dat de bundellijn met botsingspartners zodanig geplaatst kan worden dat de botsingspartners in dezelfde richting vliegen als de ammoniakmoleculen. Hierdoor zullen de relatieve snelheid en dus de botsingsenergie veel lager zijn. De botsingsenergie kan gevarieerd worden door de snelheid van de ammoniakmoleculen te variëren, door de snelheid van de bundel met botsingspartners te variren, en door de ammoniakmoleculen selectief te laten botsen met de snellere botsingspartners vóór of de langzamere botsingspartners achter in de puls.

Deze ideeën hebben we in het laboratorium getest. Hoofdstuk 2 beschrijft in het kort de basisprincipes en experimenten alvorens de resultaten voor botsingen met argon te presenteren, en deze te vergelijken met theoretische, *ab initio* berekeningen uitgevoerd door bevriende theoreten. Het belangrijkste resultaat is dat de botsingsmetingen met ammoniak en argon bewijzen dat deze methode, namelijk het meten van botsingen met een synchrotron, inderdaad werkt zoals verwacht. De gevonden structuur in de botsingsdoorsnede zelf is in grote lijnen in overeenstemming met theorie, hoewel de botsingsenergieresolutie van de metingen te ruw is om de fijnere, door theorie voorspelde structuur te kunnen meten. Een aantal verbeteringen wordt voorgesteld, waarmee bijvoorbeeld de botsingsenergieresolutie verbeterd kan worden zodat dit soort fijne structuur wél gemeten zou kunnen worden, of waarmee bijvoorbeeld botsingsenergie verder verlaagd kan worden naar een regime waar meer uitgesproken structuren zijn om te meten.

In het verkrijgen van de resultaten is verreweg de meeste tijd echter gaan zitten in het uitgebreid karakteriseren van de experimentele opstelling en het nauwkeurig interpreteren van de gemeten data met behulp van simulaties. Deze meer praktische zaken worden in Hoofdstuk 3 uitgebreid beschreven. Samen geven Hoofdstukken 2 en 3 een compleet beeld van de experimenten die tijdens dit onderzoek zijn uitgevoerd.

In plaats van botsingsmetingen met ammoniakmoleculen opgeslagen in een synchrotron met elektrische velden, zou het interessant kunnen zijn om metingen te doen met waterstofatomen opgeslagen in een synchrotron met magnetische velden. In Hoofdstuk 4 wordt beschreven hoe zo een synchrotron eruit zou kunnen zien. Dit zou interessant zijn omdat waterstof het meestvoorkomende atoom is in het heelal. Verder voorspelt de theorie veel botsingsresonanties door de lage massa van het waterstofatoom in de lage botsingsenergieën die met deze magnetische synchrotron mogelijk zouden zijn. Het belangrijkste ingrediënt van de magnetische synchrotron is een hybride magneet die bestaat uit permanente magneten, die sterke velden kunnen maken zonder dat langdurige hoge stromen nodig zijn, en uit elektromagneten, die geschakeld kunnen worden om de waterstofatomen de ring binnen te laten en om de waterstofatomen in

de voorwaartse richting bijeen te houden. Onze berekeningen laten zien dat zo een synchrotron mogelijk zou moeten zijn.

Dankwoord

After more than 5 years and 4 months, it seems that my PhD research is finally drawing to a close. It has been quite a ride, to which many have contributed. Here I would like express my gratitude to those people.

Rick, de afgelopen jaren heb ik veel van je geleerd. Zowel vakinhoudelijk, van jouw intuïtieve begrip van de natuurkunde, als over mezelf. De laatste loodjes kwamen me niet van harte; toch ben je al die tijd je best blijven doen om mij te motiveren en ondersteunen. Ontzettend bedankt.

Wim, bedankt dat ik in jouw groep mocht promoveren. Ik heb me welkom gevoeld, niet het minst door de gezellige kerstborrels met knakworst en zuurkool.

My thanks to all of my colleagues from the Atoms, Molecules & Lasers group. The open atmosphere, interest in each other's research, and helpful attitudes make it a great place to learn and develop oneself. Of course, the social aspect is just as important, and I have many fond memories of borrels, Melon Jennifer, game nights, win-win situations on the roof of the Basket, or simply drinking a beer on a comfortable, concrete picnic bench. Rob, bedankt voor je aanmoedigende manier van meedenken en je technische ondersteuning.

I am indebted to all of my collaborators. I would like to thank Peter Zieger for spending several months in Amsterdam to teach me how to operate the synchrotron, and for remaining available for questions during all these years. Also, I would like to thank Ad van der Avoird and Jérôme Loreau for their theoretical work and their prompt answers to my many questions, and Bas van de Meerakker for helpful discussions. I would like to thank Gerard Meijer for his continued involvement and for providing the synchrotron with its new, old home.

I would like to thank the reviewing committee for their time and effort in reviewing my thesis.

I would like to thank Stichting FOM for funding my research and providing many courses, and my fellow FOM PhD students for making these courses an absolute joy to attend.

Also many thanks to my flat mates at Kanteel. For all the good times we had, dinners and barbecues, for our many discussions, both professional and personal, and simply for being there, making me feel at home. René, jij was er van begin tot eind; dank voor je gezelschap.

The last few months of analysis and writing took place in Groningen, where Steven Hoekstra was kind enough to provide me with a desk within the Fundamental Interactions and Symmetries group. Having a dedicated place to work, filled with welcoming colleagues to have lunch and drink coffee with,

played a crucial role in these months. For this I am very grateful to Steven and everyone else at the FIS group.

Christian and Stefan, our time working together was short but very enjoyable. We had great times in the lab, exploring de Pijp from our cosy apartment, going to the football, and doing many other things.

Ook wil ik mijn ouders, familie en vrienden bedanken voor hun steun. Niels, ik ben blij dat we van de gelegenheid gebruik hebben gemaakt om extra vaak af te spreken voor een film of spelletje. Hylke en Albert, bedankt voor jullie onverminderde vriendschap gedurende mijn jaren in Amsterdam. Ik kan altijd op jullie rekenen.

Lieve Esther, zonder jou was dit proefschrift er niet gekomen. Bedankt voor alles.

Groningen, 5 februari 2018

Aernout van der Poel

Publications

- *A detailed account on the measurement of cold collisions in a molecular synchrotron.*
  Aernout P. P. van der Poel, and Hendrick L. Bethlem.
  To be submitted.

- *Cold collisions in a molecular synchrotron.*
  Aernout P. P. van der Poel, Peter C. Zieger, Sebastiaan Y. T. van de Meerakker, Jérôme Loreau, Ad van der Avoird, and Hendrick L. Bethlem.
  Physical Review Letters **120**, 033402 (2018).

- *Molecular fountain.*
  Cunfeng Cheng, Aernout P. P. van der Poel, Paul Jansen, Marina Quintero-Pérez, Thomas E. Wall, Wim Ubachs, and Hendrick L. Bethlem.
  Physical Review Letters **117**, 253201 (2016).

- *A compact design for a magnetic synchrotron to store beams of hydrogen atoms.*
  Aernout P. P. van der Poel, Katrin Dulitz, Timothy P. Softley, and Hendrick L. Bethlem.
  New Journal of Physics **17**, 055012 (2015).

- *Femtosecond laser detection of Stark-decelerated and trapped methylfluoride molecules.*
  Congsen Meng, Aernout P. P. van der Poel, and Hendrick L. Bethlem.
  Physical Review A **92**, 023404 (2015).

- *First test of Lorentz invariance in the weak decay of polarized nuclei.*
  S. E. Müller, E. A. Dijck, H. Bekker, J. E. van den Berg, O. Böll, S. Hoekstra, K. Jungmann, C. Meinema, J.P. Noordmans, M. N. Portela, C. J. G. Onderwater, C. Pijpker, A. P. P. van der Poel, B. Santra, A. Sytema, R. G. E. Timmermans, O. O. Versolato, L. Willmann, H. W. Wilschut, K. Yai.
  Physical Review D **88**, 071901 (2013).